Politecnico di Milano
Dipartimento di Elettronica e Informazione
Doctoral Programme In Information Technology

SAR Polarimetric Monitoring by Natural Calibrators

Doctoral Dissertation of:
Lorenzo Iannini

Supervisor:
Prof. Andrea Monti Guarnieri

Tutor:
Prof. Michele D’Amico

The Chair of the Doctoral Program:
Prof. Carlo Fiorini

2009 – XXIV cycle

Abstract

THE thesis debates the problem of the external polarimetric calibration and system monitoring of Synthetic Aperture Radar (SAR) devices. More specifically, the efforts has been aimed at assessing the capabilities of natural in-scene scatterers and at proposing novel methodologies for the exploitation of such potential.

The first part surveys the calibration feasibility and the distortion estimation performance of the approaches based on distributed targets (DTs). It will be shown that, by introducing convenient assumptions on the distortion model and on the target properties, effective information on the system cross-talks and on the channel imbalance ratio can be extracted from the scene. However, clear evidence that a point calibrator is needed to accomplish a full polarimetric monitoring is also provided. The partial polarimetric calibration achieved by DTs is then investigated with concern to the achievable performance on the well-determinable parameters. A numerical optimization algorithm is proposed to improve the accuracy in case of low channel isolation.

The second part is dedicated to an innovative calibration approach based on the stable point targets, namely Permanent Scatterers (PS). The method, hereby called PolPSCal, allows for relative calibration of the full polarimetric distortion matrices (PDMs) affecting the stack images. The algorithm is neither constrained to a particular PDM model nor to any external information, though this latter is needed afterwards to normalize the calculated PDMs. The exploitation of the DT information for the relative calibration of the PolPSCal information is then investigated. The mathematical framework of such overarching natural target-based approach is reported, and a performance analysis is carried out on a 26 images RADARSAT-2 dataset registering promising results.

Summary

SAR polarimetry offers significant benefits in target characterization and contrast enhancement over traditional single-polarization acquisitions. Polarimetric applications obviously demand the preservation of amplitude and phase relationships between the different polarization channels. The accuracy requirements depend on the specific application and can be honoured through proper monitoring procedures aimed to remove distortion introduced by the system Transmit/Receive modules (TRMs) and/or by the propagation medium. This process is referred to as external calibration, and can be performed on the natural scene features, on deployed calibrators or on the combination of both. The main research question addressed in this thesis is how the scene information must be collected and processed in order to produce an effective contribution to the polarimetric system monitoring and data calibration activities.

In first part of the work an overview on the traditional POLSAR approaches based on the distributed targets (DTs) is introduced. The feasibility related to the estimation of the most acknowledged distortion model, comprising channel imbalances, cross-talks and Faraday rotations in the L/P-Band frequencies, is explored. The choice of a convenient set of case studies allowed to provide indication on the effectivness of DT-alone approaches and on the necessity of a calibrated point target (PT). Though it is demonstrated that a full polarimetric calibraton can be achieved only by using a PT, the analysis stresses the fact that significant information on the channel cross-talks and on the imbalance ratio can be nevertheless attained from DTs. The uncertainty on the parameter estimates due to data and model noise sources is assessed both at a theoretical level and on practical techniques. The reader is shown in the end that the poor performance attained by reference algorithms in case of high cross-talk levels or large Faraday rotations can be improved through numerical optimization.

An alternative calibration approach which exploits the temporal information provided by multi-image stacks rather than the traditional spatial statistics is then debated. It certainly represents the most innovative contribution of the thesis. The novel methodology is based on the stable natural targets, the so-called Permanent Scatterer (PS). When a sufficient density of PSs can be found within the selected image frame, the PS based technique, namely PolPSCal, offers a reliable relative calibration solution. More specifically, it returns the differential distortion information with respect to a master image of the stack. The work proceeds then by proposing an encompassing framework for polarimetric system monitoring based on both the spatial and the temporal exploitation of the natural targets. The solution relies exclusively on the in-scene information, and thus it is independent from calibrated reflectors and from other a-priori external information. A generic distortion model has been conceived, so that the approach can be readily tailored to different sensor scenarios, ranging from higher-frequency SARs to lower-frequency acquisitions affected by Faraday rotations. The DT estimates are indeed integrated with the PS differential distortion in order to achieve (up to an absolute radiometric scale factor) an unambiguous temporal monitoring of the system distortion, and therefore a consistent data calibration within the image stack. The performance has been in the assessed through synthetic simulations and validated on a Fine Quad-Pol Radarsat-2 dataset reporting promising stability results.

Contents

Nomenclature

Acronyms and Abbreviations

APN	Average Polarimetric Noise
CFAR	Constant False Alarm Rate
Cpol	Co-polarised channels (HH,VV if linear)
CT	Cross-Talk
DI	Dispersion Index
DT	Distributed Target
DWP	Distortion Work-Point
FRA	Faraday Rotation Angle
GLRT	Generalized Likelihood Ratio Test
HH	Horizontal polarisation on transmit / Horizontal polarisation on receive
HV	Horizontal polarisation on transmit / Vertical polarisation on receive
LR	Likelihood Ratio
LS	Least Squares
ML	Maximum Lakelihood
MNE	Maximum Normalized Error
MSE	Mean Squared Error
NESZ	Noise Equivalent σ_0
NL	Number of Looks
PDM	Polarimetric Distortion Matrix
POLSAR	Polarimetric SAR
PS	Permanent Scatterer
PT	Point Target

RF	Radio Frequency
RMSE	Root Mean Square Error
ROI	Region Of Interest
Rx	Reception
RS2	Radarsat-2
SAR	Synthetic Aperture Radar
SCR	Signal to Clutter Ratio
SLC	Single Look Complex
SNR	Signal to Noise Ratio
TMSE	Total Mean Squared Error
TRM	Transmit/Receive Module
Tx	Transmission
VH	Vertical polarisation on transmit / Horizontal polarisation on receive
VV	Vertical polarisation on transmit / Vertical polarisation on receive
Xpol	Cross-polarised channels (HV,VH if linear)

Symbol Notations

$\mathbf{X}^T$	Transpose of the matrix **X**
$\mathbf{X}^*$	Complex conjugate of the matrix **X**
$\mathbf{X}^H$	Hermitian conjugate (transpose conjugate) of the matrix **X**
$\mathbf{X}^{-1}$	Inverse of the matrix **X**
$\mathbf{X}^\dagger$	Moore-Penrose pseudoinverse of the matrix **X**
$\mathbf{I}_N$	$N \times N$ identity matrix
$\|\|\mathbf{x}\|\|$	L^2-norm of the vector **x**
$\|\|\mathbf{X}\|\|_F$	Frobenius norm of the matrix **X**
$\det(\mathbf{X})$	Determinant of the matrix **X**
$\mathrm{eig}(\mathbf{X})$	Eigenvalues of the matrix **X**
$\mathrm{Tr}(\mathbf{X})$	Trace of the matrix **X**
$\mathrm{vec}(\mathbf{X})$	The vector-version of the matrix **X**
$\|.\|$	Modulus of
$\angle(.)$	Phase of
$\mathcal{R}(.)$	Real part of
$\mathcal{I}(.)$	Imaginary part of
$\circ$	Hadamard, or entrywise, product
$\otimes$	Kronecker product

$\sim$	Distributed as
$\simeq$	Approximated by
$\propto$	Equal up to a scale factor
$\ll , \gg$	Much smaller,larger than
$\sum$	Sum
$\prod$	Product
$E[.]$	Expectation of
$\ln(.)$	Natural logarithm of
$\log_b(.)$	Base b logarithm of
$\mathcal{L}(\mathbf{Y}\|\Theta)$	Likelihood of the observation $\mathbf{Y}$ given the model parameter set Θ
$\langle x_i \rangle$	Sample average
$\langle x_{ij} \rangle_i$	Sample average along i
$\mathcal{N}(\mu, \sigma^2)$	Normal distribution with mean μ and variance σ^2
$\mathcal{CN}(\mu, \sigma^2)$	Complex normal distribution with mean μ and variance σ^2

CHAPTER 1

Introduction

1.1 Background and motivation

The interest in Synthetic Aperture Radar (SAR) data has considerably grown in the last decades due to their unveiled potential in land, ocean and also atmospheric feature observation and characterization. The interpretation of SAR backscatter with respect to the physical cell content is however far from straightforward, since its properties must always be related to the specific acquisition configuration in terms of resolution, frequency, time (with changing target and atmospheric conditions), look angle and polarization. The wave polarization plays in many cases [3, 47, 55] an essential role in uncovering the geophysical information of targets from their digitalized backscattering values. With fixed single-polarized antennas for transmission as well as for reception, however, some information of the backscattered field is lost, and the target features which can be provided by the measurement process are generally dependent on the target orientation angle around the line of sight [22]. A comprehensive definition of the backscattering phenomenon would be instead attained by retaining the complete set of polarized scattering combinations, represented by the scattering, or Sinclair, matrix [54]. This requires a radar equipment capable of decomposing the received wave into two orthogonally polarized components, which independently feed two identical and coherent reception channels. In a full-polarimetric system the reception polarization-diversity must then be accompanied by transmission polarization-diversity, which is generated by alternate radiation of orthogonally polarized pulse waves (horizontal and vertical are the ones far implemented in space-borne systems). The first successful experiments with SAR polarimetric systems date to 1985, when NASA/JPL efforts led to the sensor known as the CV-990 L-band radar. A few years later NASA/JPL was able to produce an operational, three-frequency polarimetric SAR (AIRSAR) flying on the DC-8 aircraft, which has taken part in many science data acquisition campaigns since 1988 [6]. In 1994 the SIR-C/X-Band SAR [24], the first polarimetric space-borne sensor, was lanched onboard a NASA shuttle, within a joint NASA/German Space Agency/Italian Space Agency mission. Such increased attention to the polarimetric context combined with a shifted interest towards the quantitative use of SAR data led consequently to a prolific debate on a wide gamma of polarimetric calibration/validation aspects.

Whereas absolute radiometric calibration refers to the process of estimation and removal from the data of the overall system gain, the polarimetric calibration aims to compensate polarimetric channel distortions. Both operations are needed in order to estabilish a correct relationships between radar backscatter and geophysical parameters. The object of this thesis is indeed the second calibration typology: the polarimetric calibration. As it is widely aknowledged, the distortions can be attributed to coupling and impurities in the TRMs (Transmit/Receive Modules) and in the radiating elements, to atmospheric perturbations and artifacts due to the software processing (e.g. quantization, focusing) [15, 19]. Internal in-flight calibration is the common approach to deal with the distortions introduced by the internal components and processing inaccuracies, whereas external calibration covers the whole distortion chain and thus represents an inescapable feedback throughout the mission life. With concern to this latter, techniques based solely on calibrated targets [21, 51], as well as techniques recommending the use of in-scene scattering information [38, 41, 49, 55] were proposed and verified on the DC-8 datasets and on the SIR-C acquisitions available a few years later [11, 17].

The scientific debate concerning the optimal distortion compensation strategies was then tailored throughout the years to the new polarimetric SAR missions, though progressing at a slower pace. The Japanese ALOS/PALSAR [43] sensor in particular raised most of the recent concerns due to the explicit necessity to account for both the system distortion and the Faraday rotations affecting its L-Band data-takes [42, 45]. On a general standpoint, the common trend that characterizes the SAR evolution over these last years is that of seeking an ever increasing system accuracy (meaning an higher calibration performance costraints) equipping at the same time the system with a higher range of beam modes. The following issues with respect to the calibration/validation routines must be therefore considered:

- An absolute polarimetric verification must be applied with a certain rivisit frequency to all the acquisition modes. When the sensor configurations is much larger then the number of sites qualified for the verification the scheduling of the system monitoring becomes challenging.

- The targets deployed in order to allow an absolute radiometric and polarimetric calibration must be maintained stable all along the mission operational life, i.e. their RCS should be constrained to a few fractions of dB accuracy. The more stringent is the accuracy requirement the more efforts/costs must be accounted in the project.
- Few natural calibration sites all over the globe are stable enough to provide the necessary accuracy without calibrated point targets (maybe only the rain forests at high frequencies can get close to the specifics [28, 43]).

Such forthcoming scenario would certainly benefit from additional unexpensive calibration sites. The belief supporting this work is that the natural scattering diversity, offered by the data available inside the SAR frame, still has to be fully exploited. So far, the reference techniques in literature [16, 38, 49] have made use of distributed target areas. The distortion is extracted from the pixel-wise second order moments of the target, which apparently make their use convenient. However, all these approaches rely on major assumptions either on the target statistics or on the number of the distortion parameters in order to keep the estimation problem well-posed. This necessarily leads to only partial distortion assessments or alternatively impairs significantly the calibration accuracy. Differently, the system monitoring problem can be tackled from a temporal monitoring perspective when a selected group of stable features can be used to create a coherent polarimetric connection between two images in the same dataset. In this case, the polarimetric and even the radiometric changes along the acquisition timeline can be detected, at the expense obviously of additional memory and computational resource allocation. This approach wuold be similar to the one proposed by D'Aria et al. in [9] for single-polarization systems, though applied to the polarimetric context and thus requiring a novel mathematical framework.

1.2 Research objectives and thesis outline

On a more encompassing perspective, the aim of this thesis is to provide practical and theoretical insights into the limits and the capabilities of traditional and novel multi-temporal methods for the calibration of polarimetric SAR imagery by means of in-scene natural targets. More specifically the work answers to the following research questions:

- Which is the theoretical capability of distributed target areas in assessing the image miscalibration in different distortion scenarios? Which are then the benefits in terms of assessment feasibility brought by the introduction of calibrated point targets?
- How do traditional algorithms based on distributed targets handle the estimation of the distortion at different frequency bands and how they can be possibly improved

without sacrificing the robustness that characterizes their analytic retrieval procedures?

- Is the intrinsic potential of in-scene natural mechanisms fully exploited yet? Can stable targets as opposed to the ramdomly distributed targets represent a valuable calibration alternative to the traditional techniques? What additional benefits and unavoidable limits should be then considered?
- Is the distortion information extracted from the stable scatterers a superset/subset of that returned by distributed target analysis, or the two sets of estimates bear complementary information? How can this information be integrated within an overarching natural target-based approach?

The first two questions are dealt in **chapter 2**, which is indeed devoted to the discussion of the non-linear inversion problem associated to the retrieval of the SAR distortion parameters (Channel imbalances, channel cross-talks and Faraday rotation) from the data measurements over the distributed target areas and from the observation of calibrated point targets. The structure of the chapter is two-fold: in the first part the problem equations delivered by the available calibrators are introduced and their effectiveness in terms of problem well-posedness and data sensitivity is assessed. A methodology based on local model linearization was used to provide a schematic overview of the distributed scatterers capabilities and to assess the estimation performance on two realistic distortion scenarios: 1. A symmetric system distortion model (cross-talks in Tx and Rx are reciprocal) with the presence of Faraday rotations handled by a distributed target alone; 2. a full distortion scenario (with all the cross-talks and imbalances to be estimated) where the aid of a corner reflector is employed. The second part of the chapter is then dedicated to practical estimation algorithms. The analysis focuses in particular on the assessment of the unambiguous parameter subset whose retrieval is advised, amongst many others, by the Quegan technique [38], still one of the most credited ones. A numeric optimization strategy is then proposed to overcome some of the accuracy limitations evidenced by analytic techniques.

An alternative calibration approach is then discussed in **chapter 3**. It basically answers to the research question n.3 and consists in taking advantage of multiple images collected over the same area. Whereas the DT-based approach made assumptions on the ensemble spatial statistics of the target (orientation symmetry), this latter makes explicit exploitation of the Permanent Scatterer (PS) temporal stability, in both its radiometric and polarimetric behavior. When a sufficient density of PSs can be found within the selected image frame (urban scenarios are in particular suited), the PS based technique, namely PolPSCal, offers a reliable relative calibration solution. More specifically it returns the differential distortion information with respect to a master image of the stack. The chapter presents the mathematical formalization (PS model and stable target characterization and identification), describes the steps of the algorithm implementation and provides the theoretical assessment of the approach performance on synthetic datasets.

Chapter 4 debates then an encompassing framework for polarimetric system monitoring based on both the spatial and the temporal exploitation of the natural targets, answering therefore to the last research question. The solution relies exclusively on the in-scene information, and thus it is independent from calibrated reflectors. A generic distortion model has been conceived, so that the approach can be readily tailored to different sensor scenarios, ranging from higher-frequency SARs to lower-frequency acquisitions affected by Faraday rotations. The DT estimates are indeed integrated with the PS differential distortion in order to achieve (up to an absolute radiometric scale factor) an unambiguous temporal monitoring of the system distortion, and therefore a consistent data calibration within the image stack. The performance has been assessed through synthetic simulations and validated on a Fine Quad-Pol Radarsat-2 dataset which comprises 26 images over the Barcelona area, returning an accuracy on the channel imbalance stability below 0.2 dB and on the cross-talk level <-35 dB.

Finally **chapter 5** summerizes the theoretical and concrete contribution to the SAR polarimetric calibration research field that the work so far conducted was able to achieve. The challenges ensuing from the techniques here proposed are remarked and some suggestion on future research work is offered.

CHAPTER 2

Assessment of the Polarimetric Distortion by Means of Distributed Targets: Theoretical Analysis and Estimation Strategies

In the last years, much effort has been spent by the SAR community investigating the benefits of SAR polarimetry (POLSAR) over traditional single-pol acquisitions. Much has been accomplished in a variety of applications ranging from classification, image correction, to biomass evaluation and other environmental studies. The understanding of the physical scattering phenomena is enhanced from the analysis of more polarization channels representing different antennas-target field interaction modes. The preservation of amplitude and phase relationships between the registered channels is fundamental, though it is hindered by the distortion introduced by the system TRMs and/or by the propagation medium. In the present chapter we will conduct an analysis on the model disturbances and on their compensation strategies by means of distributed targets (DTs) with reference to linearly polarized fully-polarimetric (FP) systems, actually the only operative mode for FP spaceborne SARs.

The accurate calibration of Polarimetric SAR data is not a trivial task, since it usually corresponds to an ill-posed problem. The large number of parameters which has to be estimated and the non-linearity of the solving equations makes the correct estimation of such unknowns difficult without the use of suitable assumptions. A number of approaches have been proposed in the last two decades in order to cope with a variety of POLSAR system acquisitions, based either on the use of DT alone and on the use of DT jointly with a target with known radar cross section, such as a trihedral corner reflector. A proper formalization of the intrinsic conditioning issues that affect the non-linear estimation problem is nonetheless still missing. To this end, the first part of the chapter has been spent in studying the theoretical feasibility of the distortion estimation problem by investigating a representative set of target/distortion model scenarios. The analysis was able to provide indicative information on the model uncertainty and to assess the impact of model disturbances on this latter. In the second part of the chapter the performance and the limitations associated to the most acknowledged calibration techniques are explored. A numeric optimization scheme which allows to exploit to a wider extent the available covariance information is in the end proposed.

2.1 The polarimetric distortion model

2.1.1 Sensor distortions

Full-polarization acquisitions in spaceborne systems are operationally attained by alternating in transmission (Tx) the horizontal (H) and vertical (V) polarizations and by recording them simultaneously at reception (Rx). The capability of steering the beam in order to fit a wide range of elevation and squint illumination angles, is accomplished in modern systems by using phased-array antennas composed of lots of radiating elements each with a phase shifter. The beam can then be modulated electronically by switching the elements or by changing the relative phases of the RF signals driving the elements. Each radiating element is controlled by the a Transmit/Receive Module (TRM) which includes Power and Low Noise amplification as well as phase and amplitude control and polarization switching. In such architecture, the signal can be affected by amplitude and phase perturbations and by channel cross-talks (CTs). The former lead to fluctuations in

- $\boldsymbol{A}$, the overall radiometric gain of the system, referred to the HH channel
- $\boldsymbol{f_1}$, the complex imbalance ratio between the vertical and the horizontal polarizations in the Rx phase(ideally 1)
- $\boldsymbol{f_2}$, the complex imbalance in the Tx phase (ideally 1)

whereas the latter contribute to

- $\boldsymbol{\delta_1}$, the fraction of H signal leaking into the V receiver
- $\boldsymbol{\delta_2}$, the fraction of V signal leaking into the H receiver
- $\boldsymbol{\delta_3}$, the fraction of H field transmitted alongside the V pulses

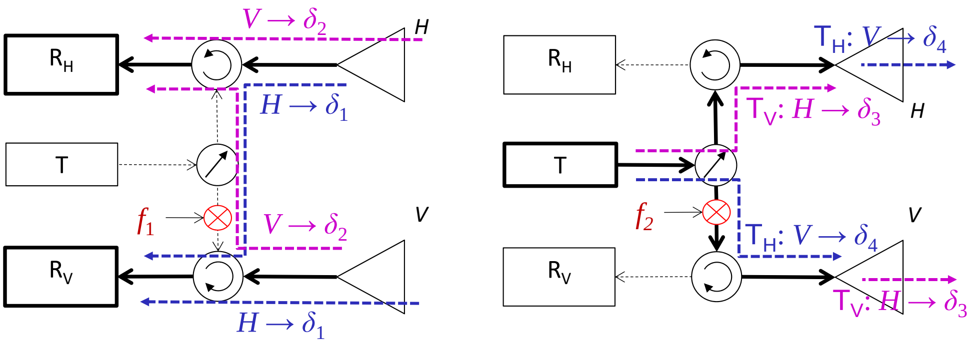

Figure 2.1: *Schematic representation of the cross-talk paths in the block comprising the TRM and the radiating elements (H and V polarizations) during the receive (**left**) and transmit (**right**) phases.*

- $\boldsymbol{\delta_4}$, the fraction of V field transmitted alongside the H pulses.

as schematically illustrated in Fig. 2.1. The overall system distortion is mathematically accounted into the observation $\mathbf{M}$ of the target backscatter matrix $\mathbf{S}$ through the model:

$$\begin{bmatrix} M_{HH} & M_{VH} \\ M_{HV} & M_{VV} \end{bmatrix} = A \cdot e^{j\phi} \begin{bmatrix} 1 & \delta_2 \\ \delta_1 & f_1 \end{bmatrix} \begin{bmatrix} S_{HH} & S_{VH} \\ S_{HV} & S_{VV} \end{bmatrix} \begin{bmatrix} 1 & \delta_3 \\ \delta_4 & f_2 \end{bmatrix} + \begin{bmatrix} N_{HH} & N_{VH} \\ N_{HV} & N_{VV} \end{bmatrix} \qquad (2.1)$$

or, with a compact nomenclature:

$$\mathbf{M} = A \cdot e^{j\phi} \cdot \mathbf{R}^T \cdot \mathbf{S} \cdot \mathbf{T} + \mathbf{N}. \qquad (2.2)$$

where the HH, HV, VH, VV subscripts refer to the 4 different polarization modes, ϕ is the overall target phase, $\mathbf{N}$ is the signal noise (both thermal noise and deviations from the linear distortion model).

The disturbances are either produced by the RF electronics (TRM) or by non-idealities in the radiating elements. When the CTs are mostly determined by the antenna, the reciprocity property of this latter should lead to the model simplification [19]:

$$\delta_1 = \delta_3, \qquad \delta_2 = \delta_4 \qquad (2.3)$$

that has been so far employed by a few well-acknowledged calibration approaches [45, 49]. Differently, when the CTs are dominated by the TRM leakages, the full CT model should be accounted. This is likely the case of modern polarimetric systems [42,46] which present a moltitude of TRMs (from 80 forming the PALSAR to 512 onboard the Radarsat-2) and very low antenna isolation. It was for instance assessed in [46] that the Radarsat-2 antenna cross-talk level is below -40 dB, much lower than that of the T/R modules that was estimated at -35 dB on average. Consider also that the behaviour of the TRM-driven distortion is uniform throughout the beams, and thus easier to handle than that induced by the antennas, which is usually range-dependent.

2.1.2 Faraday rotations

Several studies were able to shed light on the effects of the ionosphere on the SAR acquisitions [32,40]. The most significant disturbance on the polarimetric quality is represented by rotations of the wave polarization. The signal is degraded in its polarimetric purity since the channels are mixed according to the Faraday rotation model:

$$\begin{bmatrix} S'_{HH} & S'_{VH} \\ S'_{HV} & S'_{VV} \end{bmatrix} = \begin{bmatrix} \cos\Omega & \sin\Omega \\ -\sin\Omega & \cos\Omega \end{bmatrix} \begin{bmatrix} S_{HH} & S_{VH} \\ S_{HV} & S_{VV} \end{bmatrix} \begin{bmatrix} \cos\Omega & \sin\Omega \\ -\sin\Omega & \cos\Omega \end{bmatrix} \tag{2.4}$$

$$\mathbf{S}' = \mathbf{R_F}\mathbf{S}\mathbf{R_F}$$

with Ω being the rotation angle, or, identically, by expanding (2.4) in its vector representation:

$$\mathbf{s}' = \left(\mathbf{R}_\mathbf{F}^T \otimes \mathbf{R_F}\right) \cdot \mathbf{s} = \mathbf{H_F} \cdot \mathbf{s}, \tag{2.5}$$

$$\mathbf{s}' = \begin{bmatrix} S'_{HH} \\ S'_{HV} \\ S'_{VH} \\ S'_{VV} \end{bmatrix}, \quad \mathbf{s} = \begin{bmatrix} S_{HH} \\ S_{HV} \\ S_{VH} \\ S_{VV} \end{bmatrix}$$

$$S'_{HH} = S_{HH}\cos^2\Omega - S_{VV}\sin^2\Omega \tag{2.6a}$$

$$S'_{HV} = S_{HV} + (S_{HH} + S_{VV})\sin\Omega\cos\Omega \tag{2.6b}$$

$$S'_{VH} = S_{HV} - (S_{HH} + S_{VV})\sin\Omega\cos\Omega \tag{2.6c}$$

$$S'_{VV} = S_{VV}\cos^2\Omega - S_{HH}\sin^2\Omega \tag{2.6d}$$

where it must be remembered that backscatter reciprocity property holds ($S_{HV} = S_{VH}$). The Faraday angle Ω is given by:

$$\Omega[rad] = k\frac{B}{f^2}TEC \tag{2.7}$$

where k is a constant, B is the geomagnetic field and TEC is the Total electron content relative to the travelled path. The expression is again dependent on the satellite spatio-temporal coordinates as well as on the beam parameters such as the frequency and the look angle. Whereas at C-Band wavelength the rotation hardly exceeds 1°, at P-band frequencies, high latitudes and high solar activity the angle can exceed a full 2π cycle. Among the consequences of the rotation, the most evident is the loss of the backscatter reciprocity. Only a few scattering mechanisms are not sensitive to the distortion, maintaining their original polarimetric signature. These are the eigentargets $\mathbf{v}_k$ of the transformation (2.5), in formulas:

$$\mathbf{H_F}\mathbf{v}_k = \lambda_k \mathbf{v}_k \,, \qquad k = 1, 2, 3, 4$$

$$\mathbf{v}_1 = \frac{1}{\sqrt{2}} \begin{bmatrix} 1 \\ 0 \\ 0 \\ -1 \end{bmatrix}, \ \mathbf{v}_2 = \frac{1}{\sqrt{2}} \begin{bmatrix} 0 \\ 1 \\ 1 \\ 0 \end{bmatrix}, \ \mathbf{v}_3 = \frac{1}{2} \begin{bmatrix} -j \\ 1 \\ -1 \\ -j \end{bmatrix}, \ \mathbf{v}_4 = \frac{1}{2} \begin{bmatrix} j \\ 1 \\ -1 \\ j \end{bmatrix} \tag{2.8}$$

$$\lambda_1 = 1, \quad \lambda_2 = 1, \quad \lambda_3 = e^{j\Omega}, \quad \lambda_4 = e^{-j\Omega} \tag{2.9}$$

where λ_k are the associated eigenvalues with unitary amplitude, thus in agreement with the pure rotative nature of the distortion. Notice that $\mathbf{v}_3$ and $\mathbf{v}_4$ cannot be associated to physically consistent scatterers (the reciprocity condition is not satisfied), whereas the first two eigentargets refer to the class of the rotated dihedrals, or, more generally, to the ideal even-bounce scattering mechanisms. With reference to the Pauli coherent decomposition [7], it is then easily inferred that the estimation of the Faraday rotation relies on the odd-bounce component of the scene.

A more physical insight on the phenomenon is achieved by considering that the eigenmodes of the ionospheric distortion are the left and right circular polarizations. This means that the circular components of a polarized wave suffer from different delays, and therefore their downstream recomposition generates corruption in both the amplitude and phase of the original modes. It is easily demonstrated that with the circular bases the backscatter matrix takes the expression:

$$\begin{aligned} \begin{bmatrix} S'_{RR} & S'_{LR} \\ S'_{RL} & S'_{LL} \end{bmatrix} &= \begin{bmatrix} e^{-j\Omega} & 0 \\ 0 & e^{j\Omega} \end{bmatrix} \cdot \begin{bmatrix} S_{RR} & S_{LR} \\ S_{RL} & S_{LL} \end{bmatrix} \cdot \begin{bmatrix} e^{j\Omega} & 0 \\ 0 & e^{-j\Omega} \end{bmatrix} \\ &= \begin{bmatrix} S_{RR} & e^{-j2\Omega} S_{LR} \\ e^{j2\Omega} S_{RL} & S_{LL} \end{bmatrix} \end{aligned} \tag{2.10}$$

where R and L refer to the right and left-handed circular polarizations respectively. One of the most effective methods for evaluating Ω, originally proposed by Bickel and Bates in [2], consists then in recording the phase difference between the cross-pol channels:

$$\Omega = \frac{1}{4} \left[\arg S'_{RL} - \arg S'_{LR} \right] . \tag{2.11}$$

Table 2.1: *Faraday rotation effects: equivalent cross-talk level for small Ω residuals*

Ω Residual [deg]	Equiv. CT [dB]
0.5	-41
1	-35
2	-29
5	-21
10	-15
20	-10

Table 2.2: *Distortion requirements for a polarimetric SAR system.*

Parameter		Max tolerated
Polarimetric amplitude imbalance	$\lvert f\rvert$	±0.2 [dB]
Polarimetric relative phase calibration	$\angle f$	$\pm 5^\circ$
Polarimetric cross-talk error	$\lvert\delta\rvert$	-30 [dB]

by exploiting the reciprocity $S_{LR} = S_{RL}$. Though the procedure is indeed trivial and is hindered by a $\pi/2$ ambiguity it still represents one of the most solid estimators. Faraday rotation residuals after mitigation by means of (2.11) or by any other estimator introduce channel cross-coupling and radiometric fluctuations. For small residuals the most significant effect is indeed the first one. The amount of distortion is expressed in Table 2.1 in terms of equivalent cross-talk level. A cross-talk constraint of -20 dB demands a Faraday estimation accuracy of 5°, whereas a stricter -30 dB requirements would bring the acceptable error down to 2°. Notice also that the Faraday model in (2.4) carries a π intrinsic ambiguity, that do not depend on the specific algorithm adopted.

2.1.3 Polarimetric quality requirements

The accuracy requirements for the each distortion parameter are in general agreed by the scientific community as a result of several assessment efforts such as [11, 30, 32] to name a few. Some common requirements for a polarimetrically calibrated system are reported in Table 2.2. The maximum tolerated Faraday angle is easily attained by Table2.1 for a finely calibrated system (CTs dominated by Faraday), differently, the reader is referred to more detailed investigations such as [30].

The calibration accuracy demanded by a specific SAR application is trivially dependent on the sensitivity of the geophysical information to the distortion residual. Consider to this regard that eventual biases arising from inaccuracies in the modeling of the geophysical parameter within the SAR data cannot be detected and avoided. In most cases though, such issue can be assumed negligible. The most common parameter retrieval scenario involves monotonic relationships between the amplitude of a particular polarization mode and the physical quantity. In the most generic polarimetric case, the unperturbed field measure is obtained from the true backscatter matrix S through polarization synthesis:

$$V = \mathbf{h_r}^H \mathbf{S} \mathbf{h_t}, \qquad P = VV^* \tag{2.12}$$

where V is the field associated to the desired polarization mode, $\mathbf{h_r}, \mathbf{h_t}$ are the polarization vectors of the Rx and Tx antennas, and P is the ideal field power. When the investigation is applied to a distributed scatterer, the field power must be necessarily replaced with the ensemble average

$$P = \langle VV^* \rangle \tag{2.13}$$

Let now define P_d as the power derived from the distorted observation $V_d = \mathbf{h_r}^H \mathbf{M} \mathbf{h_t}$ as a result of (2.1) and (2.4). The normalized radiometric RMS Γ induced by the polarimetric distortion can then be theoretically assessed through:

$$\Gamma = \sqrt{\frac{E\left[(P_d - P)^2\right]}{E\left[P^2\right]}} \tag{2.14}$$

where the mean operator $E\left[\cdot\right]$ accounts for the scatterer irregularities due to the finite number of looks used in (2.13) and the in-scene scatterer diversity. Expression (2.14) is indeed similar to the metric formalized by Dubois in [11], the only difference being that this latter integrates the squared powers and the squared power differences (numerator and denominator) over the complete sets of possible polarization setups of the system. The proposed metric has been exploited to assess the maximum tolerable Faraday rotation over a typical P-Band forest scenario. The error registered by the HH,HV,VV polarizations has been simulated and shown in 2.2 for a typical P-Band symmetric (like- and cross-pol components uncorrelated) forest scatterer [12]. As expected, the greatest distortion is recorded by the HV channel, which, amongst the three, has the weakest backscatter return but that also registers the highest correlation with the biomass volume [23]. The results points to the fact that the error on the Faraday angle estimates must be restrained into a $\pm 2^\circ$ interval in order to achieve a biomass accuracy better than -10 dB. By comparing the commented results with the theoretical isolation in Table 2.1, it can be easily sensed that when higher biomass accuracy is required the -30 dB constraint on the CT level is not sufficient for the HV channel.

2.1.4 Polarimetric calibration: a brief overview on the state of the art

The complete distortion model for a polarimetric observation from (2.1) and (2.4) is then given by:

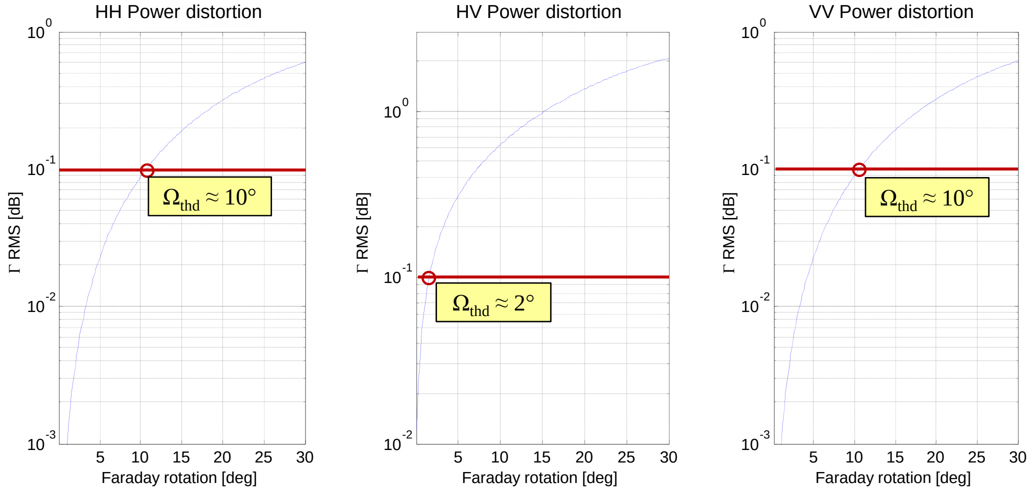

Figure 2.2: *Normalized RMS error for the three different linear polarization modes as a function of the Faraday angle* Ω *.*

$$\mathbf{M} = \begin{bmatrix} M_{HH} & M_{VH} \\ M_{HV} & M_{VV} \end{bmatrix} = A \cdot e^{j\phi} \begin{bmatrix} 1 & \delta_2 \\ \delta_1 & f_1 \end{bmatrix} \begin{bmatrix} \cos\Omega & \sin\Omega \\ -\sin\Omega & \cos\Omega \end{bmatrix} \begin{bmatrix} S_{HH} & S_{VH} \\ S_{HV} & S_{VV} \end{bmatrix} \cdot$$

$$\cdot \begin{bmatrix} \cos\Omega & \sin\Omega \\ -\sin\Omega & \cos\Omega \end{bmatrix} \begin{bmatrix} 1 & \delta_3 \\ \delta_4 & f_2 \end{bmatrix} + \begin{bmatrix} N_{HH} & N_{VH} \\ N_{HV} & N_{VV} \end{bmatrix} \qquad (2.15)$$

In its compact form:

$$\mathbf{M} = A \cdot e^{j\phi} \cdot \mathbf{R}^T \cdot \mathbf{R_F} \cdot \mathbf{S} \cdot \mathbf{R_F} \cdot \mathbf{T} + \mathbf{N}. \qquad (2.16)$$

Depending on the system design and sensor frequency a few approximations can eventually be applied to (2.15). For instance, depending on the frequency and on the acquisition latitude and time the FRA can be assumed null: this is certainly the case of C-Band and higher frequencies but also of L-Band systems at near-equatorial latitudes and at low solar activity periods [42, 43]. A common simplification for spaceborne SAR systems regards the CT quality. In [16] their contribute is indeed considered negligible in modern well-isolated systems (with claimed values better than -30 dB) and thus omitted from (2.15), whereas the Rx-Tx reciprocity explained in (2.3), is hypothesized in the work of van Zyl [49], and in other following contributes. Among these latter, the insightful assessment in [45], that validates the PALSAR quality by means of the van Zyl algorithm, and the original solution proposed in [19] to solve the polarimetric problem in presence of small FRA, are certainly noteworthy. A full system distortion model, with no specific treatment of FRAs, is instead addressed by the reference work of Quegan [38], where no calibrated target is used, and by the recent L-Band calibration approach of Shimada [42], where the joint exploitation of the spectral structure of a distributed target (the Amazon forest) and a calibrated target (a trihedral or a reference natural surface) is assessed for the PALSAR calibration.

Since the polarimetric accuracy of recent L-band and forthcoming P-band systems can be severely degraded by uncorrected Faraday rotations [52], a significant research activity has been recently committed to the investigation and the handling of such effects [33]. As a result, a few notable approaches [5, 16] have been proposed in order to provide valid alternatives with respect to the reference Bickel and Bates estimator [2]. All these techniques, including [2], can be conveniently performed on a natural distributed scatterer, though the underlying assumption is that the system distortion has been removed from the data. The impact of the eventual miscalibration (crosstalk and imbalance residual effects) on the FRA estimation have been therefore properly evaluated in [5], reporting a varying robustness of each estimator with regard to the amplitudes and phases of the distortion residuals.

2.2 The calibrator equations

Identically to the scattering vector $\mathbf{s}$ in (2.5), let here define the observation and noise vectors as

$$\mathbf{m} = \text{vec}(\mathbf{M}) = \begin{bmatrix} M_{HH} \\ M_{HV} \\ M_{VH} \\ M_{VV} \end{bmatrix}, \qquad \mathbf{n} = \text{vec}(\mathbf{N}) = \begin{bmatrix} N_{HH} \\ N_{HV} \\ N_{VH} \\ N_{VV} \end{bmatrix}. \tag{2.17}$$

The model in (2.15) can then be conveniently rephrased into the equation system:

$$\mathbf{m} = A \cdot e^{j\phi} \cdot \mathbf{H} \cdot \mathbf{s} + \mathbf{n} \tag{2.18}$$

where $\mathbf{H}$, hereby referred to as polarimetric distortion matrix (PDM), is the 4 by 4:

$$\mathbf{H} = \left(\mathbf{T}^T \otimes \mathbf{R}^T\right) \cdot \mathbf{H_F} \tag{2.19}$$

with:

$$\mathbf{T}^T \otimes \mathbf{R}^T = \begin{bmatrix} 1 & \delta_2 & \delta_4 & \delta_2\delta_4 \\ \delta_1 & f_1 & \delta_1\delta_4 & \delta_4 f_1 \\ \delta_3 & \delta_2\delta_3 & f_2 & \delta_2 f_2 \\ \delta_1\delta_3 & \delta_3 f_1 & \delta_1 f_2 & f_1 f_2 \end{bmatrix} \tag{2.20}$$

With regard to the problem cardinality, the overall number of real unknowns in the most generic PDM calibration problem amounts to 13, more specifically:

- 4 for the complex f_1 and f_2
- 8 for the complex $\delta_1, \delta_2, \delta_3, \delta_4$
- 1 for the real Ω

whereas the number of equations depends on the specific site used for the calibration.

2.2.1 Distributed targets

When a DT is used, the distortion information is extracted from the second order statistic of the observation, i.e. the covariance matrix. Depending on the a-priori information on the target, a few assumptions can eventually be done on its covariances. The most common ones [16, 38, 49], that will be identically adopted in our analysis, are:

1. Reciprocity, $S_{HV} = S_{VH}$, which is indeed a basic physical property for a monostatic system
2. Azimuthal symmetry, leading to $\langle S_{HV} S_{HH}^* \rangle = \langle S_{HV} S_{VV}^* \rangle = 0$.

This latter condition represents a solid assumption when the number of samples used for the ensemble average is large enough and when the target, in the case of low frequency systems, is distributed on flat or zero-mean sloped areas [26]. Such behavior is explained through the application of the second-order Born approximation to a layer of randomly positioned particles. The result is that the like- and cross-polarized elements of the scattering matrix are completely uncorrelated [4]. This is because the cross-polarized terms come entirely from higher-order scattering (two-bounce or greater), while the like-polarized terms usually come predominately from first-order scattering (single-bounce). For randomly positioned scatterers the higher-order scattering paths are independent of the first-order scattering paths and thus, the cross- and like-polarized terms of the scattering matrix are uncorrelated.

The covariance of the distorted observation, neglecting in this first theoretical analysis the noise, becomes:

$$\mathbf{C} = [C_{mn,pq}] = A^2 \mathbf{H} \mathbf{C_S} \mathbf{H}^H \tag{2.21}$$

where $m, n, p, q = h, v$ stand for the polarization indexes and $\mathbf{C_S}$ is the target covariance. As a result of assumptions 1 and 2 this latter is described by

$$\mathbf{C_S} = \begin{bmatrix} \sigma_{hh} & 0 & 0 & \rho^* \\ 0 & \sigma_{hv} & \sigma_{hv} & 0 \\ 0 & \sigma_{hv} & \sigma_{hv} & 0 \\ \rho & 0 & 0 & \sigma_{vv} \end{bmatrix} \tag{2.22}$$

with σ_{hh},σ_{hv} ,σ_{vv} being the power in each channel and ρ being the co-pol covariance. Note that there is a coefficient ambiguity between σ_{pq}, ρ and the data $C_{mn,pq}$, making the gain A impossible to discriminate from σ_{pq}, ρ.

The number of real equations provided by (2.21) is 16 (4 real diagonal elements and 6 complex out-of-diagonal covariances), though it must be considered that the 5 parameters (3 real and 1 complex value) in (2.22) must be accounted for as unknowns of the inversion problem as well. By using the DT alone we would therefore have 16 equations for the retrieval of 18 total parameters, yielding an ill-posed problem.

2.2.2 Calibrated point targets

By adding to the calibration scene one or more point targets (PTs) with known polarimetric signatures we obtain 8 more equations for each target. The targets can be either corner reflectors (CR), with trihedrals being the most convenient choice with regard to the orientation accuracy, or the more expensive polarimetric active radar calibrators (PARC). The ideal scattering matrix of a trihedral with a σ_{CR} RCS is:

$$\mathbf{S}_{CR} = \sqrt{\sigma_{CR}} \begin{bmatrix} 1 & 0 \\ 0 & 1 \end{bmatrix} \tag{2.23}$$

and provides the additional set of complex equations:

$$\begin{aligned} M_{HH}^{(CR)} =& A \cdot \sqrt{\sigma_{CR}} \cdot e^{j\phi} \left[(1-\delta_2\delta_4) \cdot \cos 2\Omega + (\delta_4 - \delta_2) \cdot \sin 2\Omega\right] \\ M_{HV}^{(CR)} =& A \cdot \sqrt{\sigma_{CR}} \cdot e^{j\phi} \left[(\delta_1 - \delta_4 f_1) \cdot \cos 2\Omega + (\delta_1\delta_4 - f_1) \cdot \sin 2\Omega\right] \\ M_{VH}^{(CR)} =& A \cdot \sqrt{\sigma_{CR}} \cdot e^{j\phi} \left[(\delta_3 - \delta_2 f_2) \cdot \cos 2\Omega + (f_2 - \delta_2\delta_3) \cdot \sin 2\Omega\right] \\ M_{VV}^{(CR)} =& A \cdot \sqrt{\sigma_{CR}} \cdot e^{j\phi} \left[(\delta_1\delta_3 - f_1 f_2) \cdot \cos 2\Omega + (\delta_1 f_2 - \delta_3 f_1) \cdot \sin 2\Omega\right] \end{aligned} \tag{2.24}$$

where the noise has been again omitted. Typical transponder signatures [15] for an effective CT quality assessment are for instance:

$$\mathbf{S}_{PARC_{HV}} = \sqrt{\sigma_{PARC}} \begin{bmatrix} 0 & 0 \\ 1 & 0 \end{bmatrix} \qquad \mathbf{S}_{PARC_{VH}} = \sqrt{\sigma_{PARC}} \begin{bmatrix} 0 & 1 \\ 0 & 0 \end{bmatrix} \tag{2.25}$$

though other PARC solutions can be employed as well. It is straightforward noticing that active calibrators do not respect the scattering reciprocity that applies to the passive reflectors. It must be then remarked that the phase ϕ must be added to the parameters list when the calibration relies on the first order information, whereas its estimation can be avoided when, identically to (2.21), the second order information is used instead. In this latter case the nature of the information can either be punctual, i.e. the peak value of the IRF after a proper pixel interpolation (the same referred to in (2.24)):

$$\mathbf{C}^{(PT)} = A^2 \mathbf{H} \mathbf{S}_{PT} \mathbf{S}_{PT}^H \mathbf{H}^H. \tag{2.26}$$

or evaluated from the integration [15] of a convenient area I_{PT} around the target peak, which leads to:

$$\mathbf{C}^{(PT)} = \sum_{(r,x) \in I_{PT}} \sum \mathbf{m}_{PT}(r,x) \mathbf{m}_{PT}^H(r,x). \tag{2.27}$$

where r, x are the range and azimuth coordinates. Note that I_{PT} must be chosen so that the system IRF integral is almost 1 (all the side lobes giving a significant contribute must be included), and that the noise produced by the ground clutter (here not explicitly addressed) requires some treatment since the summation degrades the SCR quality of the target. Assuming that the ground reflectivity is homogenous around the PT, an effective method would be that of subtracting to (2.27) the covariance estimated over a neighboring area.

2.3 Assessment of the model sensitivity

2.3.1 Methodology

The estimation of the distortion parameters is often a complicated task since the equation sets (2.21),(2.24) are non-linear and the retrieval of closed-form expressions is in general not feasible. Our analysis aims to provide a useful insight on a restricted number of calibration scenarios, focusing on determining the solvability of the problem around some realistic work points, not being able to explore by sampling the whole parameters domain. In other words the methodology proposes to verify the existence of the solution though it cannot guarantee for its uniqueness.

The feasibility of PDM retrieval, given a specific calibration site and distortion model, is investigated through linearization of the system equations in some convenient distortion configurations. Let $\mathbf{Y} = [y_1 \cdots y_{N_{eq}}]^T$ be the vector with the N_{eq} real distorted data, and $\mathbf{X} = [x_1 \cdots x_{N_{par}}]^T$ the vector with the N_{par} real unknowns. This latter are represented by the distortion parameters in (2.15) and by the unknown covariance elements of the DT in (2.22). On the other side, the data $\mathbf{Y}$ comprise the measured (distorted) DT covariance elements and the PT first or second order information, when the point target is included in the calibration scenario. They are related through the generic non-linear functionals g:

$$\mathbf{Y} = g(\mathbf{X}) = \begin{bmatrix} g_1(\mathbf{X}) \\ \vdots \\ g_{N_{eq}}(\mathbf{X}) \end{bmatrix}. \tag{2.28}$$

For a specific $\mathbf{X}_0$, the solution ambiguities in its proximity can be investigated through the function Jacobian $\mathbf{J}$:

$$\mathbf{d_Y} = \mathbf{Y} - \mathbf{Y}_0 = \begin{bmatrix} \left.\frac{dg_1(\mathbf{X})}{dx_1}\right|_{\mathbf{X}_0} & \cdots & \left.\frac{dg_1(\mathbf{X})}{dx_{N_{par}}}\right|_{\mathbf{X}_0} \\ \vdots & \ddots & \\ \left.\frac{dg_{N_{eq}}(\mathbf{X})}{dx_1}\right|_{\mathbf{X}_0} & & \left.\frac{dg_{N_{eq}}(\mathbf{X})}{dx_{N_{par}}}\right|_{\mathbf{X}_0} \end{bmatrix} \cdot (\mathbf{X} - \mathbf{X}_0) = \mathbf{J} \cdot \mathbf{d_X}. \tag{2.29}$$

In particular, it is trivial demonstrating that when $\mathbf{J}$ has a nullspace, the parameters associated to this latter are not determinable. This kind of analysis is readily performed through the Singular Value Decomposition:

$$\mathbf{J} = \mathbf{U}\mathbf{\Lambda}\mathbf{V}^T = \begin{bmatrix} \mathbf{u}_1 & \cdots & \mathbf{u}_{N_{eq}} \end{bmatrix} \Lambda \begin{bmatrix} \mathbf{v}_1 & \cdots & \mathbf{v}_{N_{par}} \end{bmatrix}^T \tag{2.30}$$

where the components $\mathbf{v}_i$ in the space of the model associated to the null singular values of $\mathbf{\Lambda}$ cannot be resolved. Notice that the transpose operator has been used on $\mathbf{V}$ instead of the Hermitian operator since all of the quantities have been decomposed into their real valued contributes (real and imaginary parts in the data and amplitude and phase components for the model). An example of the SVD qualitative effectiveness in the interpretation of the model sensitivity is provided by the panels in Fig. 2.3 and Fig. 2.4. The most trivial model scenario (CT and FRA null) is approached by a DT-alone calibration and by a DT+CR calibration. It is clear that in the first case the problem is ill-posed because of the two null singular values associated to the sum of the imbalance phases and the sum of their moduli. The differences in the phase and modulus are instead well resolved, as conveyed by the 5° and 7° singular vectors. In Fig. 2.3 the same analysis applied to a scenario where a corner shows that all components can be determined as expected.

It is evident that such methodology cannot ensure the uniqueness of the solution in the whole $\mathbf{X}$ domain. Instead, it brings evidence of its existence, meaning that the correct PDM represents a local optimum in the parameters domain. It can be inferred that when some consistent a-priori information on the PDM is available (e.g. assuming slow

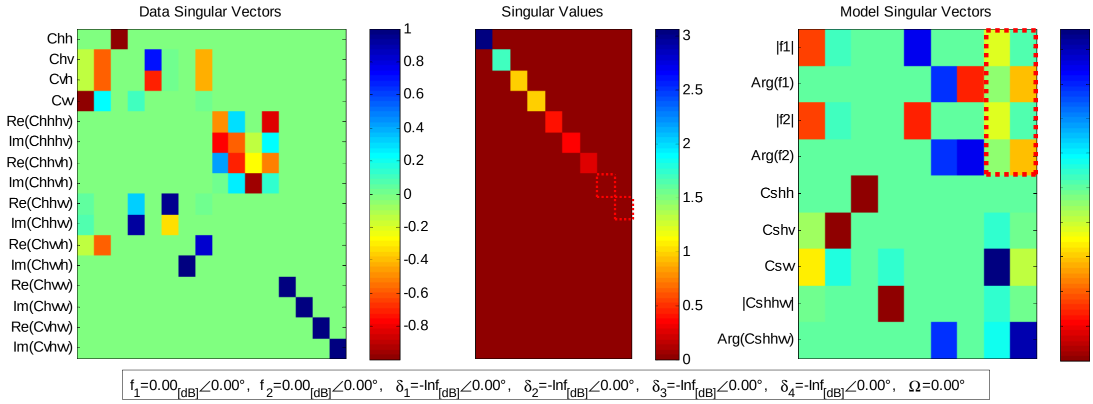

Figure 2.3: *SVD analysis in a DT calibration site with null CTs and FRA. The system, that has been linearized around the ideal PDM (no distortion), shows in particular two null singular values and the associated model nullspace both marked with red dotted squares.*

miscalibration with respect to the previously estimated PDMs and estimating the FRA a-priori from TEC maps), a numerical solver (see section 2.5) can be employed in order to converge to the correct solution.

Besides, when the problem is well-posed (in its local linearized form (2.29)) a the model uncertainty can be conveniently assessed. Its derivation is readily provided by the parameter MSE matrix $\mathbf{C_X}$ that is attainable by means of the simple passage:

$$E\left[\mathbf{d_Y}\mathbf{d_Y}^T\right] = \mathbf{J}\cdot E\left[\mathbf{d_X}\mathbf{d_X}^T\right]\cdot\mathbf{J}^T \Longrightarrow \mathbf{C_Y} = \mathbf{J}\cdot\mathbf{C_X}\cdot\mathbf{J}^T \tag{2.31}$$

$$\mathbf{C_X} = \mathbf{J}^{\dagger}\cdot\mathbf{C_Y}\cdot\mathbf{J}^{\dagger T} \tag{2.32}$$

where $\mathbf{J}^{\dagger}$ is the Jacobian pseudo-inverse and $\mathbf{d_Y}$ must be referred to as $\mathbf{d_Y} = \hat{\mathbf{Y}} - \mathbf{Y}_0$, i.e. the deviation of the measured values $\hat{\mathbf{Y}}$ with respect to the expected distorted ones $\mathbf{Y}_0$, with $\mathbf{C_Y}$ thus representing the data MSE matrix.

2.3.1.1 DT model uncertainty

With concern to the DT, $\mathbf{C_Y}$ is a quantity which depends on the number of averaged targets N_p and on the model deviation from (2.21) and (2.22), which comprise the NESZ disturbance and the lack of orientation symmetry. Its retrieval is readily shown. With reference to DT calibration let define then the observed scattering vectors as

$$\mathbf{m}_i \sim CN(0, \mathbf{C_M} = \mathbf{C}{+}\mathbf{C_n}) \tag{2.33}$$

and the real $N_{eq} = 16$ equations data as:

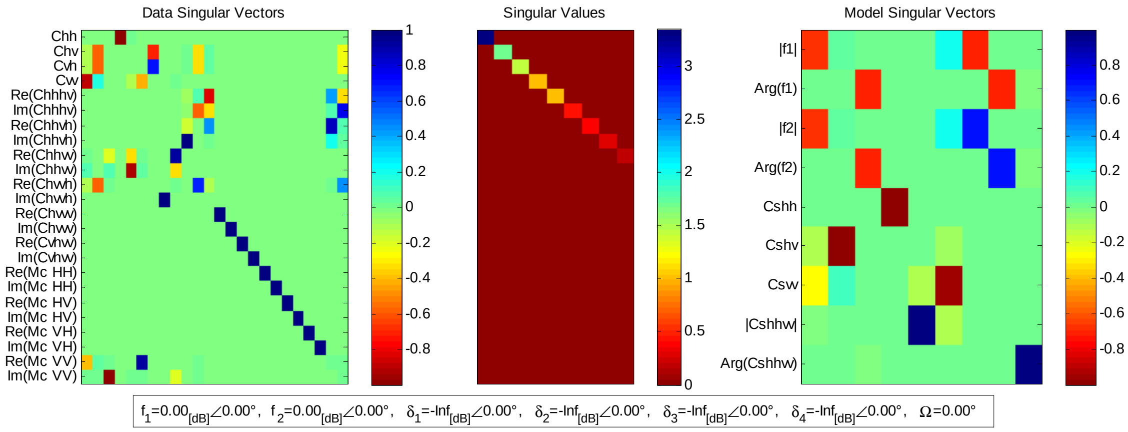

Figure 2.4: *SVD analysis in a DT+CR calibration site with null CTs and FRA. The system, linearized around the ideal PDM (no distortion), is well-posed since no null singular values has been attained.*

$$\bar{\mathbf{Y}} = \underbrace{\mathbf{P}\cdot\mathrm{vec}\left(\begin{bmatrix}\mathcal{R}\left(\mathbf{C}\right)\\ \mathcal{I}\left(\mathbf{C}\right)\end{bmatrix}\right)}_{\mathbf{Y}_0} + \underbrace{\mathbf{P}\cdot\mathrm{vec}\left(\begin{bmatrix}\mathcal{R}(\mathbf{C_n})\\ \mathcal{I}(\mathbf{C_n})\end{bmatrix}\right)}_{\mathbf{Y}_n} \tag{2.34}$$

$$\hat{\mathbf{Y}} = \mathbf{P}\cdot\mathrm{vec}\left(\begin{bmatrix}\mathcal{R}\left(\hat{\mathbf{C}}\right)\\ \mathcal{I}\left(\hat{\mathbf{C}}\right)\end{bmatrix}\right) \tag{2.35}$$

where $\mathbf{C_n}$ is the covariance deviation from the model $\mathbf{C}$, $\mathbf{P}$ is the 16×32 binary matrix in (2.38) that limits the number of real elements (32 overall) to the 16 informative ones[1],

---

[1]

$$\mathcal{R}\left(\mathbf{C}\right) = \begin{bmatrix}\mathbf{c_1} & \mathbf{c_5} & \mathbf{c_9} & \mathbf{c_{13}}\\ c_2 & \mathbf{c_6} & \mathbf{c_{10}} & \mathbf{c_{14}}\\ c_3 & c_7 & \mathbf{c_{11}} & \mathbf{c_{15}}\\ c_4 & c_8 & c_{12} & \mathbf{c_{16}}\end{bmatrix}, \mathcal{I}\left(\mathbf{C}\right) = \begin{bmatrix}c_{17} & \mathbf{c_{21}} & \mathbf{c_{25}} & \mathbf{c_{29}}\\ c_{18} & c_{22} & \mathbf{c_{26}} & \mathbf{c_{30}}\\ c_{19} & c_{23} & c_{27} & \mathbf{c_{31}}\\ c_{20} & c_{24} & c_{28} & c_{32}\end{bmatrix} \Rightarrow \mathrm{vec}\left(\begin{bmatrix}\mathcal{R}\left(\mathbf{C}\right)\\ \mathcal{I}\left(\mathbf{C}\right)\end{bmatrix}\right) = \begin{bmatrix}c_1\\ \vdots\\ c_{32}\end{bmatrix} \tag{2.36}$$

$$\tag{2.37}$$

$$\mathbf{P} = \begin{array}{c}\begin{array}{cccccccccccc}1 & 2 & 3 & 4 & 5 & 6 & \cdots & 29 & 30 & 31 & 32 & \\ \end{array}\\ \left[\begin{array}{ccccccccccc}1 & 0 & 0 & 0 & 0 & 0 & & 0 & 0 & 0 & 0\\ 0 & 0 & 0 & 0 & 1 & 0 & \cdots & 0 & 0 & 0 & 0\\ 0 & 0 & 0 & 0 & 0 & 1 & & 0 & 0 & 0 & 0\\ & & & \vdots & & & \ddots & & & \vdots & \\ 0 & 0 & 0 & 0 & 0 & 0 & \cdots & 0 & 1 & 0 & 0\\ 0 & 0 & 0 & 0 & 0 & 0 & & 0 & 0 & 1 & 0\end{array}\right]\begin{array}{c}1\\ 2\\ 3\\ \vdots\\ 15\\ 16\end{array}\end{array} \tag{2.38}$$

and

$$\hat{\mathbf{C}} = \frac{1}{N_p}\sum_i \mathbf{m}_i \mathbf{m}_i^H \tag{2.39}$$

is the estimated covariance matrix with Wishart distribution. The expression of $\mathbf{C_Y}$ is then:

$$\mathbf{C}_{\mathbf{Y}}^{(DT)} = E\left[\left(\hat{\mathbf{Y}} - \mathbf{Y}_0\right)\left(\hat{\mathbf{Y}} - \mathbf{Y}_0\right)^T\right] = E\left[\hat{\mathbf{Y}}\hat{\mathbf{Y}}^T\right] - E\left[\hat{\mathbf{Y}}\right]\mathbf{Y}_0^T - \mathbf{Y}_0 E\left[\hat{\mathbf{Y}}\right]^T + \mathbf{Y}_0\mathbf{Y}_0^T \tag{2.40}$$

that, by exploiting the unbiasedness $E\left[\hat{\mathbf{Y}}\right] = \bar{\mathbf{Y}}$, becomes:

$$\begin{aligned}\mathbf{C}_{\mathbf{Y}}^{(DT)} &= E\left[\hat{\mathbf{Y}}\hat{\mathbf{Y}}^T\right] - \mathbf{Y}_0\mathbf{Y}_0^T - \mathbf{Y}_n\mathbf{Y}_0^T - \mathbf{Y}_0\mathbf{Y}_n^T \\ &= E\left[\hat{\mathbf{Y}}\hat{\mathbf{Y}}^T\right] - \bar{\mathbf{Y}}\bar{\mathbf{Y}}^T + \mathbf{Y}_n\mathbf{Y}_n^T \\ &= \Gamma + \mathbf{Y}_n\mathbf{Y}_n^T\end{aligned} \tag{2.41}$$

where the elements of Γ can be evaluated through the closed-form expressions in appendix A.1. Notice that the uncertainty in the measurement depending on the number of looks is represented by Γ whereas the model deviations are accounted for within $\mathbf{Y}_n\mathbf{Y}_n^T$.

2.3.1.2 PT model uncertainty

In the PT case the error on the measured data $\hat{\mathbf{m}}$ is determined by inaccuracies in the target deployment and manufacturing (i.e. errors in the orientation and in the polarimetric signature), hereby referred to as average polarimetric noise (APN), and by the clutter and thermal noises superimposed to the target signal. All these error sources have been modeled into a single noise process, with zero-mean and gaussian distribution. In formulas:

$$\hat{\mathbf{m}}^{(PT)} = \mathbf{m}^{(PT)} + \mathbf{n}^{(PT)}, \quad \mathbf{n}^{(PT)} \sim \mathcal{CN}\left(0, \mathbf{C}_{\mathbf{N}}^{(PT)}\right) \tag{2.42}$$

$$\mathbf{C}_{\mathbf{Y}}^{(PT)} = \frac{1}{2}\begin{bmatrix} \mathcal{R}\left(\mathbf{C}_{\mathbf{N}}^{(PT)}\right) & -\mathcal{I}\left(\mathbf{C}_{\mathbf{N}}^{(PT)}\right) \\ \mathcal{I}\left(\mathbf{C}_{\mathbf{N}}^{(PT)}\right) & \mathcal{R}\left(\mathbf{C}_{\mathbf{N}}^{(PT)}\right)\end{bmatrix} \tag{2.43}$$

Since the errors on the DT measures and those on a calibrated targets are uncorrelated, the full $\mathbf{C_Y}$ of a hybrid DT+PT scenario is:

$$\mathbf{C}_{\mathbf{Y}} = \begin{bmatrix} \mathbf{C}_{\mathbf{Y}}^{(DT)} & \mathbf{0} \\ \mathbf{0} & \mathbf{C}_{\mathbf{Y}}^{(PT)} \end{bmatrix} \tag{2.44}$$

which will be employed in the sensitivity analysis presented in section 2.3.2. It should be noted that the cross-correlation terms in $\mathbf{C}_{\mathbf{Y}}$ are not null when the noise in (2.42) has a non-zero mean $\overline{\mathbf{N}}$. In such case (2.44) would take the form:

$$\mathbf{C}_{\mathbf{Y}} = \begin{bmatrix} \mathbf{C}_{\mathbf{Y}}^{(DT)} & \mathbf{Y}_n^{(DT)}\mathbf{Y}_n^{(PT)T} \\ \mathbf{Y}_n^{(PT)}\mathbf{Y}_n^{(DT)T} & \mathbf{C}_{\mathbf{Y}}^{(PT)} \end{bmatrix} \tag{2.45}$$

with

$$\mathbf{Y}_n^{(PT)} = \begin{bmatrix} \mathcal{R}\left(\overline{\mathbf{N}}^{(PT)}\right) \\ \mathcal{I}\left(\overline{\mathbf{N}}^{(PT)}\right) \end{bmatrix}$$

$$\mathbf{C}_{\mathbf{Y}}^{(PT)} = \frac{1}{2}\begin{bmatrix} \mathcal{R}\left(\mathbf{C}_{\mathbf{N}}\right) & -\mathcal{I}\left(\mathbf{C}_{\mathbf{N}}\right) \\ \mathcal{I}\left(\mathbf{C}_{\mathbf{N}}\right) & \mathcal{R}\left(\mathbf{C}_{\mathbf{N}}\right) \end{bmatrix} + \mathbf{Y}_n^{(PT)}\mathbf{Y}_n^{(PT)T}.$$

It is important to remark that the uncertainty on the model computed with (2.32) does not represent a lower bound on the achievable accuracy, especially in the case of joint calibration (DT+PT). The uncertainty, Δ_i, associated to the real parameter $x_i \in \{|f|, \angle f, |\delta|, \angle\delta, \Omega, A...\}$ is retrieved from the diagonal elements of (2.32) through:

$$\Delta_i = \sqrt{E\left[(x_i - x_{i0})^2\right]} = \sqrt{\mathbf{C}_{\mathbf{X}}(i,i)} \tag{2.46}$$

where it is worth stressing the fact that Δ is an approximate measure (i.e. for small data perturbation) of the absolute model deviation. Its conversion into a multiplicative error measurement (thus on a dB scale) is then approximately obtained by means of $\Delta_{[\mathrm{dB}]} = \frac{20}{\ln 10} \cdot \frac{\Delta}{x}$.

2.3.2 Overview on the estimation feasibility

A representative set of calibration scenarios have been explored by means of the analysis discussed above. The addressed distortion work points (DWP) are shown in Table 2.3: the set comprise the ideal PDM (DWP1), a symmetric Rx/Tx system configuration (DWP2), a reciprocal CT configuration with opposite imbalances (DWP3) and an asymmetric configuration (DWP4). With concern to the estimation models investigated, no hypothesis has been done on the imbalances, i.e. both f_1 and f_2 are always separately estimated, whereas a few different configurations (assumptions) have been tested for the cross-talks (CT) and the Faraday rotation angle (FRA). The first being modeled according to one the the three options:

Table 2.3: *Distortion work points adopted for analysis*

		DWP1	DWP2	DWP3	DWP4
f_1	dB (Linear)	0 (1)	0 (1)	0 (1)	0 (1)
	Phase [deg]	0	0	0	0
f_2	dB (Linear)	0 (1)	0 (1)	0 (1)	0 (1)
	Phase [deg]	0	0	180	0
δ_1	dB (Linear)	$-\infty$ (0)	-30 (0.03)	-30 (0.03)	-30 (0.03)
	Phase [deg]	-	0	-90	0
δ_2	dB (Linear)	$-\infty$ (0)	-30 (0.03)	-30 (0.03)	-30 (0.03)
	Phase [deg]	-	0	90	0
δ_3	dB (Linear)	$-\infty$ (0)	-30 (0.03)	-30 (0.03)	-26 (0.05)
	Phase [deg]	-	0	-90	90
δ_4	dB (Linear)	$-\infty$ (0)	-30 (0.03)	-30 (0.03)	-26 (0.05)
	Phase [deg]	-	0	90	90

1. CT null: $\delta_1 = \delta_2 = \delta_3 = \delta_4 = 0$
2. CT reciprocal: $\delta_1 = \delta_3$, $\delta_2 = \delta_4$
3. CT unknown: δ_1, δ_2, δ_3, δ_4 to be estimated

and the FRA assuming the configurations:

1. FRA null: $\Omega = 0$
2. FRA unknown: Ω to be estimated.

where it can be observed that the criterion adopted does not discriminate between a generic "FRA known" and "FRA unknown" since it is implied that the only case where Faraday is known with the required accuracy is its total absence. The feasibility of the adopted models is investigated on three different sets of equations, i.e. for the calibration sites:

- DT alone: only a homogeneous distributed target is available. It provides the 16 real equations in (2.21) but also introduces 5 more parameters, see (2.22), when the undistorted covariance is unknown.
- DT+PT: a distributed target and a point target are exploited. With regard to the latter one, the analysis will be applied to the trihedral CR since it represents, for its costs and flexibility, one of the most employed solutions. The PT offers 8 additional real equations, see (2.24), and requires the estimation of one/two , $\{A\}/\{A, \phi\}$, additional parameters, depending on whether the first or second order information is used.

A schematic overview on the degrees of freedom that must be issued in each scenario is provided by Table 2.4. For each DWP, only the consistent models have been examined.

Table 2.4: *Schematic characterization of the model scenarios tested in 2.5*

Number of parameters N_{par}		DT ($N_{eq} = 16$)	DT + PT ($N_{eq} = 24$)
		+$\sigma_{hh}, \sigma_{hv}, \sigma_{vv}$,$\rho$	+ $\sigma_{hh}, \sigma_{hv}, \sigma_{vv}$,$\rho$ + A, (+ϕ_{PT})
CT null FRA null	- f_1, f_2	9	10 (11)
CT reciprocal FRA null	- f_1, f_2 - δ_1, δ_2	13	14 (15)
CT unknown FRA null	- f_1, f_2 - δ_1,δ_2,δ_3,δ_4	17	18 (19)
CT null FRA unknown	- f_1, f_2 - Ω	10	11 (12)
CT reciprocal FRA unknown	- f_1, f_2 - δ_1,δ_2 - Ω	14	15 (16)
CT unknown FRA unknown	- f_1, f_2 - δ_1,δ_2,δ_3,δ_4 - Ω	18	19 (20)

It can be observed, for instance, that every model can fit DWP1, though the only “CT unknown” configurations are suited for DWP3. Notice, then, that the employment of a calibrated target indirectly leads to the estimation of the system gain A, thus forcing the radiometric calibration problem into the polarimetric calibration one. A further comment must be spent on the system noise that would ideally contribute with a $\sigma_n \mathbf{I}$ term to the right-hand side of (2.21). The reason behind its exclusion from the list of system unknowns is that it can be estimated independently from all the other parameters, meaning that its impact on the problem feasibility is null. The eigenvalue analysis of the DT covariance matrix leads indeed to the simple relationship:

$$\sigma_n = \min(\lambda_i), \qquad \mathbf{C}^{(DT)} = \sum_{i=1}^{4} \lambda_i \mathbf{u}_i \mathbf{u}_i^H$$

with λ_i and $\mathbf{u}_i$ being respectively the eigenvalues and eigenvectors of DT data covariance $\mathbf{C}^{(DT)}$.

The investigation on the well-posedness of the calibration problem is schematically synthesized in Table 2.5. Each DWP has been tested in two different FRA conditions: $\Omega = 0°$ and $\Omega \neq 0°$. A few points are clearly evidenced by such analysis:

- When the FRA is null (which is the general case of C and X-Band and some particular case in L-Band) the estimation problem in the DT calibration is ill-posed. This behavior holds independently of the distortion workpoint and the model assumptions. Differently, it can be noticed that with a CR all the parameters can be resolved.
- When the FRA is non-null the calibration problem becomes well conditioned in most

of the cases, even for the DT-alone scenario. It can be noticed, though, that in this latter case the feasibility is still affected by the particular DWP, as conveyed by the DWP3 ill-posedness as opposed to the DWP2 sensitivity. The accuracy of the estimates, which obviously depends on the DWP itself and on the quality of the targets employed, is evaluated in the analysis that will follow.

- The full model case, where no assumption is made, cannot be resolved by any of the tested target configurations. This would indeed occur even if additional targets were added to the scene, since the joint radiometric and polarimetric problem is by its own nature ambiguous.

This latter point is indeed worth some further discussion.

Table 2.5: *Feasibility analysis for the DWP set of 2.3*

Well-posedness		DWP1		DWP2		DWP3		DWP4	
		DT	DT + CR	DT	DT + CR	DT	DT + CR	DT	DT + CR
FRA: $\Omega = 0$	CT null FRA null	NO	YES	-	-	-	-	-	-
	CT reciprocal FRA null	NO	YES	NO	YES	NO	YES	-	-
	CT unknown FRA null	NO	YES	NO	YES	NO	YES	NO	YES
	CT null FRA unknown	NO	YES	-	-	-	-	-	-
	CT reciprocal FRA unknown	NO	YES	NO	YES	NO	YES	-	-
	CT unknown FRA unknown	NO	NO	NO	NO	NO	NO	NO	NO
FRA: $\Omega \neq 0$	CT null FRA unknown	YES	YES	-	-	-	-	-	-
	CT reciprocal FRA unknown	YES	YES	YES	YES	NO	YES	-	-
	CT unknown FRA unknown	NO	NO	NO	NO	NO	NO	NO	NO

Note: the table provides information on whether the calibration problem is well-posed (YES), ill-posed (NO) or the model is not consistent with the DWP (-)

2.3.3 Ambiguity to the radiometric coefficient

The mutual impairment between radiometric and polarimetric assessment is readily demonstrated. Let define the arbitrary matrices $\tilde{\mathbf{R}}$, $\tilde{\mathbf{T}}$, and the complex coefficients A_R, A_T as:

$$
\begin{aligned}
&A_R = \cos\Omega - \delta_2 \sin\Omega\\
&A_T = \cos\Omega + \delta_4 \sin\Omega\\
&\tilde{\mathbf{R}} = \begin{bmatrix} 0 & \tilde{\delta}_1 \\ \tilde{\delta}_2 & \tilde{f}_1 \end{bmatrix} = \begin{bmatrix} 0 & \left(\frac{\cos\Omega - A_R}{A_R}\right)\delta_1 - \frac{\sin\Omega}{A_R} f_1 \\ \left(\frac{\cos\Omega - A_R}{A_R}\right)\delta_2 + \frac{\sin\Omega}{A_R} & \left(\frac{\cos\Omega - A_R}{A_R}\right) f_1 + \delta_1 \sin\Omega \end{bmatrix}\\
&\tilde{\mathbf{T}} = \begin{bmatrix} 0 & \tilde{\delta}_3 \\ \tilde{\delta}_4 & \tilde{f}_2 \end{bmatrix} = \begin{bmatrix} 0 & \left(\frac{\cos\Omega - A_T}{A_T}\right)\delta_3 + \frac{\sin\Omega}{A_T} f_2 \\ \left(\frac{\cos\Omega - A_T}{A_T}\right)\delta_4 - \frac{\sin\Omega}{A_T} & \left(\frac{\cos\Omega - A_T}{A_T}\right) f_1 - \delta_3 \sin\Omega \end{bmatrix}.
\end{aligned}
\tag{2.47}
$$

It can be shown then, with reference to (2.15), that:

$$
\begin{aligned}
\mathbf{R^T} \cdot \mathbf{R_F} &= A_R \left(\mathbf{R} + \tilde{\mathbf{R}}\right)^{\mathbf{T}} = A_R \cdot \mathbf{R^T_{tot}}\\
\mathbf{R_F} \cdot \mathbf{T} &= A_T \left(\mathbf{T} + \tilde{\mathbf{T}}\right) = A_T \cdot \mathbf{T_{tot}}
\end{aligned}
\tag{2.48}
$$

yielding:

$$
A \cdot \mathbf{R^T} \cdot \mathbf{R_F} \cdot \mathbf{S} \cdot \mathbf{R_F} \cdot \mathbf{T} = A_{tot} \cdot \mathbf{R^T_{tot}} \cdot \mathbf{S} \cdot \mathbf{T_{tot}} \tag{2.49}
$$

with $A_{tot} = A \cdot A_R \cdot A_T$ being a complex value whose phase is a constant phase term throughout the image that cannot be estimated. Equation (2.49) reads therefore that it is not possible performing external radiometric and full polarimetric calibration at the same time. Such issue would be overcome either by considering the system already radiometrically calibrated or by performing the polarimetric calibration in absence of Faraday rotations [42]. With reference to the the first case a novel feasibility investigation has been conducted where the gain A has been assumed known. The results have been registered in Table 2.6. The difference with respect to Table 2.6 is that the CR can now solve the most complex model (CT unknown, FRA unknown) in DWP4 but not in DWP2 and DWP3, because the problem becomes undetermined for some δ_2, δ_4 combinations, e.g. $\delta_2 = \delta_4$. Note that this asymmetric condition on the CTs is due to the fact that the system has been supposed radiometrically calibrated with respect to the horizontal polarization (its gain is incorporated into the gain A). The same condition would be applied to δ_1 and δ_3 if the vertical polarization had been taken as reference. It should be considered, however, that an error in radiometric calibration could have a significant impact on the retrieval of the other parameters when the full distortion model is adopted.

It is finally important to remark that:

if we do not aim to monitor the system parameters, but rather we just need to calibrated the SAR data, the problem in the physical interpretation of $A_{tot}, \mathbf{R_{tot}}, \mathbf{T_{tot}}$ with respect to $A, \mathbf{R}, \mathbf{T}$ is meaningless. The estimation of the ambiguous set is enough for data calibration. That is indeed a feasible task when a CR is exploited (refer for this case to the "CT unknown, FRA null" scenario in 2.5).

Table 2.6: *Feasibility analysis for the DWP set of 2.3 in a radiometrically calibrated environment.*

Well-posedness Gain A is known		DWP1		DWP3		DWP4	
		DT	DT + CR	DT	DT + CR	DT	DT + CR
FRA: $\Omega = 0$	CT null FRA null	NO	YES	-	-	-	-
	CT reciprocal FRA null	NO	YES	NO	YES	-	-
	CT unknown FRA null	NO	YES	NO	YES	NO	YES
	CT null FRA unknown	NO	YES	-	-	-	-
	CT reciprocal FRA unknown	NO	YES	NO	YES	-	-
	CT unknown FRA unknown	NO	NO*	NO	NO*	NO	YES*
FRA: $\Omega \neq 0$	CT null FRA unknown	YES	YES	-	-	-	-
	CT reciprocal FRA unknown	YES	YES	NO	YES	-	-
	CT unknown FRA unknown	NO	NO*	NO	NO*	NO	YES*

Note: the table provides information on whether the calibration problem is well-posed (YES), ill-posed (NO) or the model is not consistent with the DWP (-). The * refers to the fact that the full model scenario for DWP3 is well-determined because $\delta_2 \neq \delta_4$.

Table 2.7: *Target configuration for the sensitivity analysis.*

Parameter			Value
DT (Forest)	σ_{hh} / σ_{hv} / σ_{vv}	[dB]	0 / -6.5 / 0
	$\rho/\sqrt{\sigma_{hh}\sigma_{vv}}$		$0.4\angle 5°$
Ground Clutter (CR/PARC)	$\sigma_{hh}^{(cl)}$ /$\sigma_{hv}^{(cl)}$ / $\sigma_{vv}^{(cl)}$	[dB]	-10 / -19 / -10
	$\rho^{(cl)}/\sqrt{\sigma_{hh}^{(cl)}\sigma_{vv}^{(cl)}}$	[dB]	$0.6\angle 10°$
NESZ	σ_n	[dB]	-20

2.3.4 Uncertainty analysis on two case studies

A qualitative and quantitative analysis on the local accuracy is now carried out for two significant well-posed distortion scenarios. With concern to the calibrators the simulations has been conducted using for the parameters in Table 2.7, where all the values are expressed with reference to the DT σ_{hh} set at 0 dB. A typical ground clutter noise [18] has been assigned to the calibrated target, and a NESZ disturbance has also been added to both DT and CR. The first assessment is carried out on the PDM model with reciprocal CT and unknown (non-null) FRA (see Table 2.4), i.e. the most complex scenario that can be resolved by a DT alone, whereas the second analysis will be committed to the full system calibration case study in a null FRA environment, where the aid of a CR is instead necessary.

2.3.4.1 CT-reciprocal system in the presence of Faraday rotations

The "CT reciprocal" model represents the most complex system that can be successfully calibrated when the FRA is not negligible. Interestingly, we read from Table 2.6 that a "cheap" DT calibration would be indeed an effective option, though it is also emphasized that there are a few PDMs, such as the one coming from DWP3, that demand the employment of a CR or a PARC. In order to point the investigation into the most significant directions, an exhaustive exploration of the uncertainty behavior with respect to the phase of the PDM parameters is first performed. The amplitudes of the imbalances and of the CT have been fixed to the DWP2-3 values, the FRA has been set to 10° and the uncertainty has been evaluated on $N_p = 10^5$ looks over the ideal (i.e. with perfect azimuthal symmetry) DT in Table 2.7. The results of the exploration, shown in Fig. 2.5 for the $|f_1|$ and $|\delta_1|$ uncertainties ($\Delta_{|f_1|}$,$\Delta_{|\delta_1|}$), clearly evidence that the phase difference $\phi_{f_2 f_1} = \angle f_2 - \angle f_1$ has the strongest impact on sensitivity. As expected, the worst scenario is $\phi_{f_2 f_1} = \pi$, where a few CT configurations (e.g. the DWP3 case) are not solvable. A more synthetic representation is then attained in Fig. 2.6 as a function of $\phi_{f_1 f_2}$ by averaging the uncertainties of 1000 random DWP realizations. More specifically, the phases are uniformly generated between 0 and 2π for all the parameters, whereas the amplitudes are obtained by perturbing the DWP2-3 values with 0.2 dB deviation for the imbalances and 2 dB deviation for the CTs. The sensitivity problem at $\pm\pi$ is evident in the trend of all the parameters. Calibration in such conditions can be handled, as advised in the case of DWP3 by Table 2.6, only through the aid of a calibrated point target. The sensitivity to Faraday rotation is next evaluated by similarly perturbing amplitudes and phases around DWP2 (the imbalances phases are not moved though) and averaging the uncertainty realizations: the performance is reported in Fig. 2.7. A calibration criticality is found at $\pm k\pi/2$ and once again, according to Table 2.6, the correct calibration strategy should demand the employment of a CR.

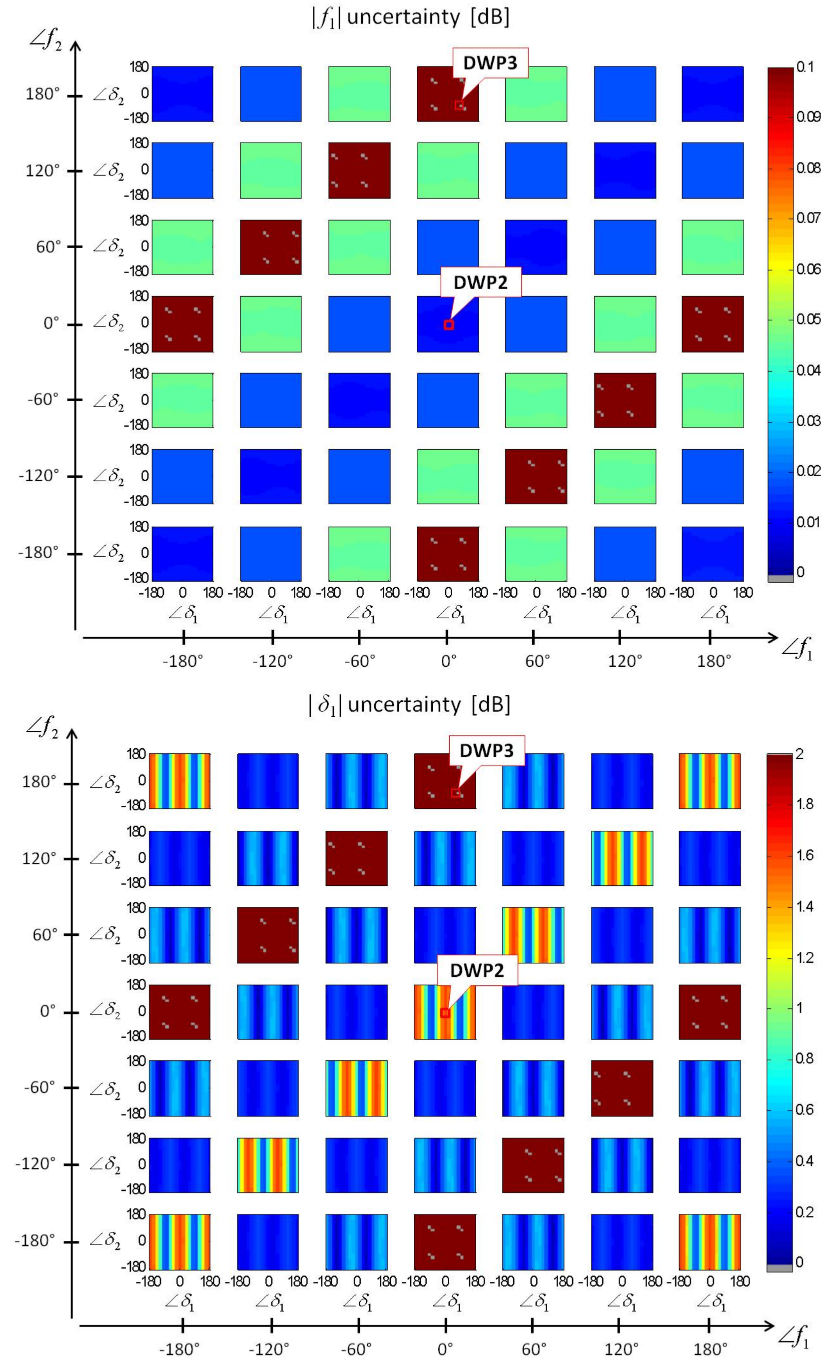

Figure 2.5: *Uncertainty on the f_1 (left) and δ_1 (right) amplitude as a function of the phase of the other parameters. DWP settings: $|f_1| = |f_2| = 0$ dB, $|\delta_1| = -30$ dB, $|\delta_2| = -26$ dB. FRA is set to 10°. The gray areas (e.g. DWP3) point to the ill-posed PDMs, whereas the saturated (red) areas represent the poor accuracy PDMs.*

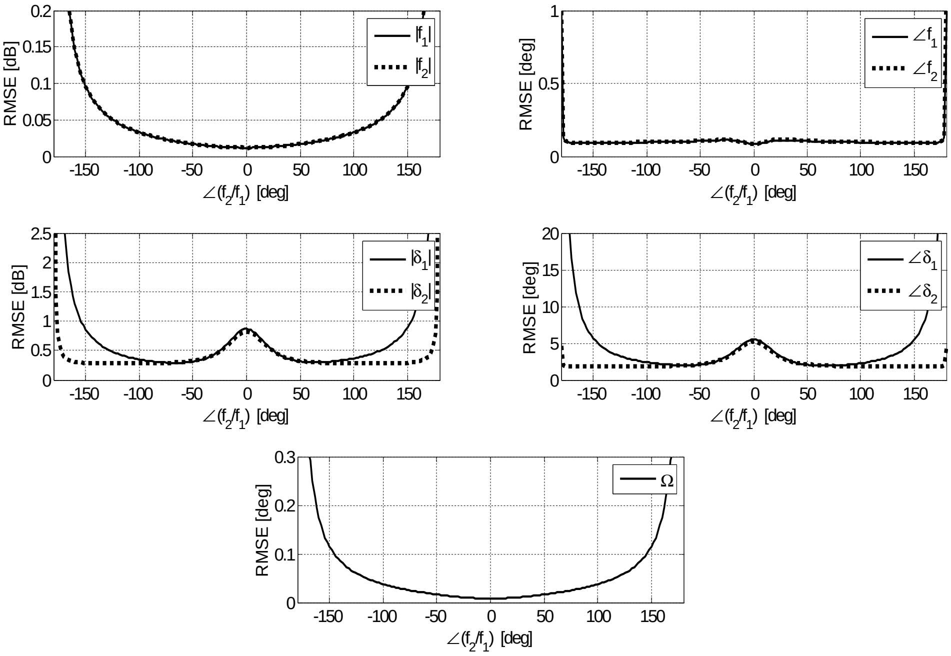

Figure 2.6: *Uncertainty behavior with respect to the imbalance ratio phase in a CT reciprocal configuration evaluated on* $\Omega = 10^{\circ}$ *FRA and* 10^5 *DT looks.*

The impact of the number of looks and of the model non-idealities on the sensitivity is now assessed by injecting into the model covariance (2.22) the disturbance $\mathbf{C_{ni}}$:

$$\mathbf{C_{ni}} = \begin{bmatrix} 0 & \varepsilon^*_{hh,hv}\sqrt{\sigma_{hh}\sigma_{hv}} & \varepsilon^*_{hh,hv}\sqrt{\sigma_{hh}\sigma_{hv}} & 0 \\ \varepsilon_{hh,hv}\sqrt{\sigma_{hh}\sigma_{hv}} & 0 & 0 & \varepsilon^*_{hv,vv}\sqrt{\sigma_{vv}\sigma_{hv}} \\ \varepsilon_{hh,hv}\sqrt{\sigma_{hh}\sigma_{hv}} & 0 & 0 & \varepsilon^*_{hv,vv}\sqrt{\sigma_{vv}\sigma_{hv}} \\ 0 & \varepsilon_{hv,vv}\sqrt{\sigma_{vv}\sigma_{hv}} & \varepsilon_{hv,vv}\sqrt{\sigma_{vv}\sigma_{hv}} & 0 \end{bmatrix} \tag{2.50}$$

yielding the perturbed model:

$$\mathbf{C_{Sp}} = \mathbf{C_S} + \mathbf{C_{ni}} \tag{2.51}$$

where $\mathbf{C_n} = \mathbf{H}\mathbf{C_{ni}}\mathbf{H}^H$ and ε plays the role of a normalized coherence. When $\varepsilon_{p,q}$ is varied in amplitude between 0 and 0.1, the uncertainty shown in Fig. 2.8 is registered. It can be noticed that when the deviation ε is close to 0 the sensitivity behavior is dominated by the number of looks N_p, whereas it becomes the most significant uncertainty source

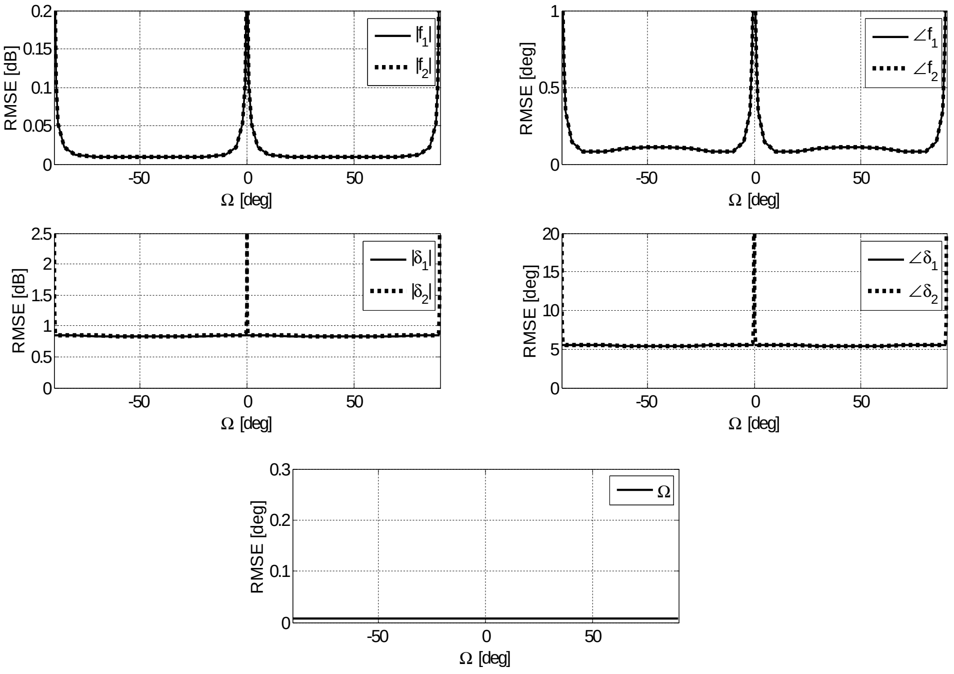

Figure 2.7: *Uncertainty in a CT reciprocal configuration evaluated on the whole FRA range (Ω behavior has π periodicity) and for* 10^5 *DT looks.*

for higher coherence deviation values. Each parameter has a different robustness to ε, i.e. a different growth slope with respect to the $|\varepsilon|$ units (reported in the panels alongside the curves), with the imbalances phase and the FRA being the most robust parameters, and the CTs being clearly the most degraded. The dual analysis on the N_p impact is then provided in Fig. 2.9 for the representative $\varepsilon = \{0, 0.01, 0.05\}$ set. The panels confirm the considerations already expressed about Fig. 2.8, with the $\angle f_1$ and Ω having the lower plateaus as expected. The log-linear trend was also predictable from the equations derived in appendix A, where it is evident that in absence of ε all the parameters behave as $\Delta_i \propto N_p^{-0.5}$.

2.3.4.2 Full system calibration aided by a point target

A full polarimetric system calibration cannot be attained when FRA is not negligible and accurate radiometric information are not available. The outcome is different when Faraday is not interfering, though the scenario (see Table 2.6) demands the employment of a CR. The uncertainty is investigated by (2.32) and (2.46), where the joint DT-CR presence is

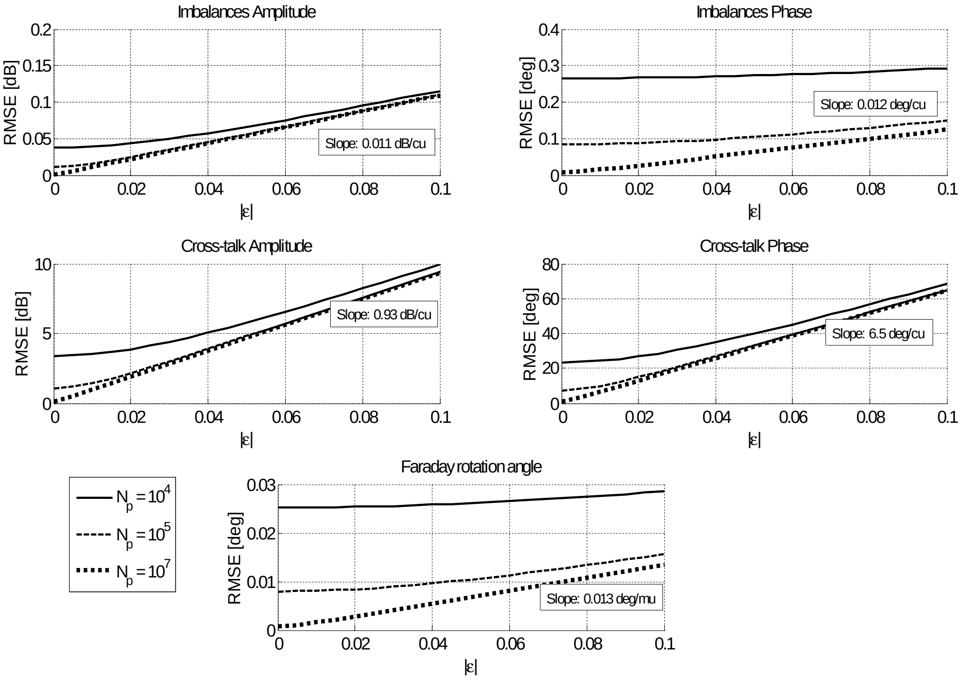

Figure 2.8: *Uncertainty in a CT reciprocal configuration with respect to the model deviation from the azimuthal symmetry assumption. The assessment is carried out in the neighborhood of DWP2 and a* $\Omega = 10^\circ$ *FRA for three different* N_p *settings.*

dealt through (2.45). As opposed to the calibration scenario in the previous section, the presence of a CR prevents from the occurrence of critical PDM configurations. Besides the DT factors already discussed, the calibration performance is obviously determined by the CR quality. This latter is represented by the clutter strength superimposed to the point target impulse response and by the APN, i.e. deviations from the ideal signature (2.23), modeled with:

$$\mathbf{N_{APN}} = \sqrt{\sigma_{CR}} \begin{bmatrix} \epsilon_{11} & \epsilon_{12} \\ \epsilon_{12} & \epsilon_{22} \end{bmatrix} \tag{2.52}$$

with ϵ_{ij} depending on the entity of the manufacturing and orientation inaccuracies. The clutter has been simulated in accordance with the typical flat ground scatterer whose details are provided in Table 2.7. The uncertainty is assessed by injecting into the measures APN disturbances, ϵ_{ij}, with the desired amplitude and uniformly distributed random phases. The CR quality with regard to the SCR is regulated by acting on the target reflectivity σ_{CR}. Assuming that a predetermined number of $N_p = 10^6$ looks is used for the DT and

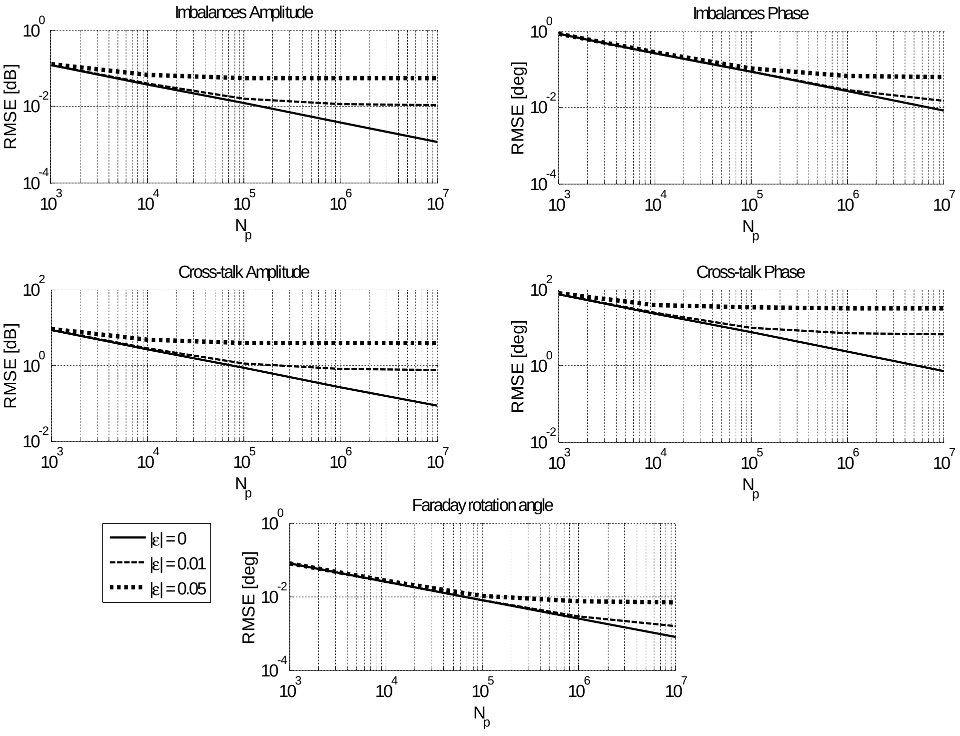

Figure 2.9: *Uncertainty in a CT reciprocal configuration with respect to the the number of looks N_p. The assessment is carried out in a neighborhood of DWP2 and on a $\Omega = 10^\circ$ FRA for three different coherence deviation, ε, settings.*

that this latter is ideal (ε null), a first analysis on the joint impact of the APN and SCR level on the calibration quality is shown in Fig. 2.10. Though the nature of the SCR and of the APN is different, their influence on the model model uncertainty is similar, with just little more sensitivity registered for the APN. On the quantitative standpoint it should be noticed that when the SCR is higher than 30 dB and the APN stands below -35 dB, the joint PT+DT uncertainty complies with the performance requirements in Table 2.2. Fixing then the CR quality to a 35 dB SCR, the two model deviations ε and APN are explored in Fig. 2.11. The imbalances uncertainty is more sensitive to the APN, whereas the CT model is more sensitive to the DT deviations. It is worth remarking that when the point target is employed for imbalance retrieval a PT quality (APN) better than -30 dB is demanded to comply with a 0.15-0.2 dB accuracy. This is indeed the case of a few well-acknowledged approaches [42,49] that employ a CR for attaining absolute imbalance information, resorting to the DT for the retrieval of all the other parameters.

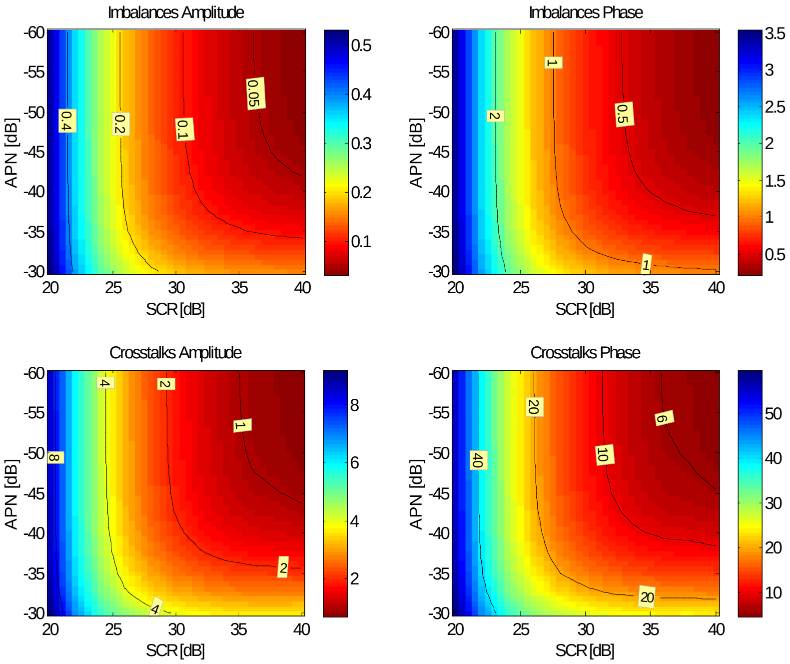

Figure 2.10: *Uncertainty behavior with respect to CR quality (APN and SCR parameters) in a CT generic and FRA null scenario. The DT quality has been set to* $\varepsilon = 0$ *and* $N_p = 10^6$.

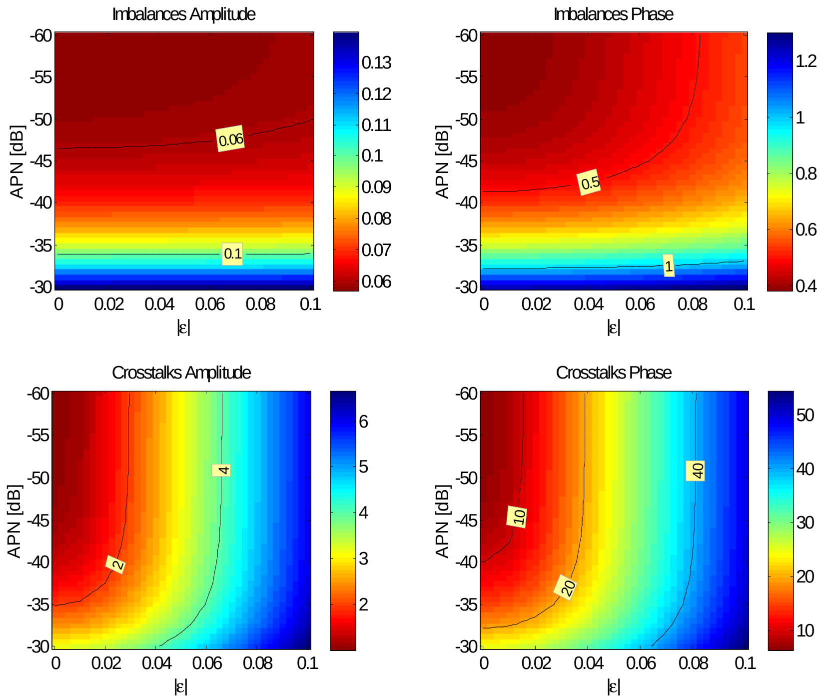

Figure 2.11: *Uncertainty behavior with respect to both the CR and DT quality (APN and DT deviation ε, this latter represented in linear scale) in a CT generic and FRA null scenario. The corner SCR is set to 35 dB and the DT looks are $N_p = 10^6$.*

2.4 A feasible approach for partial PDM estimation

According to Table 2.5 the use of a CR is required in all the addressed model scenarios with the exception of those configurations where some assumption on the CT is done (CT null or reciprocal) and a non-null FRA is affecting the scene. It was also discussed in 2.3.3 how a full model estimation is indeed unfeasible without any a-priori constraint on some of the involved parameters (e.g. the radiometric gain). However it will be shown that, through proper model arrangement, some of its parameters can be nonetheless determined independently from the others. With concern to a null FRA environment, the solution proposed by Quegan in [38] provides an effective answer to this point, showing that at least the quantities:

$$\alpha = f_1/f_2, \quad \delta_1' = \delta_1, \quad \delta_3' = \delta_3, \quad \delta_2' = \delta_2/f_1, \quad \delta_4' = \delta_4/f_2 \tag{2.53}$$

can be unambiguously retrieved. Notice that the set includes all the PDM parameters with the exception of one imbalance. The Quegan algorithm is based on the same DT assumption (reciprocity and azimuthal symmetry) used in our previous analysis and yields closed-form expressions for the estimators of (2.53). Their derivation is aided by further approximating the second order CT terms in the distorted covariance to 0, implying that cross-talk parameters must have much smaller amplitudes than true-like parameters. More details about the algorithm implementation is provided in appendix B.

The sensitivity with respect to the set (2.53) is then formally investigated through the approach discussed in 2.3. The model (2.15) is rephrased into:

$$\mathbf{M} = A \cdot e^{j\phi} \begin{bmatrix} 1 & \delta_2/f_1 \\ \delta_1 & 1 \end{bmatrix} \cdot \begin{bmatrix} 1 & 0 \\ 0 & f_1/f_2 \end{bmatrix} \begin{bmatrix} 1 & 0 \\ 0 & f_2 \end{bmatrix} \cdot \mathbf{S} \cdot \begin{bmatrix} 1 & 0 \\ 0 & f_2 \end{bmatrix} \cdot \begin{bmatrix} 1 & \delta_3 \\ \delta_4/f_2 & 1 \end{bmatrix} + \mathbf{N} \tag{2.54}$$

or, in its vectorized form:

$$\mathbf{m} = A \cdot e^{j\phi} \cdot \mathbf{Q} \cdot \mathbf{F} \cdot \mathbf{s} + \mathbf{n} \tag{2.55}$$

with:

$$\mathbf{Q} = \begin{bmatrix} 1 & \delta'_2 & \delta'_4 & \delta'_2\delta'_4 \\ \delta'_1 & 1 & \delta'_1\delta'_4 & \delta'_4 \\ \delta'_3 & \delta'_2\delta'_3 & 1 & \delta'_2 \\ \delta'_1\delta'_3 & \delta'_3 & \delta'_1 & 1 \end{bmatrix} \cdot \begin{bmatrix} 1 & & \cdots & 0 \\ & \alpha & & \vdots \\ \vdots & & 1 & \\ 0 & \cdots & & \alpha \end{bmatrix} \tag{2.56}$$

$$\mathbf{F} = \begin{bmatrix} 1 & & \cdots & 0 \\ & f_2 & & \vdots \\ \vdots & & f_2 & \\ 0 & \cdots & & f_2^2 \end{bmatrix} \tag{2.57}$$

where Faraday effects are not accounted for. By applying the distortion (2.55) in (2.21), it is readily verified that:

$$\mathbf{C} = A^2\mathbf{Q} \cdot \mathbf{F} \cdot \mathbf{C_S} \cdot \mathbf{F}^H \cdot \mathbf{Q}^H = A^2\mathbf{Q} \cdot \mathbf{C_Q} \cdot \mathbf{Q}^H \tag{2.58}$$

$$\mathbf{C_Q} = \begin{bmatrix} \sigma'_{hh} & 0 & 0 & \rho'^* \\ 0 & \sigma'_{hv} & \sigma'_{hv} & 0 \\ 0 & \sigma'_{hv} & \sigma'_{hv} & 0 \\ \rho' & 0 & 0 & \sigma'_{vv} \end{bmatrix} = \begin{bmatrix} \sigma_{hh} & 0 & 0 & (f_2^2\rho)^* \\ 0 & |f_2|^2\sigma_{hv} & |f_2|^2\sigma_{hv} & 0 \\ 0 & |f_2|^2\sigma_{hv} & |f_2|^2\sigma_{hv} & 0 \\ f_2^2\rho & 0 & 0 & |f_2|^4\sigma_{vv} \end{bmatrix}. \tag{2.59}$$

As a result in a DT calibration scenario the complexity would be equivalent to that of estimating the full δ,f model aided by the assumption $f_2 = 1$. It is straightforward noticing that (2.59) is replacing (2.22) and that the scattering reciprocity is not lost in the model. The SAR calibrated observables, achieved through the simple inversion:

$$\mathbf{m}_{cal} = \mathbf{Q}^{-1} \cdot \mathbf{m}, \tag{2.60}$$

are determined up to a f_2 and f_2^2 factor respectively in the HV and VV channels . The approach feasibility analysis, reported in Table 2.8 , confirms that such parameter simplification is able to deal with all the aforementioned PDM criticalities.

Table 2.8: *Feasibility analysis for the shrinked model approach*

Model		Parameters	DT Calibration			
			DWP1	DWP2	DWP3	DWP4
FRA: $\Omega = 0$	CT null FRA null	- f_1/f_2 - σ'_{hh}, σ'_{hv}, σ'_{vv},ρ'	YES	YES	YES	YES
	CT reciprocal FRA null	- f_1/f_2, δ'_1, δ'_2 - σ'_{hh}, σ'_{hv}, σ'_{vv},ρ'	YES	YES	YES	YES
	CT unknown FRA null	- f_1/f_2, δ'_1, δ'_2, δ'_3, δ'_4 - σ'_{hh}, σ'_{hv}, σ'_{vv},ρ'	YES	YES	YES	YES

Note: the table provides information on whether the calibration problem is well-posed (YES), ill-posed (NO) or the model is not consistent with the DWP (-)

The performance achievable by the Quegan algorithm with respect to the most significant DT features is investigated through MC simulations. The sensitivity of the corresponding model (2.55), computed through (2.32), is also reported in order to provide a more insightful analysis. In section 2.3.4 it was remarked how the accuracy is predictably dependent on the number of averaged DT looks, but also on deviations from the hypothesized model. It was shown in Fig. 2.9 that when the number of looks is high enough, as a rule of thumb $N_p \geq 10^5$, the estimation error in the most sensitive parameters, i.e. the CTs, is governed by the model non-idealities. The theoretical results achieved by the technique are illustrated in the panels in Fig. 2.12 where the impact of small covariance deviations is also addressed. The performance has been studied for a realistic CT set of values ranging from -45 dB to -25 dB, and for two different natural scatterers: a forest and a bare soil. The forest has indeed a stronger HV channel and a lower HH,VV correlation than the bare soil, whose behavior is more similar to an ideal Bragg scatterer (quantitative details of both mechanisms are taken from Table 2.7). Such scattering difference has indeed an effect on the calibration performance, with the forest being more accurate for imbalance ratio estimation and the ground having a slight advantage on the CTs due to the higher σ_{hh}/σ_{hv}, σ_{vv}/σ_{hv} ratios. Whereas it is evident that the estimation error on the imbalance ratio is never a problem, registering RMSE below 0.05 dB and 1° in amplitude and phase respectively, the CT performance can be critical. The dominant factor in the CT behavior are indeed the CT amplitude itself and the model perturbation entity. The phase accuracy in particular, even without model disturbances, is on average worse than 15°.

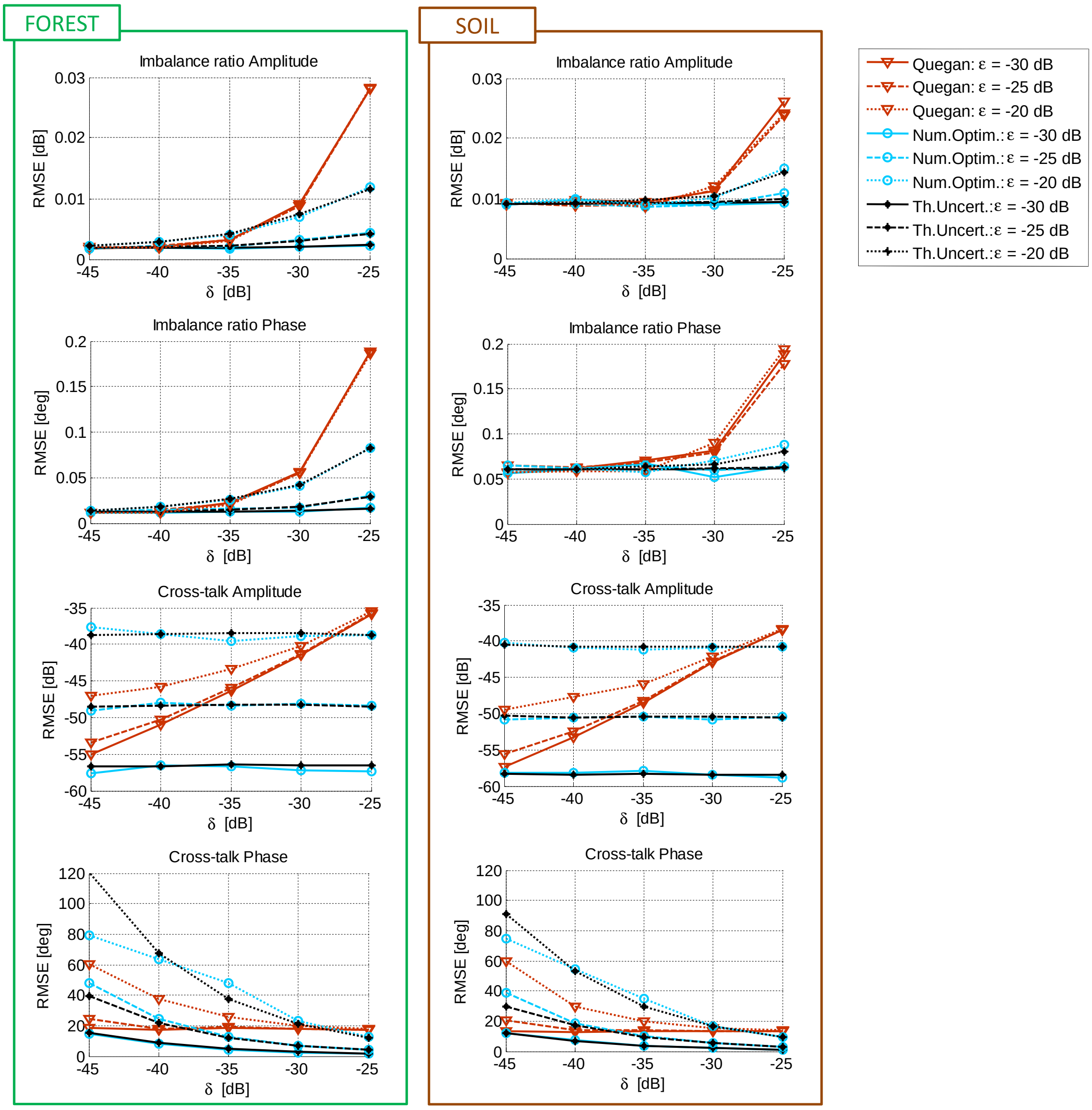

Figure 2.12: *Shrinked model approach: calibration performance measured for 3 values of the disturbance ε in the covariance model as a function of the CT level. The accuracy achieved by the traditional Quegan technique (red), by the numerical optimizator (cyan) and the uncertainty attained through theoretical sensitivity analysis (black) are reported for a typical forest and ground DTs with size $N_p = 10^6$. Note that the RMSE on the imbalances amplitude refers to the dB (relative amplitude) displacement whereas in the CT case it refers to the absolute magnitude error (linear scale).*

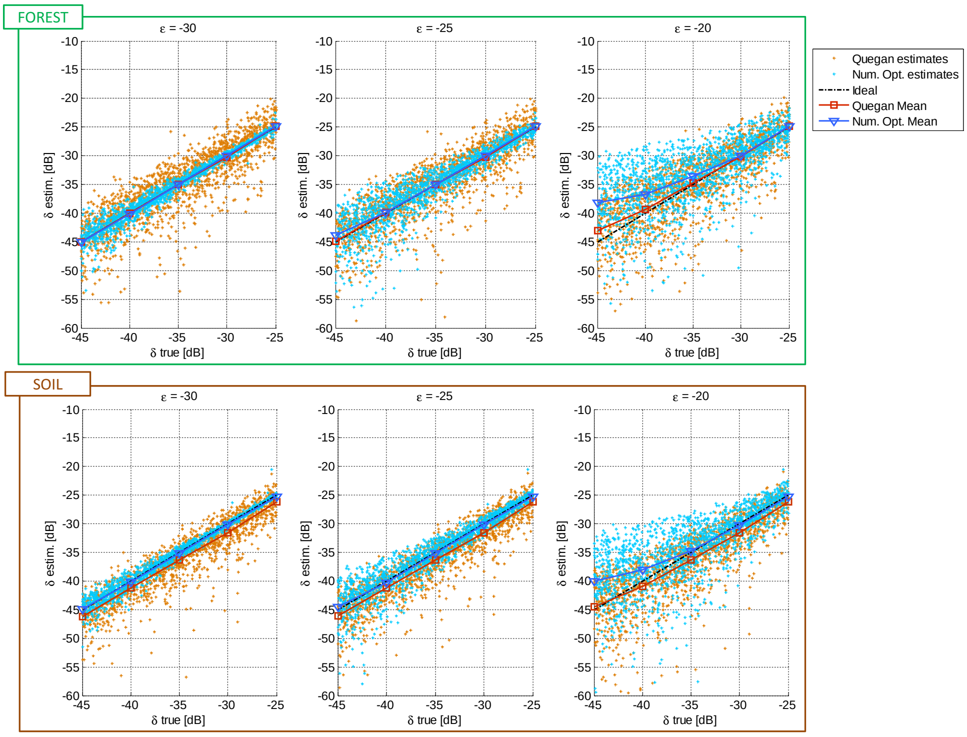

Figure 2.13: *Shrinked model approach: retrieved CT amplitudes compared to the real values for three different strength of the model perturbation ε. The simulation has been carried out for both the Quegan algorithm (red) and the numerical optimizator (cyan) on a forest DT model (10^6 looks).*

Another interesting point from Fig. 2.12 is provided by the comparison with the theoretical uncertainty. Whereas the quality of Quegan estimates is hindered by CT amplitudes, the theoretical sensitivity analysis shows that the performance is dependent only on the Cpol-Xpol coherence deviations ε. The results convey that in the presence of strong CTs the estimates have margin for improvement. Such margins can be indeed filled by refining the calibration procedure through the numerical optimization discussed in section 2.5. It is straightforward noticing how the accuracy achieved, shown in the same Fig. 2.12 panels, is consistent with the theoretical prediction, meaning that the workpoint initialization provided by the Quegan estimates represents indeed an effective choice (even when high CTs are involved) for the algorithm correct convergence. Notice though that the Quegan technique still represents the best option when the ratio between the CTs and the model perturbation ε is low. Such trend is further remarked in Fig. 2.13, where the average bias of both techniques is also represented. In both the DT cases the numerical optimization is overestimating the CTs (significantly in the case of the forest with strong residual Cpol-Xpol coherence), whereas the Quegan algorithm is almost unbiased in the forest case but underestimates (with a bias of -1.5 dB) the CTs with the ground scattering.

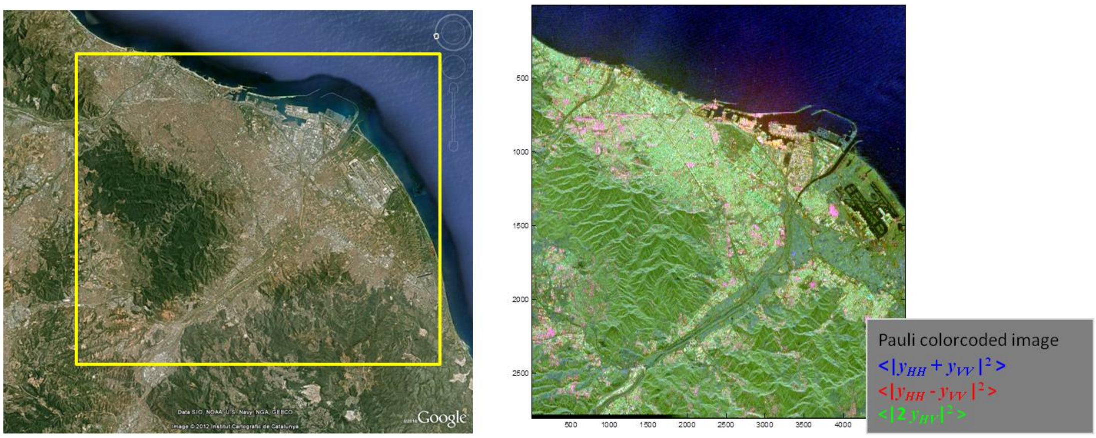

Figure 2.14: *(left) Optical reference of the Barcelona area. (right) Pauli color coded representation of the or the RS2 Fine-Quad Mode SLC used for analysis (slant-range,azimuth coordinates). The land typology diversity inside the frame clearly emerges from the two views.*

2.4.1 Application to RS2 data

The accuracy of the technique has been tested on the C-Band Radarsat-2 dataset collected over the Barcelona area with the Fine Quad-Pol mode, whose format is described in more detail in chapter 4 (section 4.3.1). The RS2 imagery is supposed to be accurately calibrated, as previous works [28] were able to assess, with CT level below -35 dB. A preliminary analysis has been conducted on spatial blocks of different sizes ranging from $N_p = 100$ to 10^5 looks. The aim is to point out how the real data diversity relate to the consistency of the calibration results. With the support of the Pauli color coded image and its optical reference in Fig. 2.14 for an intuitive association of each area to its typology, it is indeed possible to notice in Fig. 2.15 the dependence of the orientation symmetry on the block dimension N_p and on the scatterer characteristics. The degree of coherence between HH and HV (normalized for the channels power) is used as indicator. The DT-based techniques require indeed such value to be almost null, though the finite number of looks and the presence of polarized X-pol backscatter affect its estimate. The size of the block has a significant impact up to $N_p = 10^5$, as remarked in the theoretical analysis of section 2.3, then the model bias becomes dominant. The polarization induced on the estimated cross-talks is illustrated in histograms of Fig.2.16. An almost linear trend of the CT error with respect to $C_{HH,HV}$ can be inferred from the plotted distributions, validating the theoretical analysis in section 2.4 that demanded a maximum of -20 dB for Cpol-Xpol coherence deviation.

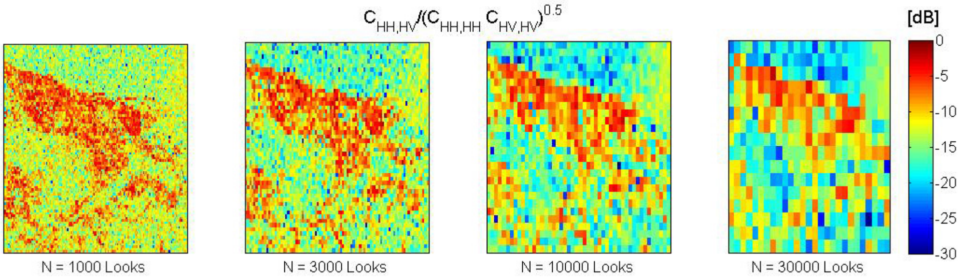

Figure 2.15: *Coherence between HH and HV channels for blocks of different dimension. The analysis provides quantitative evidence on the dependence of the reflection symmetry on the looks N_p used for ensemble average and on the scatterer characteristics.*

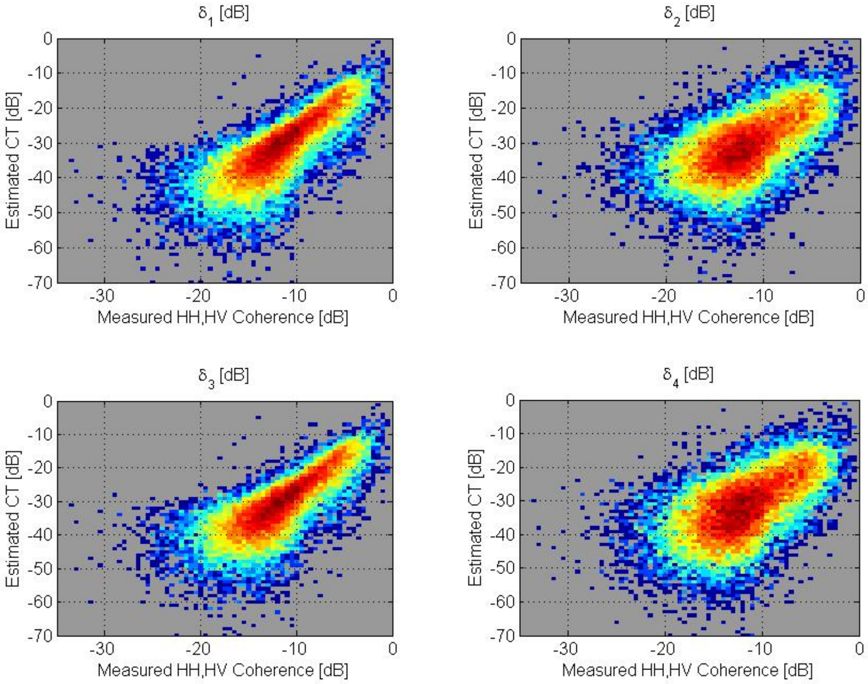

Figure 2.16: *Correlation in the RS2 data between non-ideal reflection symmetry (non-null HH,HV coherence) and its effects on the cross-talk estimation by means of the Quegan technique.*

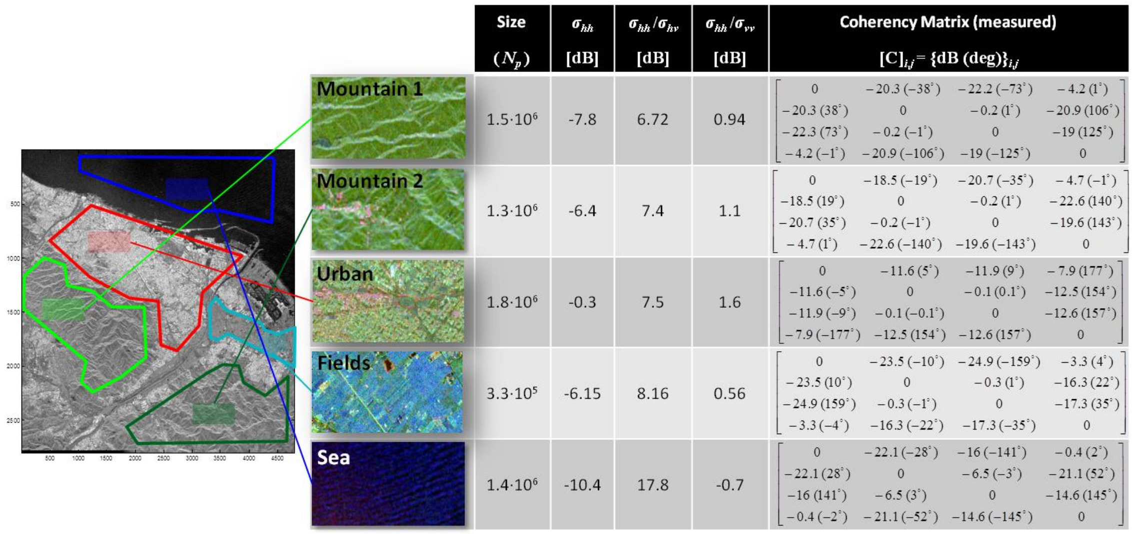

	Size (N_p)	σ_{hh} [dB]	σ_{hh}/σ_{hv} [dB]	σ_{hh}/σ_{vv} [dB]	Coherency Matrix (measured) $[C]_{i,j} = \{dB\ (deg)\}_{i,j}$
Mountain 1	$1.5\cdot10^6$	-7.8	6.72	0.94	$\begin{bmatrix} 0 & -20.3\,(-38^\circ) & -22.2\,(-73^\circ) & -4.2\,(1^\circ) \\ -20.3\,(38^\circ) & 0 & -0.2\,(1^\circ) & -20.9\,(106^\circ) \\ -22.3\,(73^\circ) & -0.2\,(-1^\circ) & 0 & -19\,(125^\circ) \\ -4.2\,(-1^\circ) & -20.9\,(-106^\circ) & -19\,(-125^\circ) & 0 \end{bmatrix}$
Mountain 2	$1.3\cdot10^6$	-6.4	7.4	1.1	$\begin{bmatrix} 0 & -18.5\,(-19^\circ) & -20.7\,(-35^\circ) & -4.7\,(-1^\circ) \\ -18.5\,(19^\circ) & 0 & -0.2\,(1^\circ) & -22.6\,(140^\circ) \\ -20.7\,(35^\circ) & -0.2\,(-1^\circ) & 0 & -19.6\,(143^\circ) \\ -4.7\,(1^\circ) & -22.6\,(-140^\circ) & -19.6\,(-143^\circ) & 0 \end{bmatrix}$
Urban	$1.8\cdot10^6$	-0.3	7.5	1.6	$\begin{bmatrix} 0 & -11.6\,(5^\circ) & -11.9\,(9^\circ) & -7.9\,(177^\circ) \\ -11.6\,(-5^\circ) & 0 & -0.1\,(0.1^\circ) & -12.5\,(154^\circ) \\ -11.9\,(-9^\circ) & -0.1\,(-0.1^\circ) & 0 & -12.6\,(157^\circ) \\ -7.9\,(-177^\circ) & -12.5\,(154^\circ) & -12.6\,(157^\circ) & 0 \end{bmatrix}$
Fields	$3.3\cdot10^5$	-6.15	8.16	0.56	$\begin{bmatrix} 0 & -23.5\,(-10^\circ) & -24.9\,(-159^\circ) & -3.3\,(4^\circ) \\ -23.5\,(10^\circ) & 0 & -0.3\,(1^\circ) & -16.3\,(22^\circ) \\ -24.9\,(159^\circ) & -0.3\,(-1^\circ) & 0 & -17.3\,(35^\circ) \\ -3.3\,(-4^\circ) & -16.3\,(-22^\circ) & -17.3\,(-35^\circ) & 0 \end{bmatrix}$
Sea	$1.4\cdot10^6$	-10.4	17.8	-0.7	$\begin{bmatrix} 0 & -22.1\,(-28^\circ) & -16\,(-141^\circ) & -0.4\,(2^\circ) \\ -22.1\,(28^\circ) & 0 & -6.5\,(-3^\circ) & -21.1\,(52^\circ) \\ -16\,(141^\circ) & -6.5\,(3^\circ) & 0 & -14.6\,(145^\circ) \\ -0.4\,(-2^\circ) & -21.1\,(-52^\circ) & -14.6\,(-145^\circ) & 0 \end{bmatrix}$

Figure 2.17: *Details of the scattering areas selected for calibration analysis. The table reports the DT size, the average channel intensities and the polarimetric coherence measured for the 13-JUN-2011 image (see 4.2).*

A better conceived analysis has been conducted by isolating 5 different DT areas (through hand-made segmentation), corresponding to representative classes of scatterers, i.e.:

1. a sloped vegetated terrain behind the Barcellona town
2. a second vegetated area
3. the inhabited Barcellona area itself
4. a flat cultivated area
5. the sea surface

whose backscatter characteristics are reported in Fig. 2.17 for one of the images. The vegetated areas are the closest to the reflection symmetry requirements, whereas the inhabited terrain exhibits cross-polarized backscatter which results in higher HH,HV coherence. The sea, in the end, has been included in the analysis, though it can be easily predicted that its very low HV intensity, almost comparable with the system noise, will hinder the resulting estimates. It must be remembered that the assumption of orientation symmetry for distributed scatterers should hold robustly for C-Band data [26]. Differently, L- and P-band signal would undermined by the presence of sloped areas that introduce preferred orientation directions, and therefore demand large ensemble averaging in order to filter out from the covariance the topography effects [20, 26]. The result of the calibration performed on the 5 areas has been reported in Table 2.9. The inhabited and the sea areas have very poor performance, the first clearly overestimating the CTs and the latter showing serious problems with the imbalance ratio. The vegetated areas (fields and forest) are indeed the most suited one, returning CT levels ranging from -50 to -35 and imbalance stability in the order of 0.1 dB, thus consistent with the RS2 radiometric stability and channel isolation. It must be remarked that for finely calibrated systems, the CT estimates are mostly determined by the model non-idealities. This consideration is indeed supported by the theoretical results in Fig. 2.12, where it is shown that for CTs as low as -45 dB the error done is almost in the same magnitude order of the CT. The analysis should be nonetheless deemed meaningful since it can to provide effective evidence of the system good health.

Table 2.9: *Results attained by the Quegan calibration algorithm. For each calibration configuration the mean value and its standard deviation (into brackets) of the amplitude and phase estimates throughout the RS2 dataset is reported. The format is indeed: Ampl. Mean [dB] (Ampl. Std [dB]), Phase Mean [deg] (Phase Std. [deg]).*

	f_1/f_2	δ_1	δ'_2	δ_3	δ'_4
Mountain 1	-0.086 (-49.6), 0.10 (1.6)	-53.2 (-61.5), -8.7 (43.8)	-49.1 (-56.7), 162.9 (18.8)	-55.4 (-62.4), -128.8 (66.6)	-53.6 (-60.5), -133.8 (67,3)
Mountain 2	-0.078 (-46.9), -0.04 (1.6)	-49.7 (-56.4), 7.62 (26.2)	-43.0 (-55.7), 169.2 (9.1)	-54.6 (-58.3), -119.9 (90.2)	-45.9 (-55.4), -175.6 (14.0)
Urban	-0.080 (-50.9), 0.15 (1.6)	-31.5 (-51.2), -4.6 (5.3)	-32.2 (-49.4), -166.3 (9.4)	-32.2 (-50.2), -8.2 (6.3)	-32.3 (-49.5), -163.5 (10.5)
Fields	-0.082 (-49.4), 0.02 (1.6)	-40.3 (-53.5), 167.3 (10.4)	-38.1 (-50.7), 27.5 (10.6)	-38.5 (-51.8), 175.5 (11.1)	-37.2 (-50.0), 16.6 (10.6)
Sea	-0.354 (-26.2), -1.8 (2.4)	-27.5 (-30.5), -10.8 (87.4)	-28.2 (-31.6), 166.3 (62.0)	-27.6 (-31.1), -4.1 (74.7)	-28.5 (-31.3), 149.2 (82.7)

* In the reduced model exploited by the Quegan approach δ_2 and δ_4 are indeed replaced by $\delta'_2 = \delta_2/f_1$ and $\delta'_4 = \delta_4/f_2$.

2.4.2 L-Band calibration with non-null Faraday rotations

It was discussed in 2.3.2 and 2.3.4.1 how the presence of Faraday rotations in a CT reciprocal system makes the calibration optimization problem well-determined, even with just a DT. The scenario has been cleverly approached by Freeman in [19], where it was shown that closed-form estimators for f_1, f_2, δ_1, δ_2, Ω can be obtained through the Faraday linearization

$$\sin\Omega \simeq \Omega, \qquad \cos\Omega \simeq 1 \tag{2.61}$$

valid for small FRA. The system (2.15), under the assumption of reciprocal CTs, becomes then:

$$\mathbf{M} = A \cdot e^{j\phi} \begin{bmatrix} 1 & \delta_2 \\ \delta_1 & f_1 \end{bmatrix} \begin{bmatrix} 1 & \Omega \\ -\Omega & 1 \end{bmatrix} \cdot \mathbf{S} \cdot \begin{bmatrix} 1 & \Omega \\ -\Omega & 1 \end{bmatrix} \begin{bmatrix} 1 & \delta_1 \\ \delta_2 & f_2 \end{bmatrix} + \mathbf{N}. \tag{2.62}$$

By omitting the cross-products $\delta_i \Omega$, it can be further simplified into:

$$\mathbf{M} = A \cdot e^{j\phi} \begin{bmatrix} 1 & \delta_2 + \Omega \\ \delta_1 - \Omega f_1 & f_1 \end{bmatrix} \cdot \mathbf{S} \cdot \begin{bmatrix} 1 & \delta_1 + \Omega f_2 \\ \delta_2 - \Omega & f_2 \end{bmatrix} + \mathbf{N}. \tag{2.63}$$

The Quegan method is then exploited to yield:

$$\begin{aligned} &\alpha = f_1/f_2 \\ &u = \delta_1 - \Omega f_1 \quad z = \delta_1 + \Omega f_2 \\ &w = \frac{\delta_2 + \Omega}{f_1} \quad\; v = \frac{\delta_2 - \Omega}{f_2} \end{aligned} \tag{2.64}$$

that can be solved in closed-form (see section B.2 in appendix) with the exception of a sign ambiguity, which, however, is easily determined by means of a-priori information on the imbalances or on some convenient scene features (e.g. the HV/HH phase for some known natural point target). It must be stressed that such approach benefits from high channels isolation, and more specifically when both the FRA, see (2.61), and its combination with the CTs, in favor of higher accuracy in the Quegan estimates (2.64), are low. The performance is evaluated on synthetic datasets and is shown in Fig. 2.19 to Fig. 2.21, where its error estimates are also compared with those of other methods. A discussion on such results is provided at the end of the next section.

2.5 Numerical optimization of the PDM estimates

The closed-form solutions discussed in 2.4 and 2.4.2 for two typical DT calibration scenarios are convenient because their implementation is effortless and their behavior is predictable. It is also straightforward that their performance is limited by the approximations adopted. The analysis in 2.3 provided useful information on the possibility of carrying out numerical optimization on the cases examined. When the problem is indeed well-determined and the a-priori PDM information is close enough to the optimum, a numerical derivation represents a valid option.

With reference to a DT-only calibration the number of real equations is 16 against 15 unknowns in the case of the shrinked model in 2.4 or 14 in the scenario of Fig. 2.3 and 2.4.2. An additional unknown has to be counted when the NESZ contribute is accounted for in the optimization: its introduction does not undermine in either case the problem solvability. The amount of parameters is then far from being prohibitive, and the computational times are certainly affordable (in the order of a few seconds). A generic solution scheme is illustrated in Fig. 2.18. The additional aid of point targets is included in the

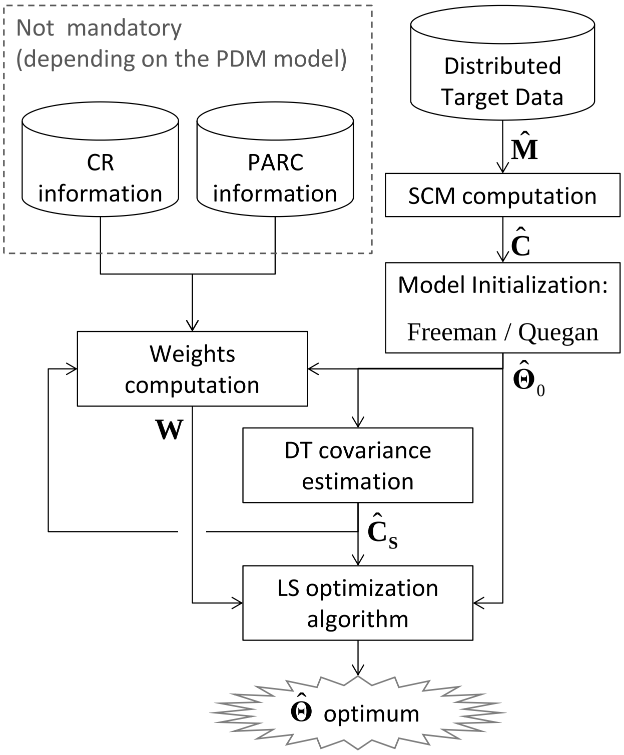

Figure 2.18: *Scheme of the calibration optimization procedure.*

scheme since it can be seamlessly integrated in the procedure through proper equation weighting, though the present work has been committed to the correct handling of the DT-only scenario.

The first step is the derivation from the estimated covariance $\mathbf{C}$ of the starting DWP parameters $\boldsymbol{\Theta}_0$ through one of the available techniques. The resulting PDM, $\mathbf{H}_0 = \mathbf{H}(\hat{\boldsymbol{\Theta}}_0)$, together with the eventual estimate of the sigma nought σ_n (e.g. the Quegan approach provides such estimate for the X-pol channels), are then used to determine the model covariance:

$$\mathbf{C}_{inv} = \mathbf{H}_{\mathbf{3}0}^{\dagger}\left(\mathbf{C} - \sigma_n \mathbf{I}\right)\left(\mathbf{H}_{\mathbf{3}0}^{H}\right)^{\dagger} \tag{2.65}$$

$$\mathbf{H}_{\mathbf{3}0} = \mathbf{H}_0 \cdot \mathbf{D} = \mathbf{H}_0 \cdot \begin{bmatrix} 1 & 0 & 0 \\ 0 & 1 & 0 \\ 0 & 1 & 0 \\ 0 & 0 & 1 \end{bmatrix} \tag{2.66}$$

where † refers to the matrix pseudo-inverse operation and $\hat{\mathbf{C}}_{inv}$ is a 3 by 3 matrix that do not respect in general the reflection symmetry assumption. This latter condition is therefore obtained by roughly nulling the Cpol-Xpol covariance elements through:

$$\hat{\mathbf{C}}_{\mathbf{S}} = \mathbf{C}_{inv} \circ \begin{bmatrix} 1 & 0 & 1 \\ 0 & 1 & 0 \\ 1 & 0 & 1 \end{bmatrix} \tag{2.67}$$

where $\circ$ stands for the matrix point-wise (Hadamard) product. As next operation, the predicted data covariance is calculated by means of the direct model:

$$\hat{\mathbf{C}}_0 = \mathbf{H_{30}} \cdot \hat{\mathbf{C}}_{\mathbf{S}} \cdot \mathbf{H}_{\mathbf{30}}^H + \sigma_n \mathbf{I} \tag{2.68}$$

and its measurement uncertainty

$$\mathbf{W} = E\left[\text{vec}(\hat{\mathbf{C}}_0^{mes} - \hat{\mathbf{C}}_0) \cdot \text{vec}(\hat{\mathbf{C}}_0^{mes} - \hat{\mathbf{C}}_0)^H\right]$$

is attained through expressions in appendix A. The proposed optimization algorithm accounts for the model sensitivity by adopting at each iteration the error metric:

$$e = \left\| \mathbf{W}^{-1/2} \cdot \text{vec}(\hat{\mathbf{C}} - \mathbf{C}) \right\| \tag{2.69}$$

i.e. by weighting the displacement between the reconstructed covariance $\hat{\mathbf{C}}$ and the measured one $\mathbf{C}$ with the data covariance $\mathbf{W}$. The new estimates are then readily obtained by moving towards the e minimum, i.e. in formula:

$$\hat{\Theta}_i, \hat{\mathbf{C}}_{\mathbf{S}i}, = \underset{\Theta, \mathbf{C}_{\mathbf{S}}}{\text{argmin}} \left\| \mathbf{W}^{-1/2} \cdot \text{vec}\left(\hat{\mathbf{C}}(\Theta, \mathbf{C}_{\mathbf{S}}) - \mathbf{C}\right) \right\| \tag{2.70}$$

$$\hat{\mathbf{C}}(\Theta, \mathbf{C}_{\mathbf{S}}) = \mathbf{H_3}(\Theta) \cdot \mathbf{C}_{\mathbf{S}} \cdot \mathbf{H_3}(\Theta)^H + \sigma_n \mathbf{I}$$

until a stable point is reached.

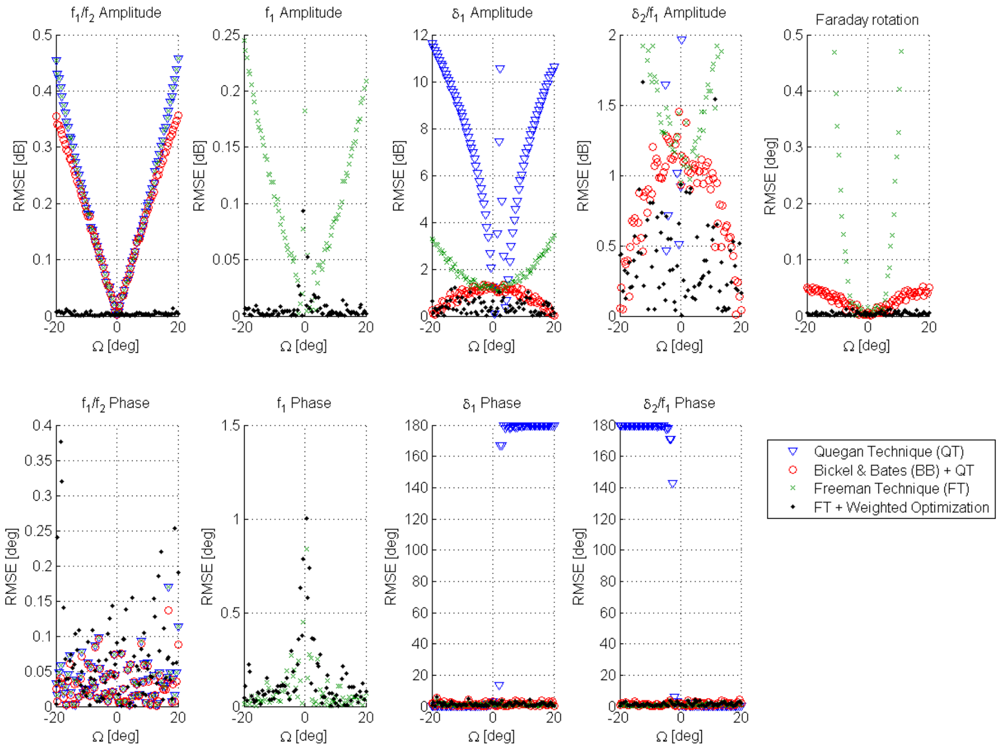

Figure 2.19: *Performance shoot-out on the PDM:* $f_1 = f_2 = 1$, $\delta_1 = \delta_2 = \delta_3 = \delta_4 = -30dB\angle 0°$. *The calibration is performed on* 10^5 *looks of a forest DT. The techniques compared are: the Quegan traditional approach (blue), the Quegan technique after Bickel&Bates Faraday removal (red), the Freeman technique (green) and the proposed optimization (black). Notice that some of the addressed parameters are not returned by all the approaches, i.e.* f_1 *is only estimated by the Freeman-based techniques and* Ω *is not considered in the QT.*

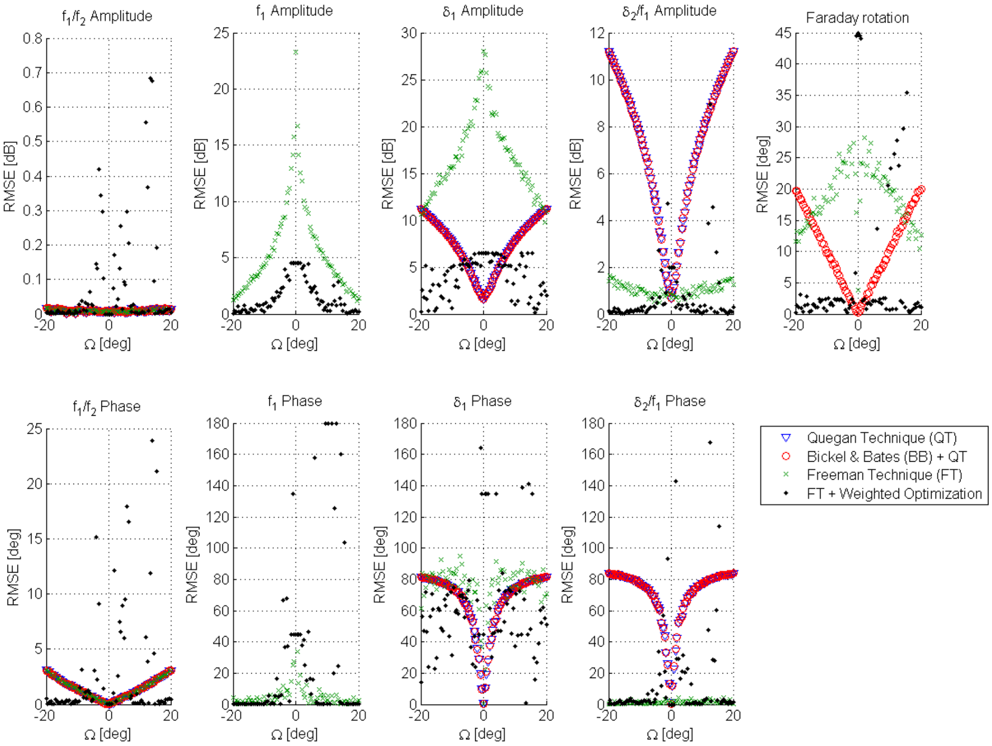

Figure 2.20: *Performance shoot-out on the PDM:* $f_1 = 1,\ f_2 = -1,\ \delta_1 = \delta_3 = -30dB\angle -90^\circ,\ \delta_2 = \delta_4 = -30dB\angle 90^\circ$*. The calibration is performed on* 10^5 *looks of a forest DT.*

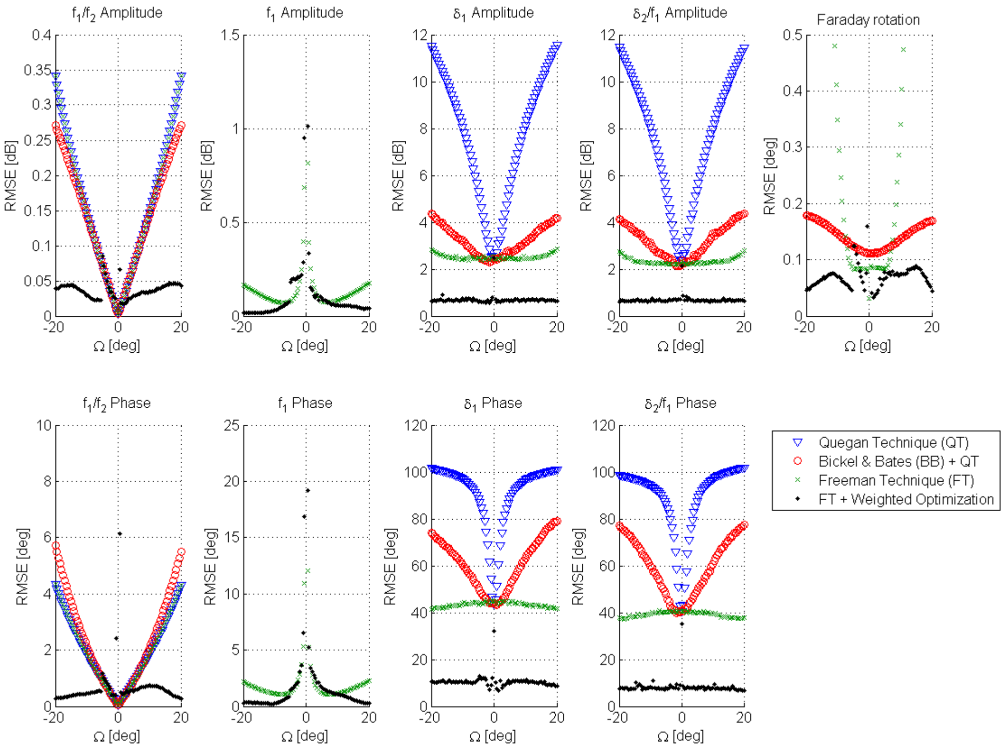

Figure 2.21: *Performance assessment based on MC simulation, i.e. by averaging 1000 PDM random realizations. The calibration is performed on* 10^5 *looks of a forest DT.*

The accuracy of the proposed method is compared, for different amounts of FRA disturbance, with that of other acknowledged techniques. The Quegan method discussed in 2.4 and the Freeman approach of 2.4.2 have been taken as reference. Since the former approach does cannot cope directly with the Faraday effects, a third approach that carries out a Faraday compensation before the application of the Quegan technique has been tested: the classic Bickel&Bates estimator [2] is used for the FRA evaluation. Note that such workflow is indeed inconsistent with the model, being the calibration steps applied in the inverse order (remember that Faraday is internal in the PDM). Nonetheless, it can be considered a valuable experiment for assessing the impact of the system miscalibration on the Faraday estimation and further demonstrating the degradation of the system parameters estimates due to improper Faraday handling. The techniques behavior is first tested on two particular distortion scenarios. The first is the same as DWP2 in Table 2.3, i.e. an easy scenario according to 2.3, whereas DWP3 has been chosen for the second case, a critical case indeed. The respective results, in Fig. 2.19 and Fig. 2.20, are in agreement with the theoretical expectations of a better performance for the first PDM, the only curious exception being the imbalance ratio amplitude RMSE. With concern to the proposed optimization, it can be noticed that the unstable behavior is limited to $\Omega = 0$ in the first scenario, whereas a wrong convergence can extend to other FRA values in the second scenario.

A more comprehensive assessment, on a quantitative standpoint, is then obtained through Montecarlo analysis and shown in Fig. 2.21. A total of 1000 PDMs are generated and their RMSE is hence averaged. The distortion diversity is simulated by perturbing the DWP2 parameters: the noise has been set to a gaussian distribution with 0.2 dB and 5 dB deviation for the imbalance and CT amplitudes, whereas their phases are uniformly generated into the $[-\pi/4,\ \pi/4]$ and $[-\pi,\ \pi]$ spans respectively. A few points are remarked with respect to the performance results:

- The proposed optimization scheme yields the best results, with the exception of the null FRA configuration, where the techniques based on the shrunk model in 2.4 represent the only feasible option. The CT estimates are in particular benefiting from the optimization, with accuracies laying below 1 dB.
- The accuracy achieved by traditional techniques on the imbalance ratio amplitude is acceptable (< 0.2 dB) up to a $\pm 10°$ FRA, while the CT performance is arguably poorer, even with null FRA, but probably sufficient to deliver the channel isolation demanded for the project.
- The FRA estimates attained by the Bickel&Bates technique are to be preferred over those computed by Freeman for FRA above $5°$, while they are both accurate for small FRA.

It can be concluded that a CT reciprocal L-band system can be calibrated with fulfilling accuracy in most of the distortion scenarios even without the employment of calibrated point targets. These latter would be instead required in order to calibrate a generic model (non reciprocal CTs) in a null FRA site.

2.6 Conclusions

In this chapter, two main contributions are proposed. Firstly, an accurate study of the problem is conducted from the theoretical point of view. A feasibility analysis is conducted over some realistic distortion configuration through the Singular Value Decomposition of the Jacobian matrix obtained after the linearization of the system (based on the realistic assumption that for a specific distortion parameters' configuration, the solution ambiguities in its proximity can be investigated through the Jacobian function). The possibility to solve the problem in the parameters' space close to the correct configuration is investigated, along with the prior conditioning needed to have a well-posed problem. Even if this methodology cannot ensure the uniqueness of the solution in the whole parameters domain, it clearly shows that the solution is a local optimum in the parameters domain. Therefore, if prior information about the distortion parameters is retrieved, a numerical solver can be used to obtain a correct estimation of the unknowns. This is the second contribution proposed in this work. The proposed optimization exploits the relationship between the distorted data covariance matrix and the covariance matrix of the original data, weighted by the distortion parameters. Several tests have been conducted considering both synthetic and real data, giving very encouraging results in comparison to the traditional approaches, in terms of both accuracy and computational time.

CHAPTER 3

A PS-Based Calibration Approach

External calibration on polarimetric SAR products is usually carried out by means of specifically deployed targets, passive targets or transponders and by exploiting those few extended natural areas on the globe made of uniformly distributed targets, such as the rain forests. As insightfully discussed in chapter 2, man-made targets represent indeed the only possible option to perform an absolute radiometric and polarimetric verification, whereas those sites characterized by spatially-invariant statistics provide a convenient solution for a partial polarimetric calibration and the monitoring of the antenna pattern.

Two issues about such external calibration needs then to be remarked:

- Few natural calibration sites agree to the necessary accuracy all over the globe, thus the in-orbit performance verification (remember that more than one acquisition mode needs to be monitored) can interfere with the normal acquisition orders over such sites.
- The targets deployed in order to allow an absolute radiometric and polarimetric calibration must be maintained stable all along the satellite's operational life, i.e. their RCS should be constrained to a few fractions of dB accuracy. The more stringent is the accuracy requirement the more efforts/costs must be accounted in the project.

The problem of the external radiometric and polarimetric calibration is again addressed by the present chapter, though the aim here is that of providing a mathematical framework for an innovative calibration approach based on the exploitation of a multi-baseline stack as opposed to the single-image methods. The key role in such approach is played by the polarimetric Permanent Scatterer (PS) model. The rationale is that a large cloud of low to medium quality PSs is equally effective as a small set of high quality calibrated targets. The natural consequence of such principle would be the possibility to identify a large number of candidate sites robust enough for the system monitoring and calibration all over the globe. A PS-based technique would therefore contribute to overcome the aforementioned limitations at the cost of introducing some memory and computational complexity into the problem. Herewith the reader will be first introduced to the PS model and its identification procedure in the polarimetric context and then he will be given explanation on the inversion method, herehence abbreviated as as PolPSCal, and analysis on its theoretical performance.

3.1 The polarimetric PS model

Let consider an uncalibrated stack composed of the observations of N_P Permanent Scatterers throughout N_I acquisitions. Combining the undistorted observations of the stable PS component $\mathbf{s}_p = [s_{hh_p}, s_{hv_p}, s_{vh_p}, s_{vv_p}]^T$ and unstable cell component (clutter) $\mathbf{w}_{i,p} = [w_{hh_{i,p}}, w_{hv_{i,p}}, w_{vh_{i,p}}, w_{vv_{i,p}}]^T$ with the linear distortion model $\mathbf{G}$ [16], the measured signal $\mathbf{y}_{i,p}$ of the p-th PS cell into the i-th image of the stack can be rephrased into the vector model:

$$\begin{bmatrix} y_{hh_{i,p}} \\ y_{hv_{i,p}} \\ y_{vh_{i,p}} \\ y_{vv_{i,p}} \end{bmatrix} = A_{i,p}\mathbf{G}_{i,p} \left(e^{j\phi_{i,p}} \begin{bmatrix} S_{hh_p} \\ S_{hv_p} \\ S_{vh_p} \\ S_{vv_p} \end{bmatrix} + \begin{bmatrix} w_{hh_{i,p}} \\ w_{hv_{i,p}} \\ w_{vh_{i,p}} \\ w_{vv_{i,p}} \end{bmatrix} \right) + \begin{bmatrix} N_{hh_{i,p}} \\ N_{hv_{i,p}} \\ N_{vh_{i,p}} \\ N_{vv_{i,p}} \end{bmatrix} \tag{3.1}$$

or into a more compact notation, with $A \cdot \mathbf{G}$ being referred to as $\mathbf{H}$:

$$\mathbf{y}_{i,p} = \mathbf{H}_{i,p} \left(e^{j\phi_{i,p}} \mathbf{s}_p + \mathbf{w}_{i,p} \right) + \mathbf{n}_{i,p} \tag{3.2}$$

where A is the real-valued overall image gain, ϕ is the target phase, $\mathbf{G}$ is the polarimetric distortion matrix (PDM) containing the effects of imbalances, cross-talks and Faraday rotations, and $\mathbf{n}$ accounts for the thermal noise as well as other modelization errors (distortion non-linearities, clutter non-stationary). The dependence of each element on the image or target number has been explicited in the subscripts.

Notice that in (3.1)-(3.2) a general behavior has been assigned to the distortion, $\mathbf{H}$, since it can vary with both the PS and image index. Such model would be indeed too much relaxed, leading any PS-based calibration approach to the solution of an underdetermined problem where the number of unknown parameters is larger than the data dimension.

As a matter of fact, in a real acquisition scenario, the distortion parameters can be safely assumed as slow-varying across the image, usually with a preferred range variation trend for the antenna distortion [19, 38, 49]. The only exception would be Faraday’s most severe scintillation phenomenons, which however represent a rather uncommon event and are most likely to occur at high latitudes. The distortion model and its inversion approach can then be modified accordingly, as also conveyed by the scheme in Fig. **??**. Similarly to [9] the processing can be performed upon limited portions of the image, that will be called ’imagettes’, where the parameters are supposed to be uniform. In formulas:

$$\mathbf{H}(i,p) \overset{p \in R_n}{\cong} \mathbf{H}_n(i) \tag{3.3}$$

where R_n refers to the region (group of pixels) assigned to the n^{th} imagette. The calibration procedure is then carried out individually for each imagette, being the eventual spatial correlations of the distortion not yet exploited. It is therefore possible to address the $\mathbf{H}_n(i)$ generically as $\mathbf{H}_i$. Arguably, the selection of the region width requires some careful considerations: making imagettes too wide would be indeed critical for the desired homogeneity condition, whereas making them too small would lead to a drop in the number of the PSs detected and consequently in the calibration’s performance. As rule of thumb a 4 to 10 km^2 region would be a safe choice in a urban area.

The distortion $\mathbf{H}$ assumes then the structure of the generic 4 by 4 matrix:

$$\mathbf{H}_i = A_i \begin{bmatrix} g_{11}(i) & g_{12}(i) & g_{13}(i) & g_{14}(i) \\ g_{21}(i) & g_{22}(i) & g_{23}(i) & g_{24}(i) \\ g_{31}(i) & g_{32}(i) & g_{33}(i) & g_{34}(i) \\ g_{41}(i) & g_{42}(i) & g_{43}(i) & g_{44}(i) \end{bmatrix} \equiv A_i \left\{ g(i) \right\}_{mn} \tag{3.4}$$

and its elements are handled in the estimation process as if they were independent along the stack, i.e.:

$$\begin{array}{l} p(A_i|A_j) = p(A_i) \\ p(g_{mn}(i)|g_{mn}(j)) = p(g_{mn}(i)) \end{array} \quad \forall\, m, n, i \neq j \tag{3.5}$$

where p defines the probability density function. No temporal behavior constraints has therefore been forced on the distortion parameters.

Operationally, the data is assembled into a 2D stack by arranging the N_I acquisitions of each target along the rows, and the N_P targets measures in each image along the columns, in order to obtain the $4N_I \times N_P$ matrix:

$$\mathbf{Y} = \begin{bmatrix} \mathbf{y}_{1,1} & \mathbf{y}_{1,2} & \cdots & \mathbf{y}_{1,N_P} \\ \mathbf{y}_{2,1} & \mathbf{y}_{2,2} & & \\ \vdots & & \ddots & \\ \mathbf{y}_{N_I,1} & & & \mathbf{y}_{N_I,N_P} \end{bmatrix} \tag{3.6}$$

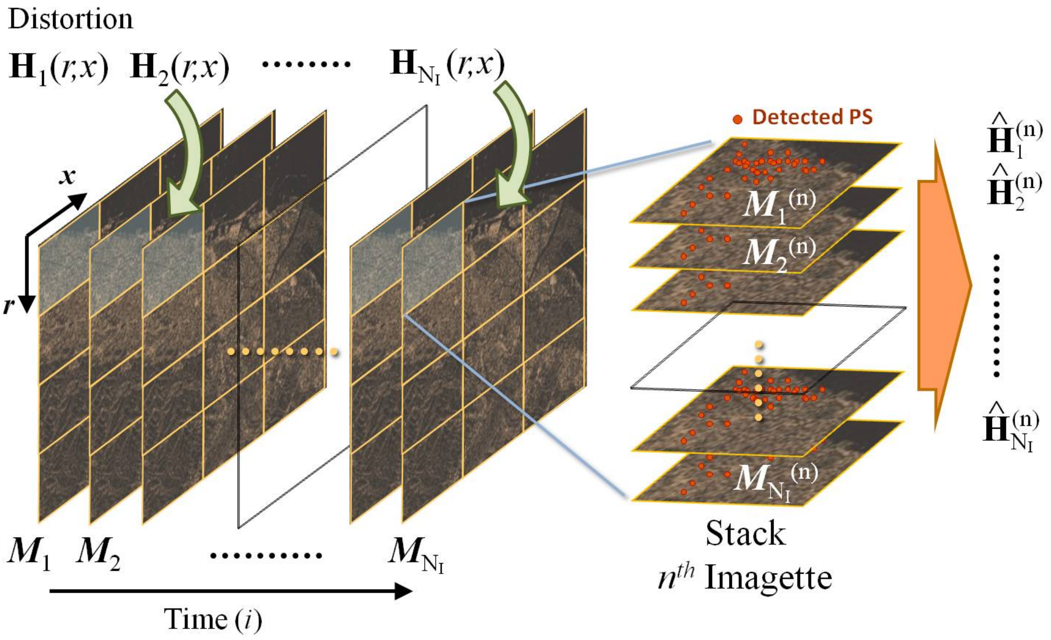

Figure 3.1: *Schematic representation of the PS-based calibration. The distorted stack made by the* N_I *observations* $\mathbf{M}_i$ *is calibrated by processing smaller portions of the image, the so-called 'imagettes'. In each imagette the Permanent Scatterers are detected and the distortion (assumed uniform inside the imagette) is estimated.*

that corresponds to:

$$\mathbf{Y} = \mathbf{\Phi} \circ \begin{bmatrix} \mathbf{H}_1 \\ \mathbf{H}_2 \\ \vdots \\ \mathbf{H}_{N_I} \end{bmatrix} \begin{bmatrix} \mathbf{s}_1 & \mathbf{s}_2 & \dots & \mathbf{s}_{N_P} \end{bmatrix} + \mathbf{N} = \mathbf{\Phi} \circ \mathbf{H_t S_t} + \mathbf{N} \tag{3.7}$$

with the operator $\circ$ standing for the Hadamard, or entry-wise, matrix product, $\mathbf{\Phi}$ and $\mathbf{N}$ being respectively the phase and noise matrices defined as:

$$\mathbf{\Phi} = \begin{bmatrix} e^{j\phi_{1,1}} & e^{j\phi_{1,2}} & \dots & e^{j\phi_{1,N_P}} \\ e^{j\phi_{2,1}} & e^{j\phi_{2,2}} & & \\ \vdots & & \ddots & \\ e^{j\phi_{N_I,1}} & & & e^{j\phi_{N_I,N_P}} \end{bmatrix} \otimes \begin{bmatrix} 1 \\ 1 \\ 1 \\ 1 \end{bmatrix} \tag{3.8}$$

$$\mathbf{N} = \mathbf{\Phi} \circ \left(\begin{bmatrix} \mathbf{H}_1 & & \\ & \ddots & \\ & & \mathbf{H}_{N_I} \end{bmatrix} \cdot \begin{bmatrix} \mathbf{w}_{1,1} & \cdots & \mathbf{w}_{1,N_P} \\ \vdots & \ddots & \\ \mathbf{w}_{N_I,1} & & \mathbf{w}_{N_I,N_P} \end{bmatrix} \right) + \begin{bmatrix} \mathbf{n}_{1,1} & \cdots & \mathbf{n}_{1,N_P} \\ \vdots & \ddots & \\ \mathbf{n}_{N_I,1} & & \mathbf{n}_{N_I,N_P} \end{bmatrix} \tag{3.9}$$

where the $\otimes$ symbol represents the Kronecker product. A model needs to be assigned at this point to the noises too. Notice to this regard that the reciprocity property applies to $\mathbf{w}$ as well as s:

$$S_{hv} = S_{vh} \tag{3.10}$$

$$w_{hv} = w_{vh} \tag{3.11}$$

since their nature is that of the physical backscatter of the cell . The clutter noise is then defined as:

$$\mathbf{w}_{i,p} \sim \mathcal{CN}\left(\mathbf{0}, \mathbf{C}_p\right) \tag{3.12}$$

$$\mathbf{C}_p = \begin{bmatrix} v_{hh_p} & \chi^*_{hh,hv_p} & \chi^*_{hh,hv_p} & \chi^*_{hh,vv_p} \\ \chi_{hh,hv_p} & v_{hv_p} & v_{hv_p} & \chi^*_{hv,vv_p} \\ \chi_{hh,hv_p} & v_{hv_p} & v_{hv_p} & \chi^*_{hv,vv_p} \\ \chi_{hh,vv_p} & \chi_{hv,vv_p} & \chi_{hv,vv_p} & v_{vv_p} \end{bmatrix} \tag{3.13}$$

i.e., a generic stationary (along acquisition time) circular complex gaussian process where the only reciprocity condition (that reduced the rank to 3) has been imposed. Each PS has its own covariance matrix, independent from those of the other targets. Differently, the residual noise $\mathbf{n}$ can be modeled with a vector of uncorrelated elements with common variance ν:

$$\mathbf{n}_{i,p} \sim \mathcal{CN}\left(\mathbf{0}, \nu_i \mathbf{I}_4\right) \tag{3.14}$$

which is appropriate for uniform thermal noise, though arguably less consistent for channel imbalances in thermal noise power and for other model-induced errors.

3.1.1 Rank of the stack

The data stack, $\mathbf{Y}$, is now investigated with respect to the rank of its different contributes. The aim is that of laying the foundation for the development of an efficient system solution. The rank of each of the matrix elements in (3.7) is readily retrieved:

Phase matrix	$\mathbf{\Phi}$	$rank = min(N_I, N_P)$
PS stable contribute	$\mathbf{H_t S_t}$	$rank \leq 3$
Noise	$\mathbf{N}$	$rank = min(4N_I, N_P)$

The case of the PS component is worth being explored into more depth. Its maximum rank is indeed limited to 3 because of the constraint on S_{hv} and S_{vh} introduced by the reciprocity property in (3.11). Let $\mathbf{H_{hh}}$, $\mathbf{H_{hv}}$, $\mathbf{H_{vh}}$, $\mathbf{H_{vv}}$ be the columns ($4N_I \times 1$ vectors) of the stacked distortion matrix, so that $\mathbf{H_t} = [\mathbf{H_{hh}}, \mathbf{H_{hv}}, \mathbf{H_{vh}}, \mathbf{H_{vv}}]$ and similarly let $\mathbf{s_{hh}}$, $\mathbf{s_{hv}}$ and $\mathbf{s_{vv}}$ be the rows of $\mathbf{s_{3t}}$ such that

$$\mathbf{s_t} = \mathbf{P} \cdot \mathbf{s_{3t}} = \begin{bmatrix} 1 & 0 & 0 \\ 0 & 1 & 0 \\ 0 & 1 & 0 \\ 0 & 0 & 1 \end{bmatrix} \begin{bmatrix} \mathbf{s_{hh}} \\ \mathbf{s_{hv}} \\ \mathbf{s_{vv}} \end{bmatrix} \tag{3.15}$$

which also determines:

$$\mathbf{s_{3t}} = \mathbf{D} \cdot \mathbf{s_t} = \begin{bmatrix} 1 & 0 & 0 & 0 \\ 0 & 1/2 & 1/2 & 0 \\ 0 & 0 & 0 & 1 \end{bmatrix} \begin{bmatrix} \mathbf{s_{hh}} \\ \mathbf{s_{hv}} \\ \mathbf{s_{hv}} \\ \mathbf{s_{vv}} \end{bmatrix} \tag{3.16}$$

with $\mathbf{D}$ and $\mathbf{P}$, related by $\mathbf{PD} = \mathbf{I}_4$ and $\mathbf{DP} = \mathbf{I}_3$, being respectively the down-scaling and up-scaling matrices. Revisiting the expression $\mathbf{H_t s_t}$ we obtain:

$$\mathbf{H_t s_t} = \mathbf{H_t P} \cdot \mathbf{s_{3t}} = \mathbf{H_{3t} s_{3t}}$$

with:

$$\mathbf{H_{3t}} = \mathbf{H_t P} = \left[\begin{array}{ccc} \mathbf{H_{hh}}, & \mathbf{H_{hv}} + \mathbf{H_{vh}}, & \mathbf{H_{vv}} \end{array} \right] \tag{3.17}$$

Identically, define the individual $\mathbf{H_3}$,$\mathbf{s_3}$,$\mathbf{w_3}$ as:

$$\mathbf{H_3}_i = \mathbf{H}_i \cdot \mathbf{P} = \begin{bmatrix} h_{11}(i) & h_{12}(i) & h_{13}(i) \\ h_{21}(i) & h_{22}(i) & h_{23}(i) \\ h_{31}(i) & h_{32}(i) & h_{33}(i) \\ h_{41}(i) & h_{42}(i) & h_{43}(i) \end{bmatrix} \equiv \{h(i)\}_{mn}$$
$$\mathbf{s_3}_p = \mathbf{D} \cdot \mathbf{s}_p = \begin{bmatrix} S_{hh_p} \\ S_{hv_p} \\ S_{vv_p} \end{bmatrix}, \quad \mathbf{w_3}_{i,p} = \mathbf{D} \cdot \mathbf{w}_{i,p} = \begin{bmatrix} w_{hh_{i,p}} \\ w_{hv_{i,p}} \\ w_{vv_{i,p}} \end{bmatrix} \tag{3.18}$$

and consequently the clutter covariance $\mathbf{C_3}$ as:

$$\mathbf{C_3}_p = \mathbf{D} \cdot \mathbf{C}_p \cdot \mathbf{P} = \begin{bmatrix} v_{hh_p} & \chi^*_{hh,hv_p} & \chi^*_{hh,vv_p} \\ \chi_{hh,hv_p} & v_{hv_p} & \chi^*_{hv,vv_p} \\ \chi_{hh,vv_p} & \chi_{hv,vv_p} & v_{vv_p} \end{bmatrix} \tag{3.19}$$

that will be often addressed herehence.

It will be now assumed that an estimate of the phases is available (this point will be better addressed in section 3.4) and that can be therefore removed from the observations, producing the new normalized data $\mathbf{Z}$:

$$\mathbf{Z} = \mathbf{\Phi}^* \circ \mathbf{Y} \tag{3.20}$$

Provided that the noise $\mathbf{N}$ affecting the data is low compared to the PS stable component, we can reasonably approximate $\mathbf{Z}$ with:

$$\mathbf{Z} \simeq \mathbf{H_{3t} s_{3t}} \tag{3.21}$$

with the number of significant singular components of the stack reducing to a maximum of 3. This value could further decrease to 2 or even to one single strong singular value when only a few PS, with no polarimetric diversity, are detected. The rank indeed depends on the number of independent scattering mechanisms that can be found in the data. Though, in a real scenario, provided that the width of the imagette and the PS detection threshold are chosen conveniently, finding such PS diversity is not a problem. In the panels of Fig. 3.2 the rank sensibility to the number of PSs is shown by reporting the first 4 singular values λ_i extracted by SVD decomposition of $\mathbf{Z}$. The stack is generated by the best PSs

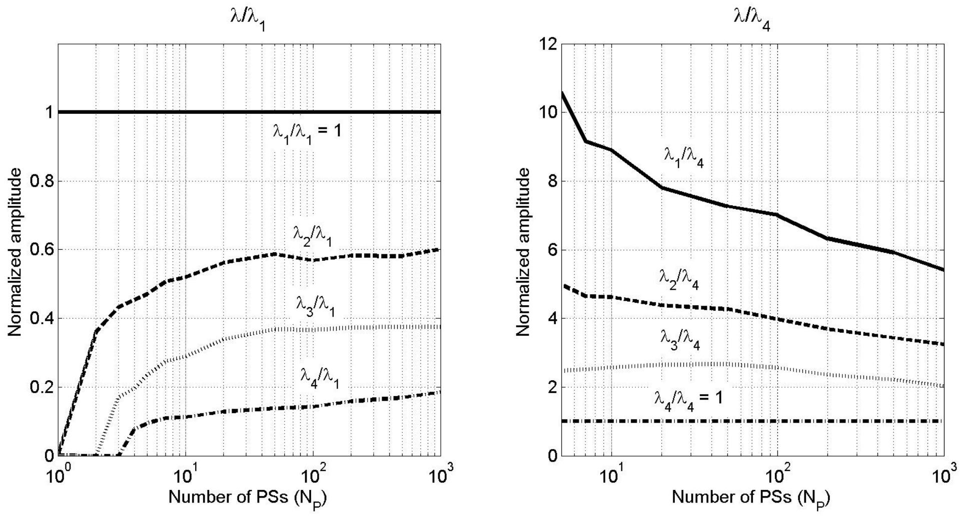

Figure 3.2: *Spectral behavior of a C-Band PS stack as a function of the number N_p of best PSs selected. The relationships between the first 4 singular values λ computed through the SVD decomposition of stacks is shown. The targets refer to an urban imagette extracted from a 26 images Radasat-2 dataset (refer to 4.1). The ratio of each singular value λ with respect to (a) the strongest value λ_1, representing the power of the dominant stable mechanism, and (b) the weaker one λ_4, representing the noise/clutter component, convey that the best mechanism power allocation is attained for higher N_p.*

identified according to (3.22). It can be noticed that when the stack is built on a very large number of PSs, including the best ones and inevitably the noisiest ones as well, λ_4 becomes stronger relatively to the other λ (Fig. 3.2a), whereas, when the PSs are good but too few ($N_P < 10$) the weight of λ_2,λ_3, as well as λ_4, tends to decrease (Fig. 3.2b), meaning that the strongest scatterers are characterized by a similar dominant mechanism. It must be specified that these results, despite being useful for a qualitative analysis on the data rank behavior, lack in generality on a quantitative standpoint, since they are specific to the characteristics of the acquisition system (in this case the C-Band Radarsat-2 satellite).

3.2 The polarimetric PS identification

The concept of Permanent Scatterers and a strategy for their detection within both an incoherent (amplitude-only) and a coherent framework was introduced by Ferretti et al. in [14]. Since then, the problem of the PS identification has been mainly addressed on single-polarization data, though it is evident that polarimetric data can add important details for the target characterization [10, 27]. A model-based parameter retrieval was proposed for dual-pol data in [36], and validated through the modest resolution resolution ERS-ENVISAT datasets. A ground-based high-resolution X-Band SAR was then used in [31, 37] to investigate the polarimetric and temporal stability of a selected group of urban features, providing evidence that high resolution combined with high frequencies delivers better characterization of the mechanisms but introduces more temporal instability as a result of small scene changes. The concept of stability, as well of that of polarimetric diversity discussed in the previous section, is indeed important for the PS-based technique here proposed since it determines its reliability. As a matter of fact, we are not interested in classifying the mechanisms in each PS cell, but in assessing their overall consistency with (3.1). Two difference typologies of stability will be defined and their relationships discussed.

3.2.1 Radiometric stability

This property can be referred either to the amplitude $|y_{ch}|$ of a single polarization channel $ch = \{hh, hv, vh, vv\}$ or to the norm of the polarimetric observation y_a, i.e. the root of the polarimetric span according to $y_a = \sqrt{SPAN_{\mathbf{y}}} = \sqrt{\mathbf{y}^H\mathbf{y}}$, where ^{H} stands for the Hermitian operator (complex conjugate). For a chosen polarization indicator $\sigma = \{y_{ch}, y_{SPAN}\}$, the stability of a target p throughout the stack can be measured by the dispersion index (DI):

$$\gamma_p = \frac{\langle \sigma_{i,p} \rangle_i}{\sqrt{\left\langle \sigma_{i,p}^2 \right\rangle_i - \langle \sigma_{i,p} \rangle_i^2}} \tag{3.22}$$

where $\langle \cdot \rangle_i$ recalls the ensemble average along the image stack, as suggested in [9, 14]. On a theoretical standpoint neither y_{ch} nor y_{SPAN} can ensure, even in case of low dispersion values in (3.22), the demanded model stability. Eventual changes in the PS signature phases indeed cannot be inferred from such metrics.

3.2.2 Polarimetric stability

The phase relationships are instead accounted by the polarimetric stability property, as well as the amplitude ratios between the channels. An intuitive way to evaluate the polarimetric stability is to make use of the eigenvalue analysis on the coherency matrix $\mathbf{T}_p$ of the p-th PS, generated as:

$$\mathbf{k}_{i,p} = \frac{1}{\sqrt{2} \cdot y_{a_{i,p}}} \begin{bmatrix} y_{hh_{i,p}} + y_{vv_{i,p}} \\ y_{hh_{i,p}} - y_{vv_{i,p}} \\ y_{hv_{i,p}} + y_{vh_{i,p}} \end{bmatrix} \tag{3.23}$$

$$\mathbf{K}_p = \begin{bmatrix} \mathbf{k}_{1,p} & \cdots & \mathbf{k}_{N_I,p} \end{bmatrix} \tag{3.24}$$

$$\mathbf{T}_p = \mathbf{K}_p \mathbf{K}_p^H \tag{3.25}$$

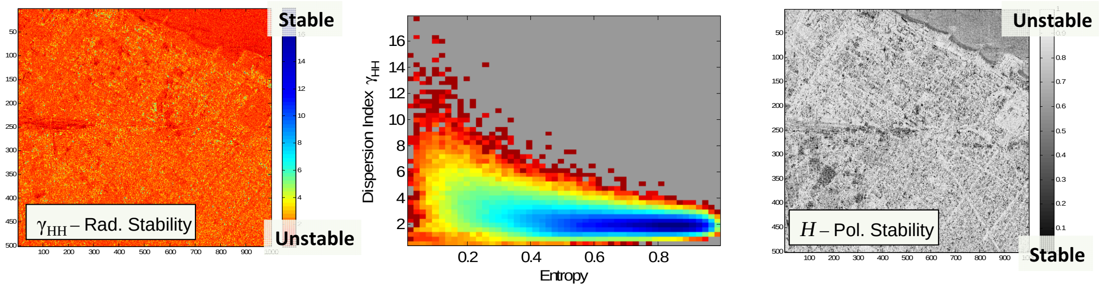

Figure 3.3: *Polarimetric (left) and radiometric (right) stability measured respectively through the Entropy decomposition and the amplitude dispersion index (in this case over the single HH channel). Their relationship is represented by 2D histogram (center).*

i.e. a 3 by 3 matrix conceived from the normalized (by the span) Pauli observations $\mathbf{k}_p$, with the cross-pol component built from the coherent summation of y_{hv} and y_{vh}. The eigenvalue analysis applied to (3.25) returns the power distribution of the cell mechanisms. From the 3 eigenvalues, λ_i, of $\mathbf{T}_p$ a measurement of the PS entropy can then be extracted as

$$H_p = -\sum_{i=1}^{3} P_i \log_3 P_i \qquad \text{with } P_i = \frac{\lambda_i}{\sum\limits_{k=1}^{3} \lambda_k}. \tag{3.26}$$

The approach is indeed analogous to the one proposed by Cloude and Pottier in [8], with a main conceptual difference represented by the averaging domain, which is space in [8] opposed to time in (3.24). A low entropy value must then be interpreted with the presence of a polarimetrically stable reflection, whereas a high entropy implies relevant temporal variations of the polarimetric mechanism inside the cell. Notice that the entropy has no sensitivity to radiometric stability, thus allowing incoherent targets which always undergo the same type of interaction with the incident field (such as the Bragg reflection of the sea surface) to attain high polarimetric stability.

Theoretically, (3.22) and (3.26) provide complementary target information. However, from their application to real scenarios a more significant connection is registered. Their relationship is reported in Fig. 3.3 for a limited frame portion of the Radarsat-2 stack of 26 images described in chapter 5. The analysis clearly conveys that the targets which are radiometrically stable (the DI on the HH channel has been shown) are also polarimetrically stable but that the opposite inference is not true. Thus, a DI thresholding would represent a valid detection criterion whereas the entropy coefficient alone is not a suitable metric. Further optimization in the development of a polarimetric PS detection algorithm that can exploit the quad-pol data to a wider extent is though encouraged.

3.2.3 The pixel-based Generalized Likelihood Ratio Test detector

A polarimetric PS detection criterion based on the Generalized Likelihood Ratio Test (GLRT) is here discussed. The aim of the detection is to establish for each cell which one of the following hypotheses:

1. the cell contains unstable mechanisms (clutter)
2. the cell is characterized by a stable backscatter (Permanent Scatterer)

is true. The occurrence of the first hypothesis is referred to as event H_0 whereas the presence of a PS is denoted with H_1. The solution borrows the Neyman-Pearson criterion, also recalled as Lakelihood Ratio Test (LRT), from the classic radar detection theory [25, 48] and extends it to the polarimetric multi-temporal context. In literature, significant research efforts can be found on polarimetric detection and contrast enhancement techniques. These are achieved either by analytic expressions for canonical targets and clutter [29, 35] or by numerical optimization [53]. Most of them, though, even when dedicated to multi-image datasets such as [39], propose to extract the clutter information from the cell neighboring pixels. Only a few attempts have been dedicated so far (see for instance [34] for dual-pol data) on optimizing a detection procedure based on the single pixel time-series. This latter is indeed our objective, especially in highly heterogeneous urban scenarios.

The proposed metric is analytically derived by further constraining the full model in (3.2) to a simplified expression as a result of these two assumptions:

1. the images are calibrated. i.e. $\mathbf{H}_i = \mathbf{I}_4$.
2. the scattering fluctuations (clutter) is stronger than the thermal noise, i.e. $\|\mathbf{w}_{i,p}\| > \|\mathbf{n}_{i,p}\|$

that lead to the approximated model:

$$\mathbf{y_3}_{i,p} = \mathbf{D} \cdot \mathbf{y}_{i,p} \simeq e^{j\phi_{i,p}} \mathbf{s_3}_p + \mathbf{w_3}_{i,p} \tag{3.27}$$

Notice that the first condition can be attained by proper image pre-processing (see section 3.4), whereas the second property is intrinsic to the specific scene and acquisition system. Arguably, it represents a reasonable assumption for C-band and X-band but should be carefully verified on low-frequency systems with weaker backscatter values. The LRT-based choice between the events

$$H_0: \quad \mathbf{y_3}_{i,p} = \mathbf{w_3}_{i,p} \tag{3.28}$$

$$H_1: \quad \mathbf{y_3}_{i,p} = e^{j\phi_{i,p}} \mathbf{s_3}_p + \mathbf{w_3}_{i,p} \tag{3.29}$$

can be then expressed through

$$LR_p = \frac{\mathcal{L}\left(\mathbf{Y}_{\mathbf{3}p} \middle| \left\{ \{\phi_{i,p}\}_{i=1}^{N_I}, \mathbf{s}_{\mathbf{3}p}, \mathbf{C}_{\mathbf{3}p} \right\}\right)}{\mathcal{L}\left(\mathbf{Y}_{\mathbf{3}p} \middle| \left\{ \{\phi_{i,p}\}_{i=1}^{N_I}, \mathbf{s}_{\mathbf{3}p} = \mathbf{0}, \mathbf{C}_{\mathbf{3}p} \right\}\right)} \underset{H_0}{\overset{H_1}{\gtrless}} T_\nu \tag{3.30}$$

where T_ν is a threshold that must be tuned with relation to the required probability of false alarm, P_{fa}, or missing detection, P_{md} and $\mathcal{L}$ recalls the likelihood of the p-th target stack

$$\begin{aligned} \mathbf{Y}_{\mathbf{3}p} &= \left[\begin{array}{ccc} \mathbf{y}_{\mathbf{3}1,p} & \cdots & \mathbf{y}_{\mathbf{3}N_I,p} \end{array} \right], \\ &\simeq \mathbf{s}_{\mathbf{3}p} \cdot \underbrace{\left[\begin{array}{ccc} e^{j\phi_{1,p}} & \cdots & e^{j\phi_{N_I,p}} \end{array} \right]}_{\substack{\Phi_p \\ \leftarrow \quad \text{Rank 1} \quad \rightarrow}} + \underbrace{\left[\begin{array}{ccc} \mathbf{w}_{\mathbf{3}1,p} & \cdots & \mathbf{w}_{\mathbf{3}N_I,p} \end{array} \right]}_{\substack{\mathbf{W}_{\mathbf{3}p} \\ \leftarrow \quad \text{Rank 3} \quad \rightarrow}} \end{aligned} \tag{3.31}$$

where the stable term is rank one whereas the clutter term, $\mathbf{W}_{\mathbf{3}p}$, is full rank. The practical implementation of (3.30) demands however the knowledge of $\{\phi_{i,p}\}_{i=1}^{N_I}, \mathbf{s}_{\mathbf{3}p}, \mathbf{C}_{\mathbf{3}p}$ that are unknowns within the PS problem. The $\hat{\mathbf{s}}_{\mathbf{3}p}$ and $\hat{\phi}_{i,p}$ estimates can be in a first moment retrieved through SVD from $\mathbf{Y}_{\mathbf{3}p}$, exploiting its model separability according to

$$\mathbf{Y}_{\mathbf{3}p} = \sum_{i=k}^{3} \alpha_k \mathbf{u}_k \mathbf{v}_k^H \rightarrow \mathrm{SVD}(\mathbf{Y}_{\mathbf{3}p}) \rightarrow \{\alpha_k, \mathbf{u}_k, \mathbf{v}_k\} \quad \text{with } \alpha_1 > \alpha_2 > \alpha_3 \tag{3.32}$$

$$\mathbf{s}_{\mathbf{3}p} \Phi_p \simeq \alpha_1 \mathbf{u}_1 \mathbf{v}_1^H$$

$$\Phi_p \simeq \mathbf{v}_1^H$$

$$\mathbf{s}_{\mathbf{3}p} \Phi_p \frac{\mathbf{v}_1}{N_I} \simeq \alpha_1 \mathbf{u}_1 \mathbf{v}_1^H \frac{\mathbf{v}_1}{N_I}$$

that readily yield

$$\hat{\mathbf{s}}_{\mathbf{3}p} = \frac{\alpha_1 \mathbf{u}_1 \left\|\mathbf{v}_1\right\|^2}{N_I} \tag{3.33}$$

$$\left[\begin{array}{ccc} \hat{\phi}_{1,p} & \cdots & \hat{\phi}_{N_I,p} \end{array} \right] = -\angle \mathbf{v}_1^H \tag{3.34}$$

with α_k being the real singular values sorted amplitude-wise and $\mathbf{u}_k, \mathbf{v}_k$ the associated complex singular vectors. The covariance can then be easily retrieved by means of the LS estimator:

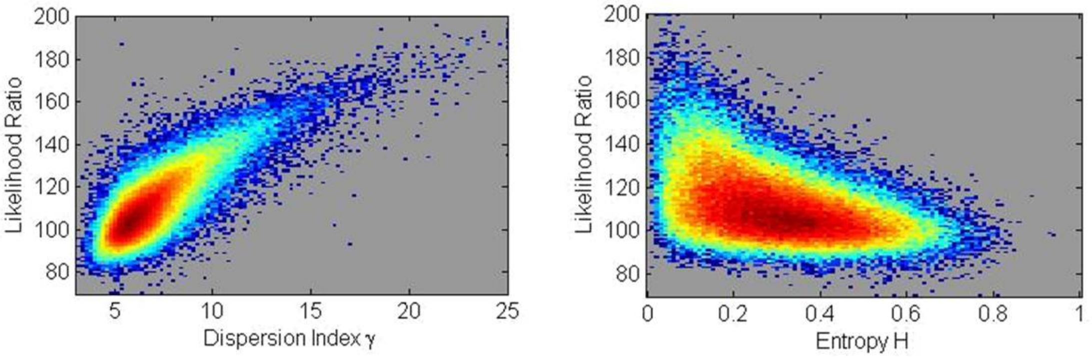

Figure 3.4: *Relationship of the chosen PS quality metric, the Generalized Likelihood Ratio, with the radiometric (left) and polarimetric (right) estimates by means of the DI (on span) and Entropy coefficients.*

$$\hat{\mathbf{C}}_{\mathbf{3}p} = \frac{1}{N_I}\sum_{i=1}^{N_I}(\mathbf{y}_{\mathbf{3}i,p} - e^{j\hat{\phi}_{i,p}}\hat{\mathbf{s}}_{\mathbf{3}p})(\mathbf{y}_{\mathbf{3}i,p} - e^{j\hat{\phi}_{i,p}}\hat{\mathbf{s}}_{\mathbf{3}p})^H \tag{3.35}$$

which also represents the optimum in the ML sense. The replacement of the nominal values with the parameter estimates leads to the criterion known as Generalized Likelihood Ratio Test:

$$LR_p = \frac{\mathcal{L}\left(\mathbf{Y}_p \middle| \left\{ \left\{ \hat{\phi}_{i,p} \right\}_{i=1}^{N_I}, \mathbf{s}_{\mathbf{3}p} = \hat{\mathbf{s}}_{\mathbf{3}p}, \mathbf{C}_{\mathbf{3}p} = \hat{\mathbf{C}}_{\mathbf{3}p} \right\} \right)}{\mathcal{L}\left(\mathbf{Y}_p \middle| \left\{ \mathbf{s}_{\mathbf{3}p} = \mathbf{0}, \mathbf{C}_{\mathbf{3}p} = \frac{1}{N_I} \cdot \mathbf{Y}_p \mathbf{Y}_p^H \right\} \right)} \underset{H_0}{\overset{H_1}{\gtrless}} T_\gamma \tag{3.36}$$

where the covariance matrix in the case of the clutter hypothesis has been estimated as the target average power. Through proper handling of the likelihood ratio (the reader is referred to section in appendix) we yield the simplified expression:

$$\hat{\gamma}_{LR} = \ln LR = N_I \cdot \ln\left(1 + \hat{\mathbf{s}}_{\mathbf{3}}^H \hat{\mathbf{C}}_{\mathbf{3}}^{-1} \hat{\mathbf{s}}_{\mathbf{3}}\right) \underset{\text{Noise}}{\overset{PS}{\gtrless}} T_\gamma \tag{3.37}$$

which holds a strong resemblance with the PWF (Polarimetric Whitening Filter) approach [29]. The difference from this latter, though, is substantial, since (3.37) uses some estimates $\hat{\mathbf{s}}$ of the target signature instead of the direct data observation $\mathbf{y}$. As shown in Fig. 3.4, the adopted GLRT-based detection in (3.60) ensures both radiometric and polarimetric stability: for the 26-image RS2 stack a GLR threshold of 150 detects target with DI (span) better than 10 and a entropy lower than 0.2. Besides, its theoretical performance, evaluated by means of the missing detection probability (P_{md}) at CFAR (Constant False

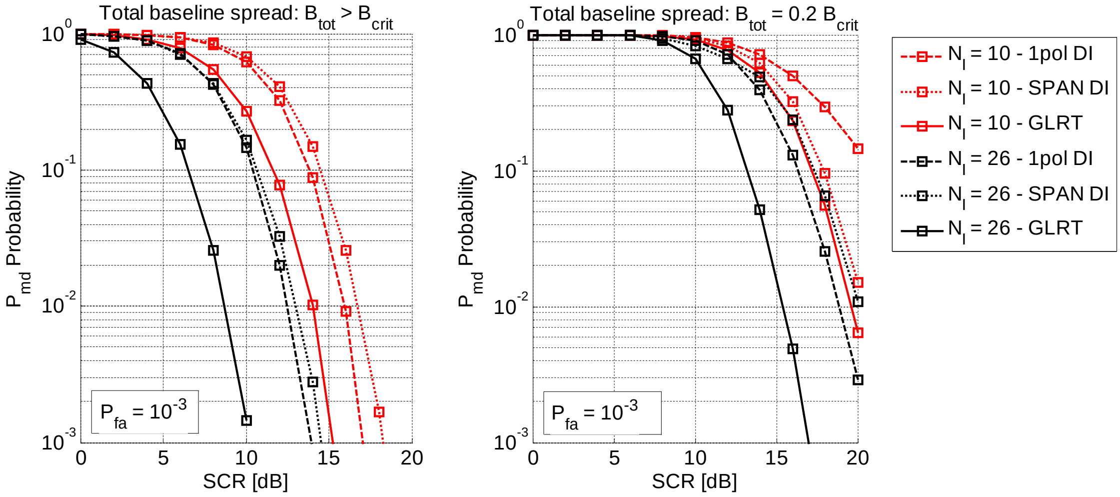

Figure 3.5: *Missing detection probability (P_{md}) curves corresponding to CFAR conditions set to $P_{fa} = 10^{-3}$. The simulations have been conducted on stacks with different baseline configurations, one with spacing between acquisitions large enough to experience complete decorrelation (**left**) and one with narrower baseline spread B_{tot} with respect to the critical baseline B_{crit} (**right**), this latter being consistent to the RS2 used for the validation in chapter 4. Three different methods, the Dispersion Index on the single channel (dot), on the polarimetric SPAN (dash) and the proposed GLRT method (solid), were assessed on $N_I = 10, 26$ stack configurations.*

Alarm Rate) conditions is better than the traditional DI. The curves in Fig. 3.5 show such comparison for false alarm probability $P_{fa} = 10^{-3}$. The detection quality was assessed as a function of the target quality, of the number of images and of the geometric decorrelation. The limited baseline spread B_{tot} has indeed the major impact for distributed targets in urban scenarios. It can be observed that for highly decorrelated acquisitions ($B_{tot} > B_{crit}$) the SCR and the number of images demanded is intuitively lower than that required at narrower baseline acqiositions ($B_{tot} = 0.2B_{crit}$ in the right panel) where distributed target has more stable behaviour. The proposed method registers significant performance improvements in every tested configuration, with the exception of the most unfavourable one characterized by small N_I and critical decorrelation, where the P_{md} is comparable with the one returned by the SPAN dispersion index. The difference in the quality returned by the GLRT criterion with respect to the SPAN dispersion index is qualitatively presented in Fig. 3.6. The two techniques has been applied to a RS2 imagette ($N_I = 26$) with half of the area covered by forest and half inhabited. Even on a rough qualitative assessment, the GLRT clearly has the edge over the DI technique inside the vegetated area, where the both the geometrical but in a particular way the temporal decorrelation of the scatterers is the strongest.

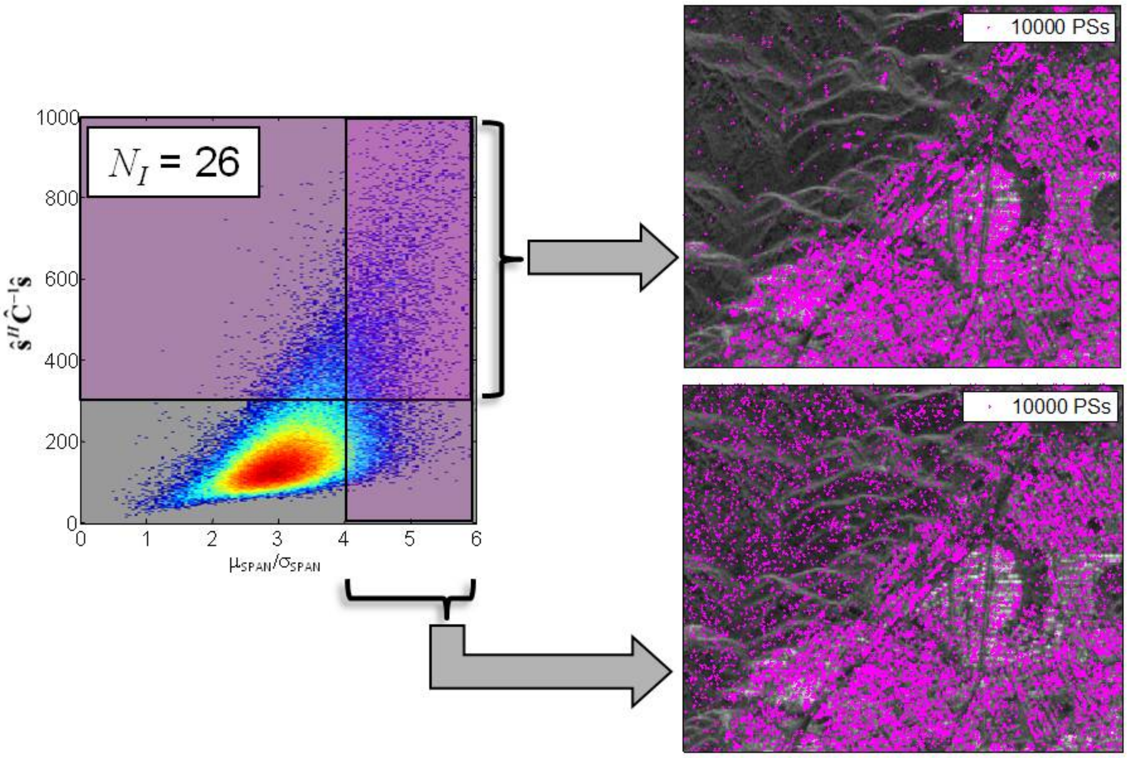

Figure 3.6: *Comparison between the GLRT and the SPAN Dispersion criterions for the polarimetric PS detection. The target selection has been forced to the 10000 strongest ones for both methods. Only 55 % of the PSs are common to the 2 sets.*

3.3 Formalization of the PS-based calibration problem

Calibrating a SAR stack means compensating the distortion that affects the data so that the polarimetric information within each stack acquisition becomes consistent with the calibrated information of other datasets. According to the linear distortion model adopted in (3.1) the calibrated polarimetric observation $\mathbf{x} = [x_{hh}\, x_{hv}\, x_{vv}]^T$ of a generic scatterer at range and azimuth coordinates (r, x) in image i would be attained by means of the simple operation:

$$\mathbf{x}(i,(r,x)) = \hat{\mathbf{H}}^{\dagger}_{\mathbf{3}_i}\mathbf{y}(i,(r,x)) \tag{3.38}$$

where $\hat{\mathbf{H}}_\mathbf{3}$ is the estimated 4×3 PDM in (3.18), the superscript † recalls the pseudo-inverse matrix operator and $\mathbf{y}$ is the uncalibrated 4-elements data vector. Notice that if no physical consistency is required for $\hat{\mathbf{H}}_\mathbf{3}$, with respect to a specific set of parameters $\boldsymbol{\Theta}$(i.e. cross-talks, channel imbalances and Faraday rotations), the estimates $\hat{\mathbf{H}}_\mathbf{3}$ are accepted despite:

$$\nexists\, \boldsymbol{\Theta} \,\Big|\, \mathbf{H_3}(\boldsymbol{\Theta}) = \hat{\mathbf{H}}_\mathbf{3}.$$

Differently, when a robust prediction of $\boldsymbol{\Theta}$ can be achieved, these latter can be exploited in the calibration procedure, leading to

$$\mathbf{x}(i,(r,x)) = \mathbf{H_3}(\hat{\boldsymbol{\Theta}}_i)^{-1}\mathbf{y}(i,(r,x)). \tag{3.39}$$

where the reconstructed matrix $\mathbf{H_3}(\hat{\boldsymbol{\Theta}}_i)$ can hopefully benefit from the damping of its noisiest and inconsistent h_{mn} elements. This is indeed the approach adopted by the reference contributions in literature, such as [16, 38, 49] to name a few. Furthermore, the retrieval of $\boldsymbol{\Theta}$ represents itself the aim of the polarimetric investigation when the monitoring of the system stability or the evaluation of the Faraday rotation angle (L-Band) are concerned. In this case we should refer to the problem more as a problem of estimation than as a problem of calibration.

Notice then that when the additive noise is negligible the calibration procedure should lead ideally to:

$$\mathbf{x}(i,(r,x)) = \hat{\mathbf{H}}^{\dagger}_{\mathbf{3}_i}\mathbf{H}_{\mathbf{3}_i}\mathbf{s_3}(i,(r,x)) \simeq \mathbf{s_3}(i,(r,x)). \tag{3.40}$$

When the expression of $\mathbf{H_3}$ is known, such as in controlled or simulated experiments, the accuracy of the calibration in (3.38) and (3.39) can be quantitatively assessed by using the the Wang-Ainsworth-Lee metric [50] here adapted to the 3×3 residual distortion $\hat{\mathbf{H}}^{\dagger}_{\mathbf{3}_i}\mathbf{H}_{\mathbf{3}_i}$. The quality is measured through the maximum normalized error (MNE):

$$MNE = \max_{\mathbf{s_3}} \frac{\left\| \left(\mathbf{I_3} - \hat{\mathbf{H}}^{\dagger}_{\mathbf{3}_i}\mathbf{H}_{\mathbf{3}_i}\right)\mathbf{s_3} \right\|}{\|\mathbf{s_3}\|} = \sqrt{\lambda_{max}[(\mathbf{I_3} - \hat{\mathbf{H}}^{\dagger}_{\mathbf{3}_i}\mathbf{H}_{\mathbf{3}_i})^H \cdot (\mathbf{I_3} - \hat{\mathbf{H}}^{\dagger}_{\mathbf{3}_i}\mathbf{H}_{\mathbf{3}_i})]}. \tag{3.41}$$

where λ_{max} is the largest eigenvalue of the enclosed matrix $(\mathbf{I_3} - \hat{\mathbf{H}}^{\dagger}_{\mathbf{3}_i}\mathbf{H}_{\mathbf{3}_i})^H(\mathbf{I_3} - \hat{\mathbf{H}}^{\dagger}_{\mathbf{3}_i}\mathbf{H}_{\mathbf{3}_i})$. However, the estimation of (3.41) in real scenarios, where the target signatures $\mathbf{s_3}$ are all unknown, is not possible, and other criterions must therefore be adopted. A reasonable criterion for the retrieval of a generic parameter set Θ would then be, with reference to (3.20) and (3.21):

$$\hat{\Theta} = \underset{\Theta}{\text{argmin}}\, d\left(\mathbf{Y}, \hat{\mathbf{Y}} = \Phi(\Theta) \circ [\mathbf{H_{3t}}(\Theta)\mathbf{s_{3t}}(\Theta)]\right) \tag{3.42}$$

which reads as the minimization of a convenient distance d between the data stack $\mathbf{Y}$ and the stack reconstructed from the model estimates, $\hat{\mathbf{Y}}$. Assuming that no a-priori information is available, the set of unknowns, Θ, in the PS problem so far introduced accounts for the parameters associated to the targets:

– $3N_P$ complex backscatter coefficients S_{hh},S_{hv},S_{vv}
– $3N_P$ real clutter variances v_{hh},v_{hv},v_{vv}
– $3N_P$ complex covariances $\chi_{hh,hv}$,$\chi_{hh,vv}$,$\chi_{hv,vv}$

those associated to the images:

– $12N_I$ complex distortion elements h_{mn} (most general linear model)
– N_I thermal noise variances ν

and the phase matrix in (3.8), comprising

– $N_I N_P$ phases ϕ

that add significant complexity to the problem. The overall number is $N_P(N_I+15)+13N_I$ real unknowns that must be estimated from $8N_P N_I$ real equations. The balance is therefore positive, meaning that the system is overdetermined, when

$$8N_P N_I > N_P(N_I + 15) + 13N_I \tag{3.43}$$

yielding

$$N_I \geq 3 \quad \text{when} \quad N_P \gg N_I \tag{3.44}$$

which conveys that, when a large number of PSs is detected, the minimum number of images required for calibration is $N_I = 3$. Since the problem is not separable, the optimal solution to (3.42) would demand a joint parameter optimization over the whole set Θ. An exhaustive exploration of the parameter space can be immediately excluded, due to the very large number of parameters. On the opposite side, the derivation of exact analytic expressions, considering the problem complexity, appears identically unfeasible. This necessarily leads to the implementation of suboptimal solutions whose robustness can be ensured by means of a convenient choice of the metric d and a smart design of each solution step. Some minor approximation will be also applied to the model.

3.4 The proposed calibration algorithm

The PolPSCal technique, whose workflow is outlined in Fig. 3.7, has been designed with the aim of providing a comprehensive and, at the same time, efficient solution to the PS model estimation problem. The technique receives as input a coregistered uncalibrated dataset and returns a calibrated stack together with the estimates of the distortion and the extracted PS information, as illustrated in Fig. 3.7. It is composed of four main operational blocks:

- The algorithm initialization consisting in an initial coarse estimation of the model parameters
- A PS selection procedure
- A parameter estimation block, that can be reiterated together with the detection until convergence of the estimates
- A final normalization of the PS-based estimates and data calibration where integration with external information is carried out

A mathematical description of the algorithm steps is now provided. The initial estimation of the distortion parameters (coarse calibration) can be approached by exploiting well-known techniques such as [19,38] in case of generic distortions or [2,5] for the correction of Faraday rotations, which provide a good partial polarimetric calibration. Such initialization is in particular recommended in case of strong miscalibration to ensure a robust convergence of the algorithm. By means of (3.39), it leads to the calibrated data $\mathbf{x}_{i,p}$, that will be used in the next step for the initialization of the target features, $\hat{\mathbf{s}}_{\mathbf{3}p}$, $\hat{\mathbf{C}}_{\mathbf{3}p}$ and $\hat{\phi}_{i,p}$. These estimates can be attained through (3.32-3.35), by replacing the data in (3.31) with $\mathbf{x}_{i,p}$. The first PS detection is then carried out through the criterion already pointed out in (3.37). A joint estimation of the PDMs and of the PS backscatter is hence conceived.

3.4.1 SVD-based estimation of the polarimetric distortion

The first step consists in building the stack $\mathbf{Y}$ in accordance with (3.6). Then the phase estimates $\hat{\phi}$ must be removed from $\mathbf{Y}$ as reported in (3.6) to get the stack $\mathbf{Z}$. Since the structure of $\mathbf{Z}$ is that of a separable model, a Singular Value Decomposition (SVD) approach configures as the most straightforward, but nonetheless efficient (on the computational times standpoint), inversion solution. With reference to the low-rank approximation theory [13,44], it can be demonstrated that the SVD approximation represents the optimum with regard to the Frobenius norm minimization of the residual. In our case this leads to the estimates:

$$\hat{\mathbf{H}}_{\mathbf{3}i}, \hat{\mathbf{s}}_{\mathbf{3}p} = \underset{\mathbf{H}_{\mathbf{3}i}, \mathbf{s}_{\mathbf{3}p}}{\operatorname{argmin}} \|\mathbf{Z} - \mathbf{Z}^{(3)}\|_F \tag{3.45}$$

where $\|\cdot\|_F$ identifies the Frobenius norm and $\mathbf{Z}^{(3)}$ is the SVD approximation of $\mathbf{Z}$ truncated to the third singular component. Remember that (3.45) is satisfied only if at least 3 independent scattering mechanisms are present throughout the stack, as discussed in section 3.1.1. Here hence we will always assume to operate on the most desirable condition,

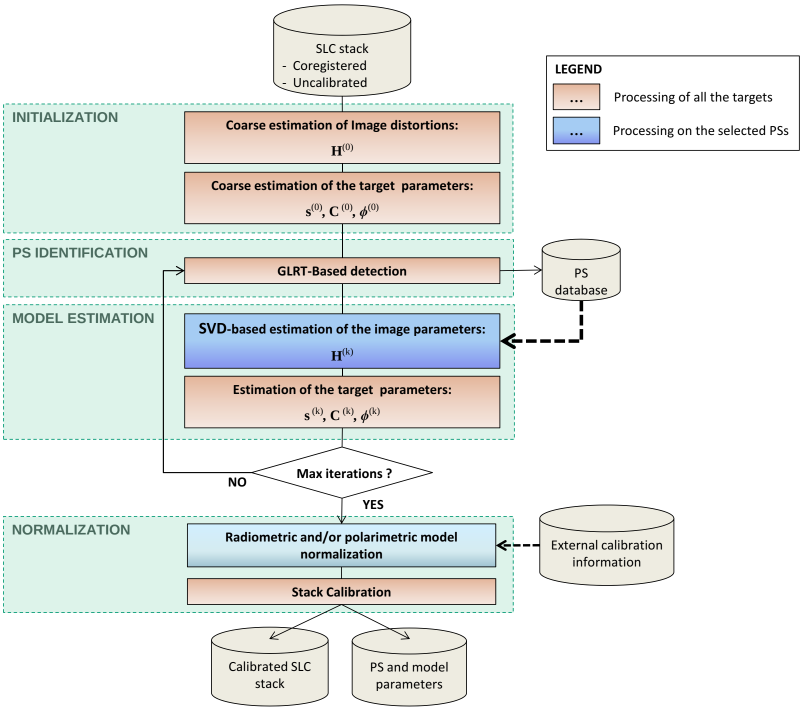

Figure 3.7: *Schematic representation of the iterative PS-based calibration solution, namely the PolPSCal technique.*

which is also the most realistic one, i.e. the case $rank(\mathbf{H_t s_t}) = 3$. The application of SVD to the stack does not return the exact $\hat{\mathbf{H}}_{\mathbf{3}i}, \hat{\mathbf{s}}_{\mathbf{3}p}$ estimates, but the matrices $\mathbf{U}, \mathbf{\Lambda}, \mathbf{V}$:

$$\mathbf{Z}^{(3)} = \mathbf{U\Lambda V}^H \tag{3.46}$$

$$\mathbf{U} = \begin{bmatrix} \mathbf{U}_1 \\ \vdots \\ \mathbf{U}_{N_I} \end{bmatrix}, \quad \mathbf{V}^H = [\mathbf{v}_1 \dots \mathbf{v}_{N_P}] \tag{3.47}$$

where $\mathbf{U}$ and $\mathbf{V}$, with dimensions of $4N_I \times 3$ and $N_P \times 3$ respectively, are sets of orthonormal vectors (namely the left and right singular vectors) and $\mathbf{\Lambda}$ is the 3×3 diagonal matrix carrying the singular values. It is readily demonstrated that the solution is determined up to the 3×3 arbitrary matrix $\mathbf{B}$:

$$\mathbf{U\Lambda V}^H = \mathbf{UB} \cdot \mathbf{B}^{-1}\mathbf{\Lambda V}^H = \mathbf{H_t s_t} \tag{3.48}$$

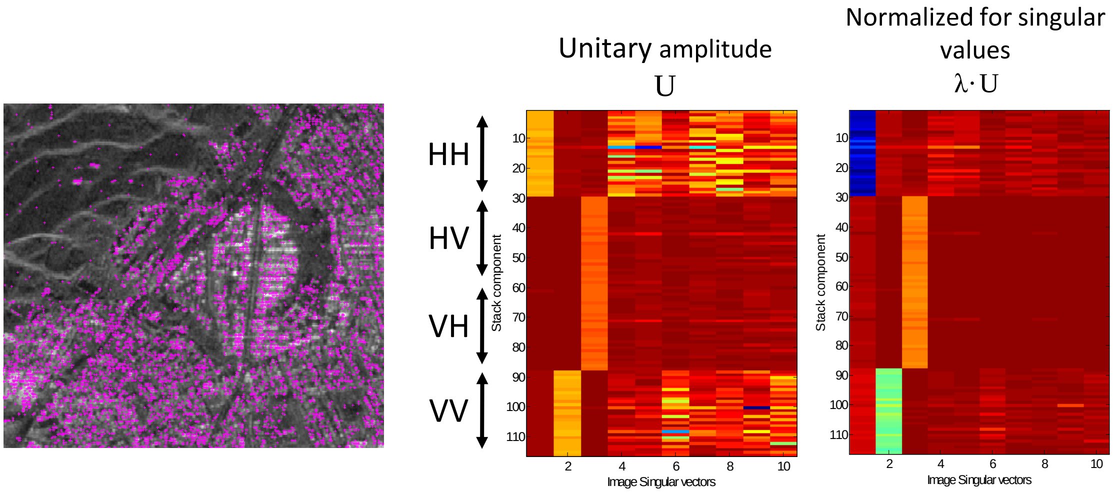

Unitary amplitude U

Normalized for singular values λ·U

Figure 3.8: *SVD analysis on a PS stack (left) extracted from the Barcelona RS2 dataset, $N_I = 29$. The 10 strongest left singular components (the ones associated to the image distortion) have been illustrated both in their unitary amplitude form (center) and scaled for their energy (right).*

thus attaining:

$$\begin{aligned} \mathbf{H_t} &= \mathbf{UB} \\ \mathbf{s_t} &= \mathbf{B}^{-1}\mathbf{\Lambda}\mathbf{V}^H. \end{aligned} \tag{3.49}$$

The ambiguity affects the polarimetric purity generating an additional cross-talk that cannot be solved without using external data. Nevertheless the PolPSCal procedure will employ the estimates

$$\begin{aligned} \tilde{\mathbf{H}}_{\mathbf{3}i} &= \mathbf{U}_i \simeq \mathbf{H}_{\mathbf{3}i} \cdot \mathbf{B}^{-1} \\ \tilde{\mathbf{s}}_{\mathbf{3}p} &= \mathbf{\Lambda}\mathbf{v}_p^H \simeq \mathbf{B} \cdot \mathbf{s}_{\mathbf{3}p} \end{aligned} \tag{3.50}$$

along the refinement steps that will follow. The effects of such induced cross-talk are shown on real dataset in Fig. 3.8. The most energetic left singular components (first 10 vectors of $\mathbf{U}$) are reported for a Radarsat-2 PS stack (29 images) both with and without normalization for the singular values. The phases have been estimated and removed from the data, which have been assumed perfectly calibrated. Notice that the stack has clearly rank 3 and that the principal components are not exactly matched to the the HH, HV and VV polarizations of $\mathbf{s_t}$, for the effect of the ambiguity $\mathbf{B}$.

3.4.2 Estimation of the PS parameters and update of the PS stack

When tough distortion scenarios are addressed, only a narrow set of PSs can be identified in the first detection step. A processing scheme based on the iterative refinement of both the detection and estimation steps has been then developed, the rationale being that the enhancement in the estimates yields a more effective detection and the consequent increase in the number of PSs lead to more accurate estimates. The purpose is to entrust the algorithm with the capability of re-evaluating at each step the quality of all the targets according to the updated estimates, and thus of inserting new targets that were left out in the previous iteration. It is evident that such mechanism cannot rely on the SVD-based estimator that operates only on the PSs already selected. As conveyed by the workflow in Fig. 3.7, updated estimates should instead be achieved for all the targets in the imagette before performing a new detection. An analytic procedure based on the sequential Least Squares assessment of all the target parameters, including the phases, has been developed.

It relies on the noise model assumption:

$$\mathbf{y}_{i,p} \simeq \tilde{\mathbf{H}}_{\mathbf{3}i} \left(e^{j\phi_{i,p}} \tilde{\mathbf{s}}_{\mathbf{3}p} + \tilde{\mathbf{w}}_{\mathbf{3}i,p} \right) \tag{3.51}$$

which exploits the fact that PSs are usually characterized by backscatter fluctuations that are stronger than the thermal noise. The data are then calibrated for the ambiguous distortion returned by the SVD[1], $\tilde{\mathbf{H}}_{\mathbf{3}}$, by means of

$$\mathbf{x}_{i,p} = (\tilde{\mathbf{H}}_{\mathbf{3}i}^{H} \, \tilde{\mathbf{H}}_{\mathbf{3}i})^{-1} \tilde{\mathbf{H}}_{\mathbf{3}i}^{H} \, \mathbf{y}_{i,p} = \tilde{\mathbf{H}}_{\mathbf{3}i}^{\dagger} \, \mathbf{y}_{i,p}. \tag{3.52}$$

attaining the 3-component vectors $\mathbf{x}_{i,p}$. Since the $\tilde{\mathbf{H}}_{\mathbf{3}}$ is full-rank (see section 3.1.1), the pseudo inverse operator always satisfies $\tilde{\mathbf{H}}_{\mathbf{3}}^{\dagger}\tilde{\mathbf{H}}_{\mathbf{3}} = \mathbf{I}$ and consequently:

$$\tilde{\mathbf{H}}_{\mathbf{3}}^{\dagger}\mathbf{H}_{\mathbf{3}} \simeq \mathbf{B}. \tag{3.53}$$

By substituting (3.51) into (3.52) and accounting for (3.53) the probability density function of $\mathbf{x}_{i,p}$ takes the expression:

$$\begin{aligned} p_x(\mathbf{x}_{i,p}) \simeq \frac{1}{\pi^3 \cdot \det(\mathbf{B}\mathbf{C}_{\mathbf{3}p}\mathbf{B}^H)} \times \\ \exp\left(-(e^{-j\phi_{i,p}}\mathbf{x}_{i,p} - \mathbf{B}\,\mathbf{s}_{\mathbf{3}p})^H (\mathbf{B}\mathbf{C}_{\mathbf{3}p}\mathbf{B}^H)^{-1} (e^{-j\phi_{i,p}}\mathbf{x}_{i,p} - \mathbf{B}\,\mathbf{s}_{\mathbf{3}p}) \right) \end{aligned} \tag{3.54}$$

where the following relationships have been exploited:

$$\tilde{\mathbf{H}}_{\mathbf{3}i}^{\dagger}\mathbf{H}_i\mathbf{s}_p \simeq \mathbf{B} \cdot \mathbf{s}_{\mathbf{3}p} \tag{3.55}$$

$$E\left[\tilde{\mathbf{H}}_{\mathbf{3}i}^{\dagger}\mathbf{H}_i\mathbf{w}_{i,p}\mathbf{w}_{i,p}^H\mathbf{H}_i^H\tilde{\mathbf{H}}_{\mathbf{3}i}^{\dagger H} \right] \simeq \mathbf{B}\mathbf{C}_{\mathbf{3}p}\mathbf{B}^H \tag{3.56}$$

---

[1] The notation $\tilde{\mathbf{H}}$ has been used instead of $\hat{\mathbf{H}}$ because of the uncertainty. The parameters retrieved through SVD cannot in fact be considered a direct estimate of $\mathbf{H}_{\mathbf{3}}$ but of its distorted version $\mathbf{H}_{\mathbf{3}}\mathbf{B}^{-1}$

Having removed the timely dependence on the distortion $\mathbf{H}_i$, the complex multivariate gaussian distribution in (3.54) is stationary with time, the benefit being that its mean and covariance optimum estimates represent indeed common knowledge. With reference to the normalized data $e^{-j\phi_{i,p}}\mathbf{x}_{i,p}$, the mean $\tilde{\mathbf{s}}_{\mathbf{3}p}$ is then retrieved in the LS sense as:

$$\tilde{\mathbf{s}}_{\mathbf{3}p} = \frac{1}{N_I}\sum_{i=1}^{N_I} e^{-j\phi_{i,p}}\mathbf{x}_{i,p} \simeq \mathbf{B}\,\mathbf{s}_{\mathbf{3}p} \tag{3.57}$$

whereas the clutter covariance is obtained with:

$$\tilde{\mathbf{C}}_{\mathbf{3}p} = \frac{1}{N_I}\sum_{i=1}^{N_I}(e^{-j\phi_{i,p}}\mathbf{x}_{i,p} - \tilde{\mathbf{s}}_{\mathbf{3}p})(e^{-j\phi_{i,p}}\mathbf{x}_{i,p} - \tilde{\mathbf{s}}_{\mathbf{3}p})^H \simeq \mathbf{B}\mathbf{C}_{\mathbf{3}p}\mathbf{B}^H \tag{3.58}$$

When the phases ϕ are not provided externally (e.g. by a PS processor) they must be replaced in (3.57) and (3.58) by their estimates $\hat{\phi}$, which are refined inside the PolPSCal algorithm as well. With reference to (3.51) their LS estimates are in fact obtained by:

$$\hat{\phi}_{i,p} = \angle\left(\mathbf{x}_{i,p}^H\tilde{\mathbf{s}}_p\right) \tag{3.59}$$

In consideration of the estimates (3.57)-(3.59), the metric $\hat{\gamma}_{LR}$ presented in (3.37) can be revisited, yielding indeed:

$$\begin{aligned}\hat{\gamma}_{LR} = \ln&\left[\frac{\mathcal{L}\left(\mathbf{Y}\,\middle|\left\{\tilde{\mathbf{H}}_\mathbf{3}, \mathbf{s}_\mathbf{3} = \tilde{\mathbf{s}}_\mathbf{3}, \hat{\phi}, \mathbf{C}_\mathbf{3} = \tilde{\mathbf{C}}_\mathbf{3}\right\}\right)}{\mathcal{L}\left(\mathbf{Y}\,\middle|\left\{\tilde{\mathbf{H}}_\mathbf{3}, \mathbf{s}_\mathbf{3} = \mathbf{0}, \hat{\phi}, \mathbf{C}_\mathbf{3} = \langle\mathbf{x}\mathbf{x}^H\rangle\right\}\right)}\right]\\ \simeq&N_I \cdot \ln\left(1 + \tilde{\mathbf{s}}_\mathbf{3}^H\tilde{\mathbf{C}}_\mathbf{3}^{-1}\tilde{\mathbf{s}}_\mathbf{3}\right) \underset{\text{Noise}}{\overset{PS}{\gtrless}} T_\gamma\end{aligned} \tag{3.60}$$

. The uncertainty $\mathbf{B}$ has no influence in such PS detection, since it can be easily verified that $\tilde{\mathbf{s}}_\mathbf{3}^H\tilde{\mathbf{C}}_\mathbf{3}^{-1}\tilde{\mathbf{s}}_\mathbf{3} = \hat{\mathbf{s}}_\mathbf{3}^H\hat{\mathbf{C}}_\mathbf{3}^{-1}\hat{\mathbf{s}}_\mathbf{3}$, with $\hat{\mathbf{s}}_\mathbf{3}$ and $\hat{\mathbf{C}}_\mathbf{3}$ standing for the unambiguous estimates. This very property represents by all means a fundamental asset, since it leads to the consideration that

the PolPSCal technique is autonomous from any external reference information. As a results its performance is only dependent on the data consistency with the PS model.

It must be then remarked that the whole estimation chain (3.57)-(3.59) and (3.45) is coherent with respect to the LS optimization criterion, included the SVD step as previously commented, whereas the expression in (3.60), at the base of the PS selection, is intended to operate in a ML framework. Since the target signature and quality (covariance) estimators coincide with the ML ones and the $\tilde{\mathbf{H}}_\mathbf{3}$ retrieved are supposed to be close enough to the

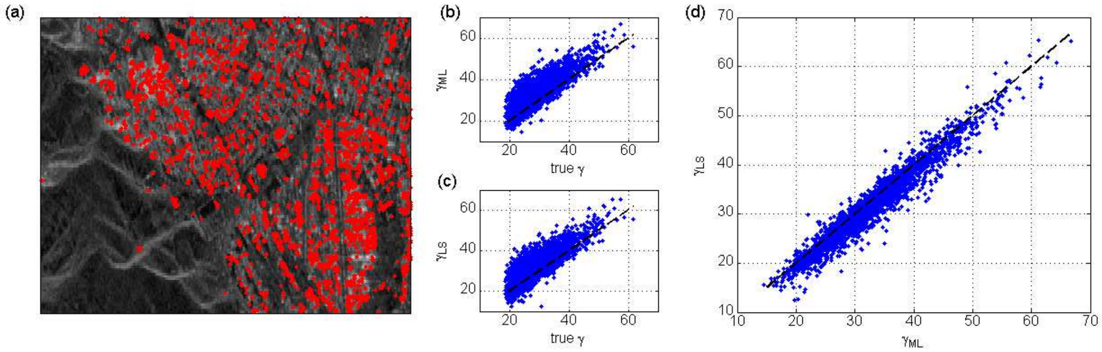

Figure 3.9: *Estimated Likelihood Ratio indicators on a pseudo-real stack of $N_I = 10$ images generated accordingly with the statistics of the detected PSs shown in (a). The deviations from the correct LR values registered by the estimates derived from the ML phases and the LS phases is shown respectively in the panel (b) and (c). The two different estimates are then directly compared in (d).*

ML optimum, the major issue in (3.60) is indeed the LS phase, and more specifically, its impact on (3.57)-(3.59). The robustness of $\hat{\gamma}_{LR}$ with respect to such improper handling has been evaluated on a representative synthetic dataset made of $N_I = 10$ images. The analysis, shown in Fig. 3.9, reports only minor deviations of the quality obtained with (3.59) from the one derived through the ML estimates. It can be therefore supposed that the adoption of (3.59) is not impairing the selection procedure.

The detection and estimations so far elucidated are repeated until a convergence on the estimates is reached. Note that because of the SVD step that jointly operates on the image and target parameters, the procedure is robust and therefore the convergence is fast, taking at most 3-4 cycles to adjust to the final estimates.

3.4.3 Normalization aided by external reference

With reference to the estimates returned by (3.49), it is evident that the ambiguity $\mathbf{B}$ must be removed from the PDM before calibrating the data or retrieving from the PDM the distortion parameters. The most obvious method to overcome such issue is that of making use of any available external information on the calibration parameters. The knowledge of the distortion matrix of a single image i_0 is indeed enough for the purpose. The problem as a result takes the form of a relative calibration problem, or, in other words, that of assessing the estimators accuracy not in an absolute sense but with respect to some other reference estimates.

Assuming that the matrix $\mathbf{H}_{i_0}^{ref}$ (and thus $\mathbf{H}_{\mathbf{3}i_0}^{ref}$) is known, and that the ambiguous estimate $\tilde{\mathbf{H}}_{\mathbf{3}i_0}$ is related to this latter through

$$\mathbf{H}_{\mathbf{3}i_0}^{ref} = \tilde{\mathbf{H}}_{\mathbf{3}i_0} \cdot \mathbf{B} + \mathbf{n}_H \tag{3.61}$$

where $\mathbf{n}_H$ is a generic noise (model errors and estimation uncertainties), the matrix $\mathbf{B}$ can be retrieved in the optimum LS sense as:

$$\hat{\mathbf{B}} = \left(\tilde{\mathbf{H}}_{\mathbf{3}i_0}^H \tilde{\mathbf{H}}_{\mathbf{3}i_0}\right)^{-1} \tilde{\mathbf{H}}_{\mathbf{3}i_0}^H \mathbf{H}_{\mathbf{3}i_0}^{ref}. \tag{3.62}$$

Once $\mathbf{B}$ is determined one can easily obtain the other PDM estimates through:

$$\hat{\mathbf{H}}_{\mathbf{3}i} = \tilde{\mathbf{H}}_{\mathbf{3}i} \cdot \hat{\mathbf{B}}. \tag{3.63}$$

Note that in a real calibration scenario the reference matrix $\mathbf{H}_{i_0}^{ref}$ is extracted either from internal calibration information or from external estimation techniques [15]. Besides, it should be considered that more normalization possibilities are offered by the multi-image dataset, such as the exploitation of more PDMs to name one, but also that the external information can be limited and thus an integration rather than a normalization would be required. Such scenario complexity will be treated in more detail in chapter 4.

3.5 Theoretical Performance

In appendix C it is shown that the ML refinement outperforms the LS estimates when the observation is consistent with the model in (3.1). It is also remarked that this is achieved at the expense of more computation burden for the system and that the stability still requires some proper assessment. Differently, the SVD solution represents a more effective and predictable approach even when the data has poor agreement with the model, and thus represents a preferable choice. Besides, a theoretical analysis on the estimation error attained by (3.45) is indeed feasible. Its approximated closed-form expression will be here derived as a function of the true distortion and target parameters.

The procedure is based on the LS estimators of the involved parameters. When the image distortion and the PS backscatter are treated separately, the LS optimum for the first is yielded through:

$$\begin{aligned}\hat{\mathbf{H}}_{\mathbf{3}i}^{(LS)} &= \underset{\mathbf{H}_{\mathbf{3}i}}{\operatorname{argmin}} \left(\sum_p \|\mathbf{z}_{i,p} - \mathbf{H}_{\mathbf{3}i}\mathbf{s}_{\mathbf{3}p}\|\right) \\ &= \underset{\mathbf{H}_{\mathbf{3}i}}{\operatorname{argmin}} \left(\sum_p \operatorname{Tr}\left[\left(\mathbf{z}_{i,p} - \mathbf{H}_{\mathbf{3}i}\mathbf{s}_{\mathbf{3}p}\right)\left(\mathbf{z}_{i,p} - \mathbf{H}_{\mathbf{3}i}\mathbf{s}_{\mathbf{3}p}\right)^H\right]\right) \\ &= \sum_p \mathbf{z}_{i,p}\mathbf{s}_{\mathbf{3}p}^H \cdot \left(\sum_p \mathbf{s}_{\mathbf{3}p}\mathbf{s}_{\mathbf{3}p}^H\right)^{-1}\end{aligned} \tag{3.64}$$

whereas the latter is simply obtained as:

$$\hat{\mathbf{s}}_{\mathbf{3}p}^{(LS)} = \left(\sum_i \mathbf{H}_{\mathbf{3}i}^H \mathbf{H}_{\mathbf{3}i}\right)^{-1} \sum_i \mathbf{H}_{\mathbf{3}i}^H \mathbf{z}_{i,p}. \tag{3.65}$$

It can be argued that in a real calibration scenario we do not have information neither on $\mathbf{H}_{\mathbf{3}i}$ nor on $\mathbf{s}_{\mathbf{3}p}$, but we can only rely on some generic estimates $\hat{\mathbf{H}}_{\mathbf{3}i}$ and $\hat{\mathbf{s}}_{\mathbf{3}p}$. A rigorous approach would at this point demand the repeated substitution of (3.65) in (3.64) and then that of (3.64) into (3.65) in order to yield the asymptotic expression of the estimates, i.e. the LS optimum. A simplified derivation, though, is here proposed. The approximated approach simply consists in accounting only for a single substitution step, which is the one carrying the largest error contribute. Equation (3.64) takes then the still comfortable expression:

$$\begin{aligned}
\hat{\mathbf{H}}_{\mathbf{3}n} &= \sum_p \mathbf{z}_{n,p}\hat{\mathbf{s}}_{\mathbf{3}p}^H \cdot \left(\sum_p \hat{\mathbf{s}}_{\mathbf{3}p}\hat{\mathbf{s}}_{\mathbf{3}p}^H\right)^{-1} \\
&= \sum_p \left(\mathbf{H}_{\mathbf{3}n}\mathbf{s}_{\mathbf{3}p} + \mathbf{e}_{i,p}\right)\hat{\mathbf{s}}_{\mathbf{3}p}^H \cdot \left(\sum_p \hat{\mathbf{s}}_{\mathbf{3}p}\hat{\mathbf{s}}_{\mathbf{3}p}^H\right)^{-1} \\
&\cong \mathbf{H}_{\mathbf{3}n}\left(1 - \mathbf{H}_{\mathbf{inv}}\sum_p\sum_i \mathbf{H}_{\mathbf{3}i}^H \mathbf{e}_{i,p}\mathbf{s}_{\mathbf{3}p}^H\mathbf{s}_{\mathbf{inv}}\right) + \sum_p \mathbf{e}_{n,p}\mathbf{s}_{\mathbf{3}p}^H\mathbf{s}_{\mathbf{inv}} \qquad (3.66)
\end{aligned}$$

where the assumption of high SCR allows to neglect all the second and higher order terms of noise $\mathbf{e}$. Besides, the following approximation and new nomenclature were adopted:

$$\mathbf{s}_{\mathbf{inv}} = \left(\sum_p \mathbf{s}_{\mathbf{3}p}\mathbf{s}_{\mathbf{3}p}^H\right)^{-1}, \qquad \mathbf{H}_{\mathbf{inv}} = \left(\sum_i \mathbf{H}_{\mathbf{3}i}^H\mathbf{H}_{\mathbf{3}i}\right)^{-1}$$

$$\left(\sum_p \hat{\mathbf{s}}_{\mathbf{3}p}\hat{\mathbf{s}}_{\mathbf{3}p}^H\right)^{-1} \cong \mathbf{s}_{\mathbf{inv}} - \mathbf{s}_{\mathbf{inv}} \cdot 2\mathcal{R}\left\{\sum_p \mathbf{s}_{\mathbf{3}p}\sum_i \mathbf{e}_{i,p}^H\mathbf{H}_{\mathbf{3}i} \cdot \mathbf{H}_{\mathbf{inv}}\right\}\mathbf{s}_{\mathbf{inv}} \tag{3.67}$$

The PDM expression in (3.66) is indeed unbiased, since the nature of the noise, see (3.13) and (3.14), is that of a zero-mean process. The expression of their covariance is attained as:

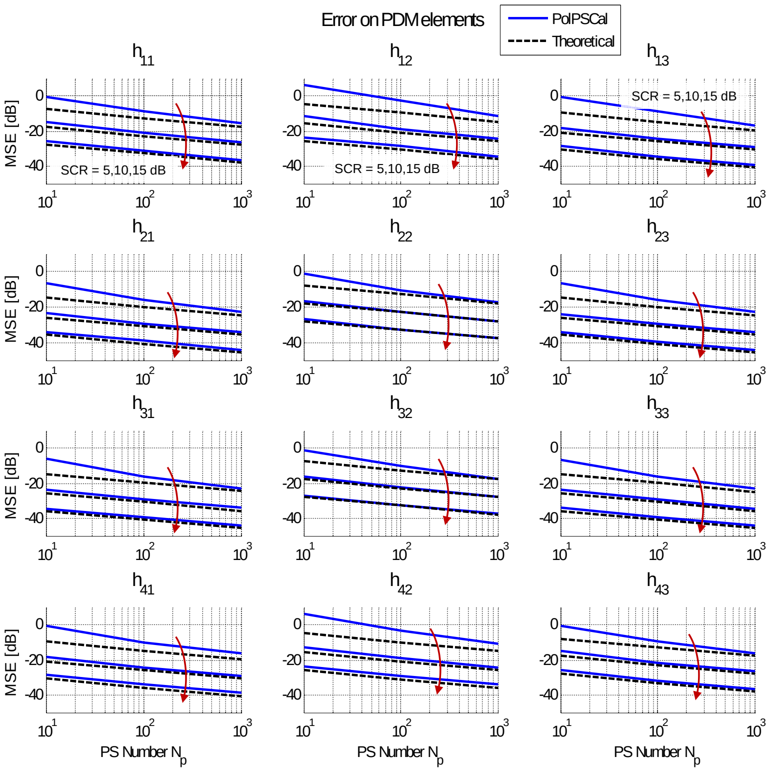

Figure 3.10: *PolPSCal performance evaluated through Montecarlo runs on synthetic PS datasets with SCR varied between 5 and 15 dB. The estimation performance is studied for every element of the 4×3 PDM as a function of the number of PS N_p in the stack and is compared with the closed-form approximated accuracy expression.*

$$\begin{aligned}
\mathbf{C}_n^{(LS)} &= E\left[\mathrm{vec}(\hat{\mathbf{H}}_{\mathbf{3}n} - \mathbf{H}_{\mathbf{3}n}) \cdot \mathrm{vec}(\hat{\mathbf{H}}_{\mathbf{3}n} - \mathbf{H}_{\mathbf{3}n})^H\right] \\
&= \kappa \left[\sum_p \sum_i \left(\mathbf{s}_{\mathbf{3}p}^* \otimes \mathbf{H}_{\mathbf{3}i}^H\right) \Gamma_{i,p} \left(\mathbf{s}_{\mathbf{3}p}^* \otimes \mathbf{H}_{\mathbf{3}i}^H\right)^H\right] \kappa^H + \\
&\qquad \sum_p \left(\mathbf{s}_{\mathbf{inv}}^T \mathbf{s}_{\mathbf{3}p}^* \otimes \mathbf{I}_4\right) \Gamma_{n,p} \left(\mathbf{s}_{\mathbf{inv}}^T \mathbf{s}_{\mathbf{3}p}^* \otimes \mathbf{I}_4\right)^H + \\
&\qquad 2\mathcal{R}\left\{\kappa \sum_p \left(\mathbf{s}_{\mathbf{3}p}^* \otimes \mathbf{H}_{\mathbf{3}n}^H\right) \Gamma_{n,p} \left(\mathbf{s}_{\mathbf{inv}}^T \mathbf{s}_{\mathbf{3}p}^* \otimes \mathbf{I}_4\right)^H\right\}
\end{aligned} \tag{3.68}$$

with * referring to the complex conjugate, $\kappa = \mathbf{s}_{\mathbf{inv}}^T \otimes (\mathbf{H}_{\mathbf{3}n} \mathbf{H}_{\mathbf{inv}})$ and $\Gamma_{i,p} = \mathbf{H}_{\mathbf{3}i} \mathbf{C}_{\mathbf{3}p} \mathbf{H}_{\mathbf{3}i}^H +$

$\nu_i \mathbf{I}_4$. The interpretation of (3.68) is not straightforward though it can be seen from the simulation results in Fig. 3.10 that such theoretical formulation is able to provide a close expectation of the SVD results (with only a little underestimation bias). It is readily inferred that when the the system is ideal, $\mathbf{H} = \mathbf{I}_4 \Rightarrow \mathbf{H_3} = \mathbf{P}$, and the clutter statistics are the same for all the PSs, the trace of (3.68), which expresses the total PDM uncertainty (Total Mean Squared Error), can be simplified into:

$$\text{TMSE} = \text{Tr}\left\{\mathbf{C}_n^{(LS)}\right\} = \left(\frac{1}{N_I} + 2\right) \cdot \text{Tr}\left\{\mathbf{s_{inv}}\right\} \left(\text{Tr}\left\{\Gamma\right\} - \sigma_n\right) + \text{Tr}\left\{\mathbf{s_{inv}}\right\} \text{Tr}\left\{\Gamma\right\}$$

The number of images is only barely influential on the estimation quality (it has an impact only when N_I is very low) whereas the disturbance added by thermal noise becomes significant when its power is close to the one of the target clutter. By coarsely assuming $\text{Tr}\left\{\mathbf{s_{inv}}\right\} \text{Tr}\left\{\Gamma\right\} \propto \left(N_p \cdot SCR_{av}\right)^{-1}$, with SCR_{av} being the average SCR, the relationship between the accuracies of the two different dataset configurations $\{SCR_1, N_{p_1}\} \rightarrow$ TMSE_1 and $\{SCR_1, N_{p_1}\} \rightarrow \text{TMSE}_2$ can be conveniently approximated to:

$$\Delta_{[\text{dB}]}\text{TMSE} \simeq -\Delta_{[\text{dB}]}\text{SCR} - 10\log_{10}\left(\frac{N_{p_2}}{N_{p_1}}\right). \tag{3.69}$$

where the notation $\Delta_{[\text{dB}]}x = x_2[\text{dB}] - x_1[\text{dB}]$ is introduced. Though (3.69) refers to the total error it can be noticed from Fig. 3.10 that the same trend is shared by all the PDM elements. Indeed, their MSE curves simply differ by a scalar factor, that depends on both the backscatter characteristics of the PSs and the specific distortion affecting the data.

So far the analysis has been focused on defining the estimation problem and evaluating the performance of the parameter estimators. The attention will be now shifted to the verification of the calibration quality, which is in the end the utmost interest for the majority of the SAR users. The overall quality is evaluated by adopting the MNE metric advised in (3.41), that is independent from the targets to calibrate. In very simple terms, an MNE level of -30 dB conveys that the maximum amount of relative distortion that a target can experience is indeed -30 dB. The curves plotted in Fig. 3.11 represent the MNE of a wide set of calibration scenarios, with number of PSs ranging from 200 to 1000 and SCR quality varying from 5 and 20 dB with steps of 5 dB. The interpretation is straightforward: for instance it can be deduced that in order to maintain a -30 dB MNE purity, the PolPSCal could identically use 7000 PSs with 5 dB SCR or 200 PSs with a 20 dB SCR quality. Note that the PDM distortion model has not been so far accounted, meaning that no model consistency was forced on the estimates. In other words, the calibration in (3.38) was chosen instead of the approach in (3.39), which will be discussed in the next chapter.

A further remark must be spent on the fact that the PolPSCal calibration performance achieved through (3.63) and (3.38) is invariant with respect to the polarimetric distortion

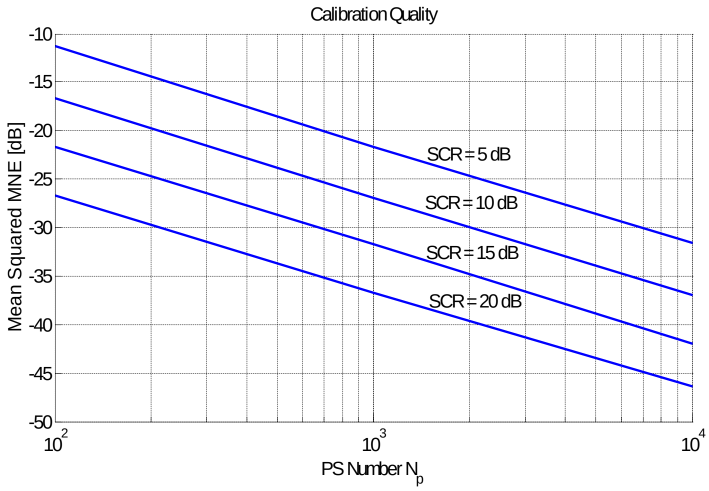

Figure 3.11: *Overall calibration quality achieved by the PolPSCal. The quality is evaluated through the MNE metric on synthetic datasets with SCR varied between 5 and 20 dB.*

diversity. This behavior is also inferred from Fig. 3.12, where the MNE attained for different perturbation amplitudes of the Faraday rotation disturbance is shown to have a constant trend.

3.6 Conclusions

The chapter debated an external calibration approach based on the stable natural targets, namely Permanent Scatterers (PS), that can be spotted in the illuminated frame. The method, hereby called PolPSCal, allows for relative calibration of the full 4 by 3 PDMs affecting the stack images. The algorithm is neither constrained to a particular PDM model (thus its implementation is practically feasible for any SAR sensor) nor to any external information. These latter are eventually demanded afterwards in order to normalize the returned PDM stack to an absolute reference. The approach is supported by the fundamental assumption that the distortion fluctuations have a large-scale spatial behavior. This allows indeed to approximate such parameters with constant values over small portions, called imagettes, of the total frame area, that are individually processed. A pixel-basel PS detection metric which allows to exploit to a larger extent the PS polarimetric time-series has been formulated. When the number of images is large the method significantly improves the detection performance with respect to the traditional amplitude based approaches even with unfavorable baseline configurations, i.e. when the clutter experiences only weak geometric decorrelation. A novel procedure was designed in order to handle the processing of the polarimetric PS data, achieving an LS estimation of the model parameters. The PolPSCal output accounts for the target phases, the PS polarimetric signatures and quality, and

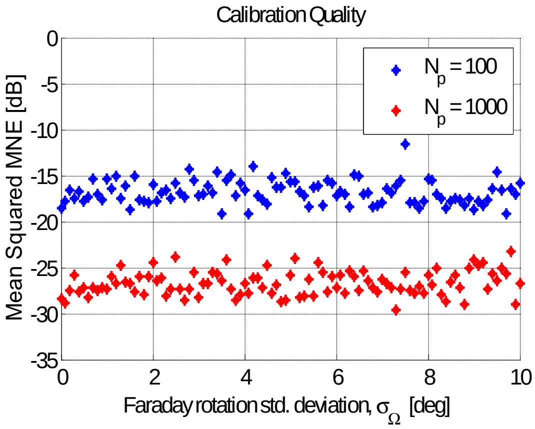

Figure 3.12: *PolPSCal calibration quality. The MNE dependence on the Faraday perturbation strength is reported for two different stack configurations with 100 and 1000 PSs respectively and the same SCR = 5 dB quality.*

last but not least the PDM information. At the end of the chapter it was shown how the theoretical calibration performance is in a first approximation related to the number of PS detected in the imagette and to their polarimetric quality and how it is instead independent from the distortion characteristics.

CHAPTER 4

Permanent Scatterers and Distributed Targets: an overarching system monitoring approach

It was discussed in chapter 2 how the estimation of the system distortion is hardly feasible when carried out solely on distributed targets (DT) without some proper model preconditioning. Chapter 3 addressed then the Permanent Scatterer (PS) based calibration problem, illustrating the performance but also remarking the need of disambiguating the estimates at the end of the process. The present chapter aims to provide a more encompassing view of the problem by focusing on the fact that the PS procedure provides different distortion information from that returned by the DTs and therefore carry the potential to unveil further distortion details. The perspective, however, can be easily reverted, thus looking at the estimation problem from the PS standpoint. In such case we should argue that the PDMs retrieved by the PolPSCal technique already carry the whole distortion information, though affected by a 3 by 3 matrix multiplication uncertainty, and that the DT-based estimates can help in removing the whole or just part of this uncertainty. The aim of this chapter is then two-fold: 1) propose the theoretical formalization of a calibration framework where the for DT-based techniques and the PolPSCal information are conveniently integrated for a joint polarimetric calibration 2) provide an effective validation through its application on a real case study. This latter has been carried out on a C-Band RADARSAT-2 dataset acquired over the Barcelona town area in the Fine Quad-Pol mode.

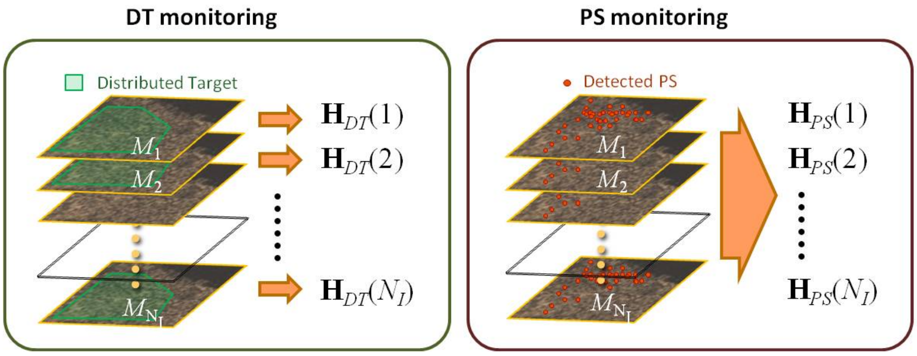

Figure 4.1: *Intuitive representation of a DT-based (left) and PS-based (right) estimation procedures. Whereas the DT-based estimates are obtained individually for each image the PS-based are the result of a joint stack estimation.*

4.1 Overview of the two-fold information framework

The DT-based techniques and the PolPSCal algorithm extract the distortion parameters from different categories of target information, more specifically from second-order statistics (covariance matrix) the first and from first-order information (amplitude and phase) the latter. Besides, DT estimation usually relies on areas of randomly oriented scatterers (orientation symmetry), whereas the PS estimates are computed from stable and strong scatterers. As a result of the independent DT-based and PolPSCal algorithm application to the data available, as illustrated in the scheme of Fig. 4.1, the two PDM (polarimetric distortion matrix) sets are attained:

$$\mathbf{H}_{PS}(i), \quad \mathbf{H}_{DT}(i) \quad \text{with } i = 1, 2 \cdots, N_I \tag{4.1}$$

for all the N_I images comprising the polarimetric image stack. This first, $\mathbf{H}_{PS}$, is indeed related to the true 4×3 PDM $\mathbf{H_3}$ by

$$\mathbf{H_3}(i) = \mathbf{H}(i) \cdot \mathbf{P} = e^{j\psi_{PS}(i)}\mathbf{H}_{PS}(i) \cdot \mathbf{B} + \mathbf{N}_{PS}(i) \tag{4.2}$$

where $\mathbf{P} = \begin{bmatrix} 1 & 0 & 0 \\ 0 & 1 & 0 \\ 0 & 1 & 0 \\ 0 & 0 & 1 \end{bmatrix}$ is a column-shrinking matrix, $\mathbf{N}_{PS}$ and $\mathbf{B}$ are the 4×3 and 3×3 complex matrices representing respectively the noise and the ambiguity matrix affecting the PolPSCal estimates, ψ_{PS} is a residual phase ambiguity between the PDM and the optical path of the targets. Notice that, whereas $e^{j\psi_{PS}}$ is image-dependent, $\mathbf{B}$ is constant throughout the stack. This is indeed the reason behind the separate modeling of their phases.

The second PDM estimate, $\mathbf{H}_{DT}$, is a model-based 4×4 matrix, $\mathbf{H}_{DT} \equiv \mathbf{H}(\hat{\Theta}_{DT})$, where $\hat{\Theta}_{DT}$ is a set of distortion parameters that can be estimated. The case of a generic polarimetric system, thus with no assumptions on the cross-talks and on Faraday, is hereby addressed. In this case, $\mathbf{H_3}$ would be related to the $\mathbf{H}_{DT}$ estimates through:

$$\mathbf{H_3} = Ae^{j\psi_{DT}} \cdot \mathbf{H}_{DT} \cdot \mathbf{P} \cdot \mathbf{K} + \mathbf{N}_{DT} \tag{4.3}$$

$$\mathbf{H_3} = Ae^{j\psi_{DT}} \cdot \begin{bmatrix} 1 & \alpha w & v & \alpha v w \\ u & \alpha & uv & \alpha v \\ z & \alpha w z & 1 & \alpha w \\ uz & \alpha z & u & \alpha \end{bmatrix} \begin{bmatrix} 1 & 0 & 0 \\ 0 & 1 & 0 \\ 0 & 1 & 0 \\ 0 & 0 & 1 \end{bmatrix} \begin{bmatrix} 1 & 0 & 0 \\ 0 & k & 0 \\ 0 & 0 & k^2 \end{bmatrix} + \mathbf{N}_{DT} \tag{4.4}$$

with:

$$Ae^{j\psi_{DT}} = r_{11}t_{11}, \quad k = \frac{t_{22}}{t_{11}}, \tag{4.5}$$

$$\alpha = \frac{r_{22}}{r_{11}}\frac{t_{11}}{t_{22}}, \quad u = \frac{r_{21}}{r_{11}}, \quad v = \frac{t_{21}}{t_{22}}, \quad w = \frac{r_{12}}{r_{22}}, \quad z = \frac{t_{12}}{t_{11}} \tag{4.6}$$

where $\mathbf{N}_{DT}$ is the estimates deviation from the true model and r_{ij},t_{pq} with $i, j, p, q = \{1, 2\}$ are respectively the complex elements of the 2×2 distortion matrices in reception and transmission belonging to the model discussed in chapter 3 and also reported schematically in Fig. 4.2. The set $\Theta_{DT} = \{\alpha, u, v, w, z\}$, comprising the imbalance ratio and the 4 cross-talk coefficients, represents the largest unambiguous parameter set attainable through DT estimation. The information about the total real gain A and the channel imbalance k would be still missing.

4.2 Distortion data assimilation: a theoretical strategy

4.2.1 PDM normalization

The idea herehence promoted for the assimilation of the two different information is that of performing the same procedure presented in 3.4.3, where some PDM information external to the PolPSCal is used to normalize the estimates of this latter. The external information is here represented by the DT-based distortion estimates $\mathbf{H}_{DT}$ of a chosen image i_0. The criterion adopted for the selection of i_0 is an image quality indicator that will be better discussed with relation to the Barcelona case study in 4.3.3. By merging the estimates (4.3) and (4.2) of the reference image i_0 we obtain the relationship:

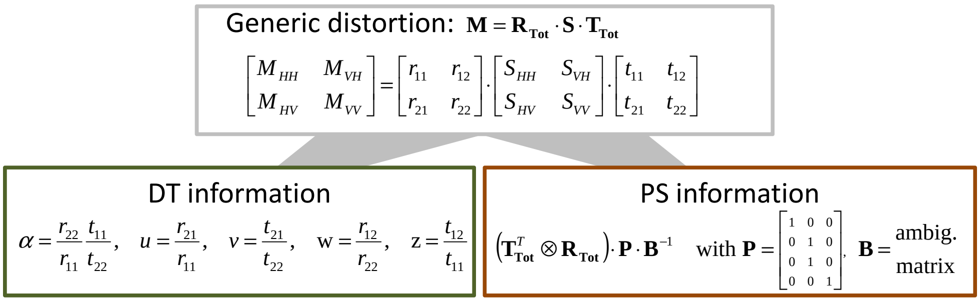

Figure 4.2: *Essential representation of the mathematical connection between the general distortion model of the observations and the information that can be extracted from the DT and PSs.*

$$A(i_0) \cdot \mathbf{H}_{DT}(i_0) \cdot \mathbf{P} \cdot \mathbf{K}(i_0) = e^{j\chi(i_0)} \mathbf{H}_{PS}(i_0) \cdot \mathbf{B} + \mathbf{N}(i_0) \tag{4.7}$$

where $\mathbf{N} = \mathbf{N}_{PS} - \mathbf{N}_{DT}$ is the overall noise term, $\chi = \psi_{PS} - \psi_{DT}$ and where the dependence on the image index has been explicited. The unknowns of the non-linear system are $A(i_0)$, k, that in (4.3) must be now referred to as $k(i_0)$, $\chi(i_0)$, and $\mathbf{B}$, therefore 2 real (A and χ) and 10 complex coefficients (f_2 and the 9 elements of $\mathbf{B}$), amounting to 22 real unknowns. On the other side, the number of real equations is 24. However, retrieving at the same time A, χ, k and $\mathbf{B}$ is not possible. This is trivially verified by observing that for arbitrary values of (α,β,γ) the two sets

$$\Psi = \left\{A, \chi, f_2, \mathbf{B}\right\}, \qquad \Psi' = \left\{ \alpha A, \beta\chi, \gamma f_2, e^{-j\beta\chi}\mathbf{B} \cdot \begin{bmatrix} 1/\alpha & & \\ & 1/(\alpha\gamma) & \\ & & 1/(\alpha\gamma^2) \end{bmatrix} \right\}$$

are both valid solutions of (4.7). Such ambiguity is practically handled by constraining the parameters to the arbitrary values:

$$\begin{aligned} A(i_0) &= 1 \\ \phi(i_0) &= 0 \\ f_2(i_0) &= 1 \end{aligned} \tag{4.8}$$

thus yielding:

$$\mathbf{H}_{DT}(i_0) \cdot \mathbf{P} = \mathbf{H}_{PS}(i_0) \cdot \mathbf{B} + \mathbf{n}(i_0) \tag{4.9}$$

with $\mathbf{K}(i_0)$ that becomes the identity matrix $\mathbf{I}_3$ as a result.

By looking further into the algebraic problem of (4.9) it can be observed that the matrices $\mathbf{H}_{DT}$, $\mathbf{H}_{PS}$ and $\mathbf{B}$ do not suffer from rank deficiencies and thus are all invertible or pseudo-invertible. It is then possible to proceed to the PDM normalization by first estimating from (4.9) the ambiguity matrix, $\hat{\mathbf{B}}$, as:

$$\hat{\mathbf{B}} = \mathbf{H}_{PS}(i_0)^{\dagger}\mathbf{H}_{DT}(i_0) \cdot \mathbf{P} \tag{4.10}$$

and than trivially applying $\hat{\mathbf{B}}$ to the other images i of the stack:

$$\hat{\mathbf{H}}_{\mathbf{3}}(i) = \mathbf{H}_{PS}(i) \cdot \hat{\mathbf{B}} \tag{4.11}$$

with † standing for the pseudo-inverse operator. Notice that the noise was neglected in the derivation of (4.11), though its optimal handling could indeed bring marginal improvements in the estimates quality. It was in fact decided to leave such topic open for future investigation.

4.2.2 System monitoring and Data calibration

As a result of the constraints in (4.8), the relationship between the retrieved ambiguity $\hat{\mathbf{B}}$ and the real one $\mathbf{B}$ can be well approximated (under the assumption of small estimation noise $\mathbf{N}$) by unwinding (4.10) into:

$$\hat{\mathbf{B}} \simeq \frac{e^{j\chi(i_0)}}{A(i_0)} \cdot \mathbf{B}^{-1} \cdot \mathbf{K}(i_0)^{-1}. \tag{4.12}$$

It follows that the normalized PDM of a generic image i computed through (4.11) can be though of as:

$$\hat{\mathbf{H}}_{\mathbf{3}}(i) \simeq \frac{1}{A(i_0)} \cdot e^{j(\chi(i_0)-\psi_{PS}(i))} \cdot \mathbf{H}_{\mathbf{3}}(i) \cdot \mathbf{K}(i_0)^{-1} \tag{4.13}$$

or, more explicitly:

$$\hat{\mathbf{H}}_{\mathbf{3}}(i) \simeq r_A(i) \cdot r_\chi(i) \cdot \begin{bmatrix} 1 & \alpha_i w_i & v_i & \alpha_i v_i w_i \\ u_i & \alpha_i & uv & \alpha_i v_i \\ z_i & \alpha_i w_i z_i & 1 & \alpha_i w_i \\ u_i z_i & \alpha_i z_i & u_i & \alpha_i \end{bmatrix} \begin{bmatrix} 1 & 0 & 0 \\ 0 & 1 & 0 \\ 0 & 1 & 0 \\ 0 & 0 & 1 \end{bmatrix} \begin{bmatrix} 1 & 0 & 0 \\ 0 & r_k(i) & 0 \\ 0 & 0 & r_k(i)^2 \end{bmatrix}. \tag{4.14}$$

$$r_A(i) = \frac{A(i)}{A(i_0)}, \quad r_k(i) = \frac{k(i)}{k(i_0)}, \quad r_\chi(i) = \frac{e^{j\chi(i_0)}}{e^{j\chi(i)}} \tag{4.15}$$

The assimilation procedure allows then to yield an unambiguous estimation of the enlarged set:

$$\Theta_{PS} = \{r_A,\ r_k,\ r_\chi,\ \alpha,\ u,\ v,\ w,\ z\} \tag{4.16}$$

that, compared to Θ_{DT} set in (4.6), also accounts for the absolute gain and channel imbalance ratios (total imbalance indeed, comprising eventual Faraday effects) with respect to their values at time i_0. The determination of Θ_{PS} from the normalized estimates $\hat{\mathbf{H}}_\mathbf{3}$ is indeed a non linear problem. A convenient solution is that of resorting to the following optimization criterion:

$$\hat{\Theta}_{PS} = \underset{\Theta_{PS}}{\operatorname{argmin}} \left\| \mathbf{W}_\mathbf{H}^{-1/2} \cdot vect\left(\hat{\mathbf{H}}_\mathbf{3} - \mathbf{H}_\mathbf{3}(\Theta_{PS})\right) \right\| \tag{4.17}$$

which reads as the minimization of the ℓ_2 norm between the vector assembled from $\hat{\mathbf{H}}_\mathbf{3}$ and the one reconstructed from the optimum set $\hat{\Theta}_{PS} = \{\hat{r}_A, \hat{r}_k, \hat{r}_\chi, \hat{\alpha}, \hat{u}, \hat{v}, \hat{w}, \hat{z}\}$ with their elements being weighted by the matrix $\mathbf{W}_\mathbf{H}$. This latter is conveniently determined as the correlation matrix of the error on the $\mathbf{H}_\mathbf{3}$ estimates, given the specific PS set under analysis, and is practically computed through the approximated analytical expressions in (3.68), which make use of the estimates $\hat{\mathbf{H}}_\mathbf{3}, \hat{\mathbf{s}}_\mathbf{3}, \hat{\mathbf{C}}_\mathbf{3}$ attained after normalization. The optimum for (4.17) is then found by means of an iterative procedure starting from the initial set $\hat{\boldsymbol{\Theta}}_{PS}^{(0)}$

$$\hat{\boldsymbol{\Theta}}_{PS}^{(0)} = \left\{ r_A = 1,\ r_k = 1,\ r_\chi = 0,\ \hat{\boldsymbol{\Theta}}_{DT} \right\} \tag{4.18}$$

It's been stated that the retrieval of $\mathbf{W}_\mathbf{H}$ is stack-adaptive, since different weights are found for different sets of PSs. The error correlation is indeed dependent on the particular PS polarimetric diversity, on the PS noise covariances, and on the actual distortion parameters. Among these latter, the Faraday rotation is the parameter exhibiting the most influence. In Fig. 4.3 the error variance on the single h_{mn} elements, normalized to the error power on the whole $\mathbf{H}_\mathbf{3}$, is shown as a function of Faraday for a representative PS scenario with SCR = 10 dB on every channel and an overall difference of 5 dB in the PS backscatter between the co-pol and the cross-pol channels. Though the cross-correlation terms are not shown, it should be remarked that they often are significant, and therefore cannot be neglected in the weighting operation.

The calibrated signature of the p-th target in the i-th image

$$\mathbf{x}(p,i) = [\ x_{HH}(p,i) \quad x_{HV}(p,i) \quad x_{VV}(p,i)\ ]^T \tag{4.19}$$

can be obtained from the its distorted vector

$$\tilde{\mathbf{M}}(p,i) = [\ M_{HH}(p,i) \quad M_{HV}(p,i) \quad M_{VH}(p,i) \quad M_{VV}(p,i)\ ]^T \tag{4.20}$$

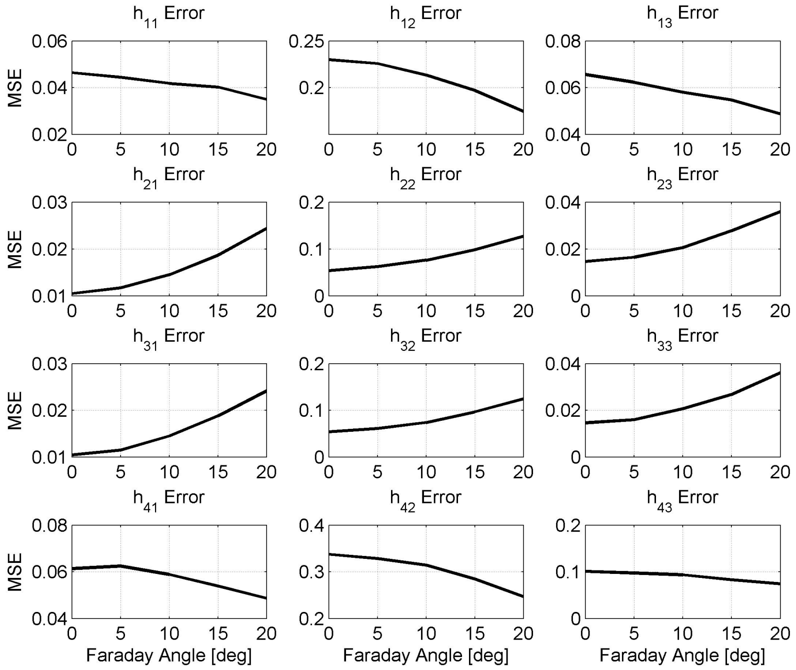

Figure 4.3: *Behavior of the residual errors for each element h_{mn} belonging to reconstructed $\hat{\mathbf{H}}_\mathbf{3}$, with respect to the Faraday rotation affecting the acquisition.*

by means of the least squares solution [38]:

$$\mathbf{x}(p,i) = \hat{\mathbf{H}}_\mathbf{3}(i)^\dagger \tilde{\mathbf{M}}(p,i) \tag{4.21}$$

where a data symmetrization ($x_{HV} = x_{VH}$) operation has implicitly been carried out. The calibrated data would be then related to their true value, $\mathbf{s}(p,i) = \begin{bmatrix} S_{HH}(p,i) & S_{HV}(p,i) & S_{VV}(p,i) \end{bmatrix}^T$, by:

$$\begin{aligned} x_{HH}(p,i) &= A(i_0) \cdot e^{j(\chi(i)-\chi(i_0))} \cdot S_{HH}(p,i) \\ x_{HV}(p,i) &= A(i_0) \cdot k(i_0) \cdot e^{j(\chi(i)-\chi(i_0))} \cdot S_{HV}(p,i) \\ x_{VV}(p,i) &= A(i_0) \cdot k(i_0)^2 \cdot e^{j(\chi(i)-\chi(i_0))} \cdot S_{VV}(p,i) \end{aligned} \tag{4.22}$$

where, apart from the common phase term that is irrelevant for data interpretation, a complex factor different for each polarization still hinders the absolute data calibration. It

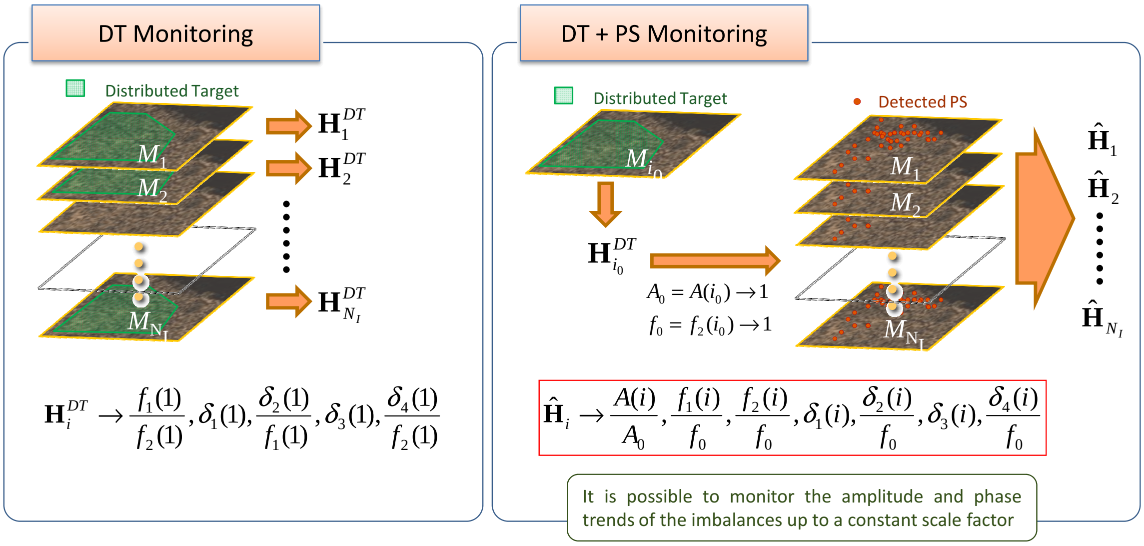

Figure 4.4: *Schematic representation of DT-based monitoring (left) and of the joint DT+PS strategy (right) that is able to extract from the scene all the information needed for a temporally comprehensive monitoring of the system distortion (up to a constant scale factor).*

must be positively remarked, though, that such factors are now constant along the stack. This means that, as a result of (4.8), a relative calibration with respect to the true data in i_0 was independently achieved for each polarization. This entails the possibility of applying intra-stack operations, such as change detection analysis, but still hampers direct inter-stack data comparison unless additional external information on the A and k at time i_0 is available. In particular, $k(i_0)$ contributes to the correct polarimetric interpretation of the scene and thus its information is essential for simple polarimetric analysis, such as the co-pol $HH - VV$ phase analysis, as well as for advanced polarimetric concepts such as polarimetric decompositions. The gain $A(i_0)$ is then required for amplitude-based parameter estimation, such as accurate soil moisture or biomass retrieval routines. This information must be necessarily determined by means of calibrated point targets observed at some time close to the i_0 UTC and for the same beam mode and elevation look angle.

4.2.3 Monitoring of Faraday-free systems

The benefits brought by the possibility of enlarging Θ_{DT} to Θ_{PS} become straightforward when the stack is not affected by Faraday rotations. This is indeed the case of airborne systems [1,38], of high frequency spaceborne sensors (from C-band upwards) and of lower frequency spaceborne systems (future L-Band and P-Band missions) operating in mild ionospheric conditions, i.e. typically at low latitudes during the night and/or in periods with lower sun activity [42]. We indeed recollect from chapter 2 that in such configurations the parameters in (4.16) are directly related to the TRM system distortion, and thus assume the more familiar expressions:

$$\begin{aligned} r_k(i) &\rightarrow \frac{f_2(i)}{f_2(i_0)} \\ \alpha(i) &\rightarrow \frac{f_1(i)}{f_2(i)} \\ u(i) &\rightarrow \delta_1(i) \\ v(i) &\rightarrow \frac{\delta_4(i)}{f_2(i)} \\ w(i) &\rightarrow \frac{\delta_2(i)}{f_1(i)} \\ z(i) &\rightarrow \delta_3(i) \end{aligned} \tag{4.23}$$

Notice that by manipulating the v and w cross-talks as:

$$\begin{aligned} r_k(i)v(i) &\rightarrow \frac{\delta_4(i)}{f_2(i_0)} \\ r_k(i)\alpha(i)w(i) &\rightarrow \frac{\delta_2(i)}{f_2(i_0)} \end{aligned} \tag{4.24}$$

we can obtain the equivalent set

$$\Theta_{PS} = \left\{ r_A(i),\ r_\chi(i),\ \frac{f_2(i)}{f_2(i_0)},\ \frac{f_1(i)}{f_2(i)},\ \delta_1(i),\ \frac{\delta_2(i)}{f_2(i_0)},\ \delta_3(i),\ \frac{\delta_4(i)}{f_2(i_0)} \right\} \tag{4.25}$$

that can be unambiguously retrieved from $\hat{\mathbf{H}}_3$ through (4.17). This implies that the temporal evolution of every system internal parameter (gain, imbalances and cross-talks) can be monitored during the whole mission life, and indeed represents the key point of the whole assimilation procedure, as also conveyed in Fig. 4.4. Such approach is aimed to bridge the gap between the lack of timely monitoring when using only DT methods and the expensive deployment and maintenance of calibrated point targets needed to ensure such information.

4.3 Assessment on the Radarsat-2 Barcelona dataset

4.3.1 Dataset overview

The monitoring capabilities so far discussed have been assessed on a Radarsat-2 dataset comprising a total of 26 images acquired over the time span of 3 years, with minimum revisit time of 24 days (Radarsat-2 revisit interval). More specifically, 9 images were collected in 2008 and the other 17 in 2010-2011. The beam mode is the Fine Quad mode with elevation look angle of 25°, which reports an effective ground range resolution of approximately 11 m. More technical details about the dataset and the sensor configuration are listed in Table 4.1 and Table 4.2, whereas in Fig. 4.5 it is possible to appreciate in more detail the differential baselines and the information on the Doppler Centroids. Notice in particular that the acquisitions span a baseline smaller than 1 km, with a deviation of 180 m, i.e. an orbit tube significantly narrower than the 2.5 km critical baseline of the Radarsat-2 mode. The SLC images are supposed to be finely coregistered: this is indeed possible even without polarimetric calibration, unless the distortion is too intense (for instance very large Faraday rotation residuals, which is not our case though).

The illuminated frame comprises a variety of scattering mechanisms, with the sea on the near range, a wide and mostly flat inhabited area in the middle range and a forested sloped area together with a few other inhabited grounds in the far range. For a visual representation of the frame area the reader is referred to the optical and Pauli colorcoded image shown in Fig. 2.14 as well as to the graphical indication of the different area typologies provided in Fig. 2.17.

Site		Barcelona (ES)
Campaign		SOAR-EU
System		Radarsat-2
# images		26
Mode		Fine Quad (FQ9)
Polarizations		HH,HV,VH,VV
Frequency	Ghz	5.405
Look Angle	deg	25
Res: sl.rg. ×az	m	5.2×7.6
Time span	yr	3
Baseline span	m	780
Baseline std	m	183
DC span	Hz	140
DC std	Hz	32

Table 4.1: *SAR Sensor and Dataset Parameters*

Image Dates - All collected at 06:00 AM (Descending)	
12-Apr-2008	13-Feb-2010
06-May-2008	02-Apr-2010
30-May-2008	26-Apr-2010
23-Jun-2008	20-May-2010
17-Jul-2008	13-Jun-2010
10-Aug-2008	07-Jul-2010
29-Sep-2008	31-Jul-2010
21-Oct-2008	24-Aug-2010
14-Nov-2008	11-Oct-2010
08-Dec-2008	04-Nov-2010
	28-Nov-2010
	22-Dec-2010
	15-Jan-2011
	08-Feb-2011
	04-Mar-2011
	28-Mar-2011

Table 4.2: *Acquisition dates of the Barcellona dataset*

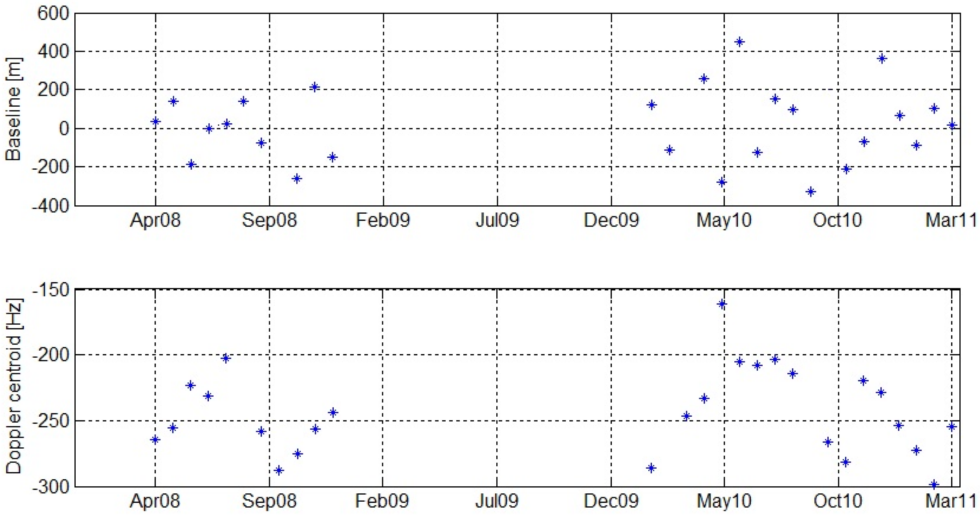

Figure 4.5: *Normal baselines (top) and Doppler rate estimates (bottom) of the 29 images belonging to the Radarsat-2 dataset used for the analysis.*

4.3.2 Assessment methodology

The effectiveness of the calibration would be exhaustively expressed by its absolute accuracy, i.e. a quantitative evaluation of the errors affecting the distortion estimates with respect to the true distortion values. Trivially, such assessment is possible when the latter values are known, which, however, is not our case, since no reference information could be collected and employed for absolute validation. Thus, instead of accuracy, we initially focused on assessing a secondary behavior: the stability. The consequence is that eventual biases in the estimates cannot be verified (herehence the "secondary" attribute), though very insightful information on the technique's robustness (fluctuations of the estimates) is obtained. The stability of the PolPSCal technique will be tested with respect to both different algorithm parameters ξ_n and independent sets of PSs $\chi_i = \{PS_i\}$. More formally, let $\hat{\Theta}(\xi_n, \chi_i)$ or simply $\hat{\Theta}_{n,i}$ be the estimate set of distortion parameters as a function of the algorithm settings and the PS group and define the estimation error as:

$$\varepsilon_{n,i} = \hat{\Theta}_{n,i} - \Theta \tag{4.26}$$

The accuracy is quantified by its MSE, which contains both the bias Δ_ε and the fluctuating part δ_ε:

$$MSE_{n,i} = E\left[\varepsilon_{n,i}^2\right] = E[(\overbrace{\hat{\Theta}_{n,i} - \mu}^{\delta_\varepsilon} + \overbrace{\mu - \Theta}^{\Delta_\varepsilon})^2] = E\left[\delta_\varepsilon^2\right] + \Delta_\varepsilon^2 = \nu_\varepsilon + \Delta_\varepsilon^2 \tag{4.27}$$

where μ is indeed $\mu_{n,i} = E\left[\hat{\Theta}_{n,i}\right]$, the fluctuation δ_ε is zero-mean with variance ν_ε and the expectation operator is supposed to be evaluated on different distortion realizations. The latter term in 4.27, Δ_ε, is not retrievable unless a-priori information on the image distortion is available. The term ν_ε, representing the stability, is instead attainable by averaging on the χ_i, thus $E\left[.\right] \to \langle . \rangle_i$, rather than averaging different distortion realizations (a challenging task indeed given the limited 29 images dataset). Such operation relies on the reasonable hypotheses:

- The Π_i overall quality is similar, so that $E\left[\nu_\varepsilon(i_1)^2\right] = E\left[\nu_\varepsilon(i_2)^2\right]$
- The distortion is the same for all Π_i
- The stability $E\left[\nu_\varepsilon^2\right]$ is not dependent on the specific distortion, i.e. $E\left[\nu_\varepsilon(\Theta_1)^2\right] = E\left[\nu_\varepsilon(\Theta_2)^2\right]$

The procedure leads then to the metric MSE_n, that is dependent only on the algorithm configuration adopted. The metric will be used to assess the performance of our inversion technique with respect to the distortion set (4.16) and to compare the results so achieved with the reference calibration technique proposed in [38] by Quegan. Remember that this latter can only handle the retrieval of (4.6).

4.3.3 Normalization Strategy

As previously discussed, when no reference data is available the normalization information demanded by the PolPSCal is indeed provided by the DT-based estimate $\hat{\mathbf{H}}_{DT}$ for a reference image i_0. A wise selection of the DT areas is indeed fundamental in order to yield consistent calibration results. This is in particular true with respect to the reflection symmetry property

$$\langle S_{HH} \cdot S_{HV}^{*} \rangle = \langle S_{HH} \cdot S_{HV}^{*} \rangle = 0$$

of the scatterer model. We could immediately identify two sloped vegetated areas behind the town. It is indeed reasonable to assume at C-Band slope effects do not impact significantly [26] on the reflection symmetry and that their area extension ($1.5 \cdot 10^6$ pixels) is large enough to provide only a bias < 20 dB on the data cross-covariance elements. A third smaller ($3.3 \cdot 10^5$ pixels) and flatter area composed by cultivated fields could also be located between the inhabited and the mountain strips.

The masks of the 3 areas superposed to the image frame is provided by Fig. 4.6, alongside of the attained Quegan estimates averaged throughout the dataset. The results agree to the fact that only a subtle (<0.1 dB) channel imbalance ratio (HV/VH) is measured and on the cross-talk level that registered surprisingly low values (< -40 dB), apparently confirming that the area selection was successful and the the RS2 instrument is finely calibrated [28].

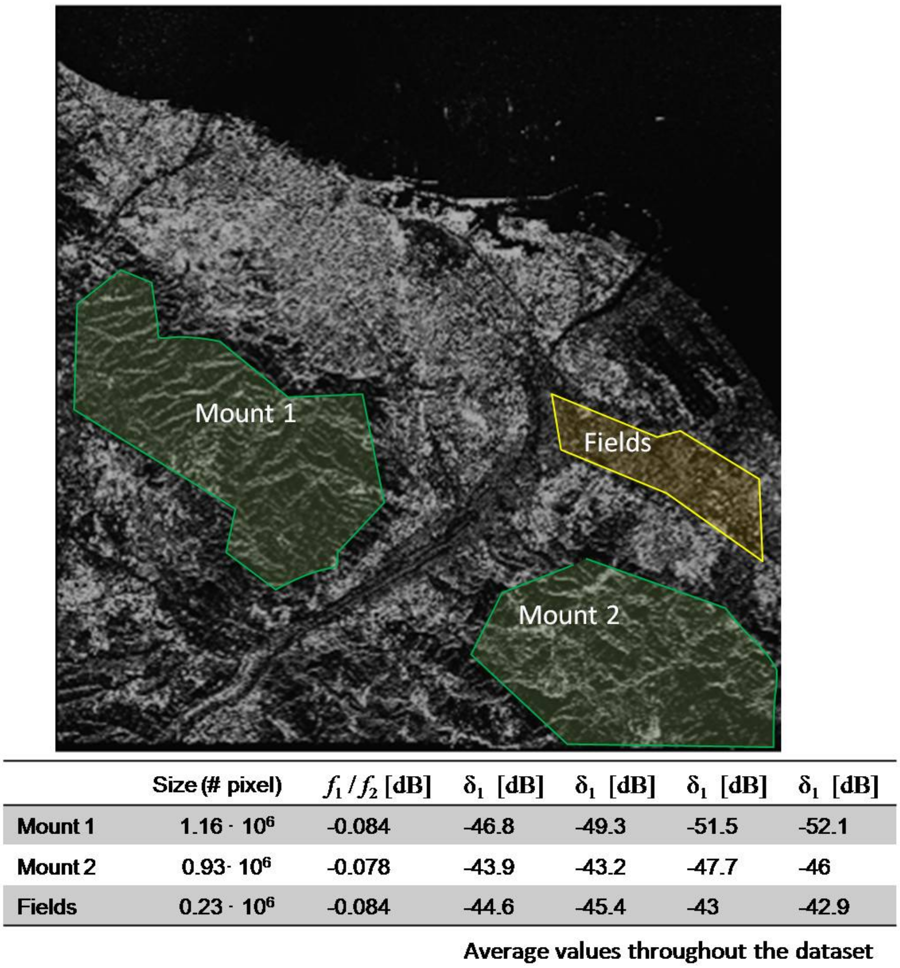

	Size (# pixel)	f_1 / f_2 [dB]	δ_1 [dB]	δ_1 [dB]	δ_1 [dB]	δ_1 [dB]
Mount 1	$1.16 \cdot 10^6$	-0.084	-46.8	-49.3	-51.5	-52.1
Mount 2	$0.93 \cdot 10^6$	-0.078	-43.9	-43.2	-47.7	-46
Fields	$0.23 \cdot 10^6$	-0.084	-44.6	-45.4	-43	-42.9

Average values throughout the dataset

Figure 4.6: *View of the three areas (top) used for the DT-based Quegan calibration algorithm. Schematic results (bottom) of the average values achieved for all the distortion parameters returned by the algorithm.*

For each PolPSCal configuration set ξ_n, the PDM normalization is performed on the image i_0 registering the best overall quality over all the imagettes (blocks). With "quality" we refer to the consistency of the PS-model with the SLC data. For the generic image i, the quality Q_i is defined as the total power of the residual between the measured data and the one reconstructed from the PolPSCal estimates normalized by the total data power. In formula:

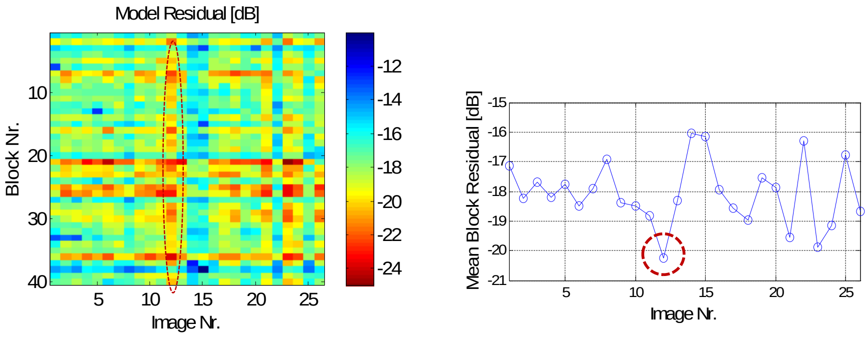

Figure 4.7: *Processing steps aimed to the selection of the PDM candidate for PDM normalization (ambiguity removal). (left) 2D representation of the block-image quality. (right) The image with minimum residual model error averaged over all the imagettes (blocks) is the best candidate.*

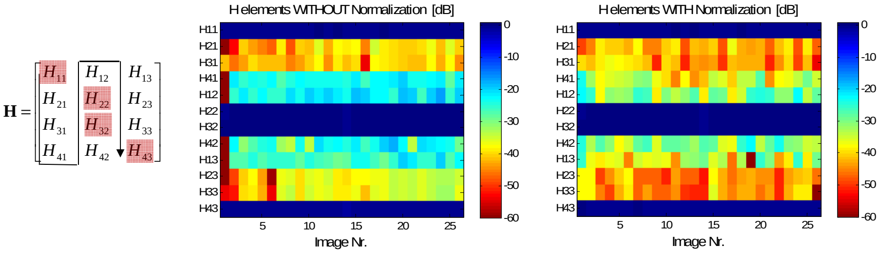

Figure 4.8: *Effects of PolPSCal normalization on the PDM element estimates. (left) PDM elements (arranged columnwise in the panels) trend along the stack (panel rows) without normalization. (right) PDM elements trend with normalization.*

$$Q_i = \frac{\sum_{p=1}^{N_p} \left\| \mathbf{y}(i,p) - e^{j\hat{\phi}(i,p)} \hat{\mathbf{H}}_{\mathbf{3}}(i) \hat{\mathbf{s}}(p) \right\|^2}{\sum_{p=1}^{N_p} \left\| \mathbf{y}(i,p) \right\|^2} \tag{4.28}$$

where $\hat{\mathbf{H}}_{\mathbf{3}}, \hat{\phi}, \hat{\mathbf{s}}$ are the PDM and target phase and signature estimates respectively and $\mathbf{y}$ are the polarimetric observations. The idea is also illustrated in Fig. 4.7; the residual of all the imagettes (along the columns) is averaged in order to evaluate the best image to use for normalization. It can be noticed that for the specific configuration reported the best quality results are attained for $i_0 = 12$. The effects of the normalization when the imagette quality is high (the SCR or the number N_p of the PSs is high) are evident, as conveyed by the estimated PDM elements in Fig. 4.8. Its correct application indeed has a great impact on the sensitivity that can be delivered by PolPSCal on the cross-talk estimates.

4.3.4 Discussion on the results

In accordance with the methodology discussed in section 4.3.2, only the the PolPSCal stability could be assessed from real data, i.e. the fluctuating ν_ε component of the MSE in (4.27). A few PolPSCal settings were tested:

- 2 different PS quality settings, associated to 2 different threshold settings T_γ. Since the GLR metric is a rather uncommon descriptor of the target quality, in a first approximation the reader can think that the first configuration accepts PS with SCR > 8 dB, while the second raises the bar to SCR > 12 dB.
- 4 different imagette sizes, regulated by the maximum number of accepted PSs N_p per imagette. The configurations tested vary from 500 PSs to 5000 PSs.

The statistical results are presented in both a compact representation where a single deviation value is given for each configuration and in a more visually-appealing representation of the image-series dispersion for the two opposite PolPSCal configurations (the best and the worst). The compact statistics are intuitively computed by averaging stack(image)-wise and block(imagette)-wise the variances registered by each imagette. Such results are shown in Fig. 4.9 and Fig. 4.10 for the amplitude and phase of the image gain and channel imbalances. Note that, whereas with traditional DT-calibration (Quegan) only the imbalance ratio can be monitored, the contribute of the PS information allows to distinguish between the two different imbalance fluctuations. On the quantitative standpoint, the amplitude stability is better than 0.3 dB (3σ) for the image gain, which is the least stable parameter. Channel imbalances and especially their ratio are in fact clipped under the 0.1 dB deviation.

Some preliminary δ_1, δ_2 cross-talk image-series results are then shown in Fig. 4.11, where it can be noticed that the good quality configuration is capable of delivering amplitude estimates below the -40 dB level, thus being on-par with the Quegan estimators. To this regard, it must be remarked that when a solid external information, such as the presence of accurate point target calibrators, is missing, the accuracy of the cross-talks estimates is necessarily related to that of the Quegan technique and thus to the quality of the DT in the scene, since a coarse normalization generates some serious PDM inter-element interference. So far, in fact, we cannot be sure if what we are measuring is true uncompensated cross-talk amplitude, or we are just dealing with a processing artifact. In the latter case we would however be happy enough to register that such noise floor is below -40 dB, and that as a natural consequence any distortion above such level should be correctly detected.

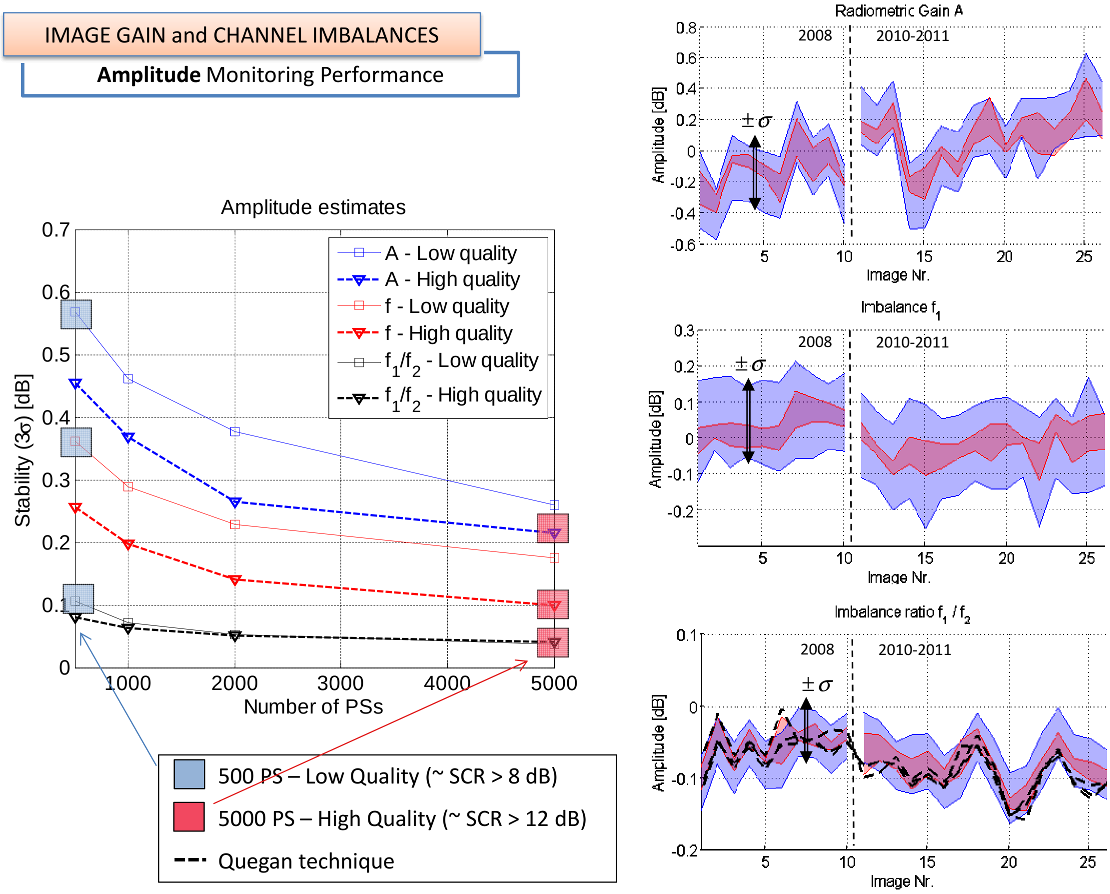

Figure 4.9: *Radiometric monitoring performance. (left) Compact representation (averaged image-wise) of the amplitude stability (3σ) estimates registered by a wide set of PolPSCal run configurations. (right) Expanded image-series results (average value and dispersion can be inferred from the colored band representation) for two specific configurations: a poor quality imagette configuration (blue), and a high quality one (red). Quegan results are limited to the imbalance ratio and are reported through black dashed lines for the three different DT areas.*

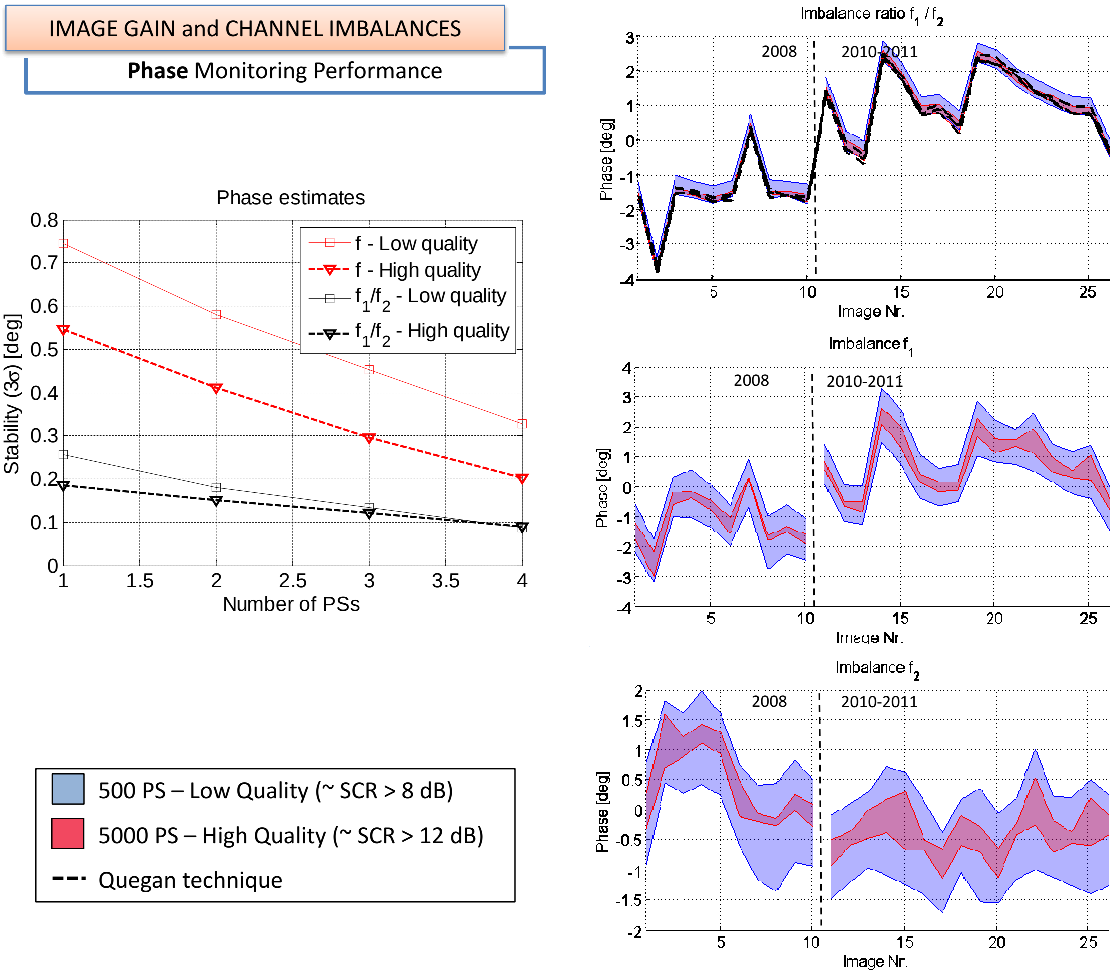

Figure 4.10: *Phase monitoring performance. (right) Compact representation (averaged image-wise) of the phase stability (3σ) estimates registered by a wide set of PolPSCal run configurations. (left) Expanded image-series results achieved by poor quality (blue) and high quality (red) imagettes estimates.*

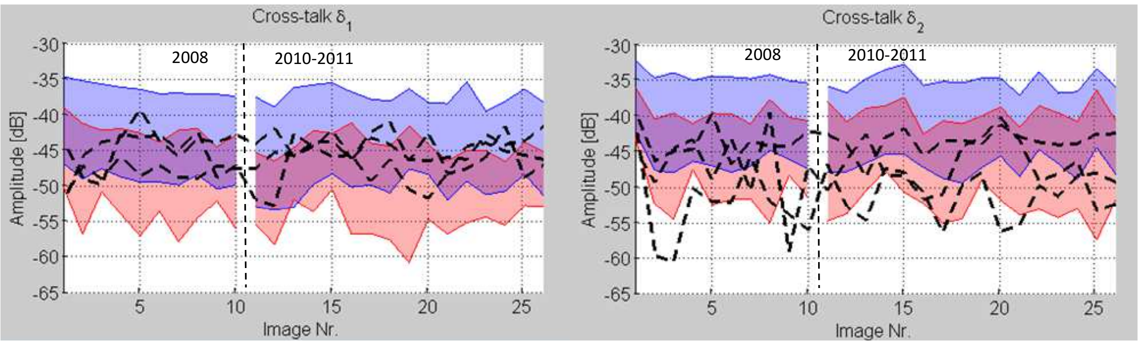

Figure 4.11: *Cross-talk amplitude performance. Expanded image-series of the dispersion results achieved on the two cross-talks* δ_1*(left) and* δ_2/f_1*(right) by processing poor quality (blue) and high quality (red) imagette sets. This represents indeed a hard test for PolPSCal since the number and quality of PSs should provide a stability at least comparable to the RS2 CT isolation (< - 40 dB) to be considered effective.*

CHAPTER 5

Conclusions

So far, the calibration of full-polarimetric SAR systems mostly relies on ground installations of calibrated active (transponders) or passive (corner reflectors) targets. It is although evident that part of the system health information can also be retrieved from other natural features which are intrinsic to the illuminated scene. The main research question that is addressed in this thesis is how the scene information must be collected and processed in order to produce an effective contribution to the polarimetric system monitoring and data calibration. Two main conceptual categories of in-scene information processing can be identified:

1. the model extraction from the scatterer **spatial** statistics
2. retrieval of coherent information from **temporal** target observation series

The two approaches apply to different target typologies: the first exploits distributed target (DT) area, the second relies on stable mechanisms, the so-called Permanent Scatterers (PS). In the first case, not any DT area would suit the calibration needs, but only the ones providing additional constraints to the model: the most common consisting in DTs with orientation symmetry. The first part of the thesis was aimed at providing an insight on the capabilities of DT-based calibration in explaining a variety of system distortions. A lot of literature has been in fact dedicated throughout the last two decades to the design of ad-hoc solutions by constraining the problem through assumption on the distortion model, on the calibrator equations or on both. In a few cases the authors attempted to solve ill-conditioned problem mitigating (voluntarily or accidentally) the intrinsic system instability by using closed-form analytic estimators. A clear definition of what is feasible and what is instead unfeasible, given a standard set of target calibrators, has therefore represented the first step of our investigation. The methodology proposed shed light on the fact that a DT-based calibration stability can be ensured only in case non-null Faraday rotation with incomplete system distortion model. In all the other cases a point target calibrator is needed. A third possibility, however, is that of performing only a partial retrieval of the distortion, up to a complex scalar coefficient. Analysis of the estimation uncertainty could be carried out as well. As expected, it was found that the cross-talks are the most sensitive parameter to the model deviations, though a number of looks $N_p > 10^5$ and a Cpol-Xpol coherence (assumed null) < 0.01 (-20 dB) would be sufficient to yield a satisfying performance. Such results have been assessed on a theoretical level and then confirmed, in the second part of the chapter, by analytic and numerical estimation analysis. In the context of practical algorithm comparison, it was also possible to show that numerical optimization is able to overcome the traditional closed-form estimators when the data is consistent with the model, whereas it presents more accuracy issues when the deviations of the data from the model are large.

The second part of the work focused then on the most innovative contribution of this thesis: the exploitation of Permanent Scatterers in polarimetric calibration activities. The novelty in the solution proposed required efforts in the formalization of an appropriate PS framework. The fundamental steps of such process were the transposition of the traditional PS model to the polarimetric context and the development of an effective methodology for robustly tackling the inverse problem. This led to the definition of a polarimetric PS detection based on the Generalized Likelihood Ratio Test criterion and to an efficient estimation procedure which exploits the low rank nature of the phase-calibrated PS stack. The integration of these steps in a joint iterative algorithm was named PolPSCal. It was shown that the theoretical calibration performance is in a first approximation related to the number of PSs detected in the imagette and to their polarimetric quality and that it is indeed independent from the PDM expression. The algorithm is neither constrained to a particular PDM model nor to any external information, thus its implementation is practically feasible for any SAR sensor. External calibrators are eventually demanded afterwards in order to normalize the returned PDM stack to an absolute reference.

A critic review of the two different methods is then demanded. Both the spatial and temporal target information processing offer valuable information. Only part of this, however, can be effectively applied to system monitoring and data calibration. In the case of DT-based estimation both radiometric and phase information on the channel imbalance is missing, avoiding any direct feature comparison between acquisitions even when belonging to the same image time series. Differently, in the case of the PS-based approach the compensation would be consistent within the same dataset, but all the images would result distorted by a common unknown PDM. In the last chapter it was demonstrated that the two information are complementary and thus their joint combination can provide an effective contribution to polarimetric monitoring. Once again, a generic distortion model has been conceived, so that the approach can be readily tailored to different sensor scenarios, ranging from higher-frequency SARs to lower-frequency acquisitions affected by Faraday rotations. In the case of C-Band for instance, the encompassing framework achieves an unambiguous temporal monitoring of the all the distortion parameters, up to an absolute radiometric scale factor. The performance has been assessed through synthetic simulations and validated on a Fine Quad-Pol Radarsat-2 dataset which comprises 26 images over the Barcelona area, returning an accuracy on the channel imbalance stability below 0.2 dB and on the cross-talk level <-35 dB, some promising results indeed, that comply with the acknowledged quality standards of polarimetric SAR systems.

In summary, the polarimetric PS technique provides an effective and cheap alternative to traditional ground-surveilled strategies for system monitoring and calibration. When a calibrated image is provided (a single one out of the whole stack) a full data calibration and absolute distortion estimation can be performed. Otherwise, the technique can be conveniently integrated with the DT-based partial estimates in order to unveil the whole temporal distortion information, while retaining comparable performance on the DT unambiguous parameter set.

It has to be properly remarked, however, that this work represents only the first step towards the definition of optimal PS polarimetric calibration strategies. A few questions indeed were left unresolved, the most crucial being possibly the quantitative relationship between the number of images available and the PolPSCal performance (due to indirect influence on the selected target quality) and the technique adaptability to SAR sensors different from the RS-2, both spaceborne and airborne. The first question certainly represents a fine theoretical challenge since it envisages the design of a SAR simulator that must be able to recreate a realistic polarimetric and temporal diversity of the scene. The second is certainly going to involve a few critical aspects such as the large angular spread of airborne imagery and the discrimination of Faraday rotations from system distortion in spaceborne L-Band (ALOS and the announced ALOS-2 and SAOCOM) and P-Band (the ESA BIOMASS candidate) systems. Hopefully such issues will found their solution within the framework of other projects and data acquisition campaigns. Further assessments on different airborne and spaceborne SAR sensors is therefore recommended.

APPENDIX $\mathcal{A}$

Proofs

A.1 Uncertainty of the covariance matrix estimator

Let the k by 1 complex random vector $\mathbf{x} = [x_1 \cdots x_k]^T$ and the associated $2k$ by 1 real vector $\tilde{\mathbf{x}}$ behave as:

$$\mathbf{x} \sim \mathcal{CN}(0, \mathbf{C}) \tag{A.1}$$

$$\tilde{\mathbf{x}} = \left[\begin{array}{c} \mathbf{p} \\ \mathbf{q} \end{array} \right] \sim \mathcal{N}\left(0, \frac{1}{2} \left[\begin{array}{cc} \mathbf{C_R} & -\mathbf{C_I} \\ \mathbf{C_I} & \mathbf{C_R} \end{array} \right] \right) \tag{A.2}$$

$$\mathbf{p} = [p_1 \ldots p_k]^T = \mathcal{R}(\mathbf{x}), \qquad \mathbf{q} = [q_1 \ldots q_k]^T = \mathcal{I}(\mathbf{x})$$
$$\mathbf{C_R} = \left[C_{R_{ij}} \right]_{k \times k} = \mathcal{R}(\mathbf{C}), \qquad \mathbf{C_I} = \left[C_{I_{ij}} \right]_{k \times k} = \mathcal{I}(\mathbf{C})$$

and let their covariance matrix estimates out of N realizations be:

$$\hat{\mathbf{C}} = \frac{1}{N} \sum_{m=1}^{N} \mathbf{x}_m \mathbf{x}_m^H \tag{A.3}$$

whose real and imaginary components are respectively:

$$
\begin{aligned}
\hat{\mathbf{C}}_{\mathbf{R}} &= \left[\hat{C}_{R_{ij}}\right] = \left[\frac{1}{N}\sum_{m=1}^{N} p_i^{(m)}p_j^{(m)} + q_i^{(m)}q_j^{(m)}\right] \\
\hat{\mathbf{C}}_{\mathbf{I}} &= \left[\hat{C}_{I_{ij}}\right] = \left[\frac{1}{N}\sum_{m=1}^{N} q_i^{(m)}p_j^{(m)} - p_i^{(m)}q_j^{(m)}\right].
\end{aligned} \tag{A.4}
$$

Note that the (A.3) is an unbiased estimator when the mean value is known (0 in this case), thus yielding:

$$
E\left[\hat{\mathbf{C}}\right] = \mathbf{C}, \qquad E\left[\hat{\mathbf{C}}_{\mathbf{R}}\right] = \mathbf{C}_{\mathbf{R}}, \qquad E\left[\hat{\mathbf{C}}_{\mathbf{I}}\right] = \mathbf{C}_{\mathbf{I}} \tag{A.5}
$$

The aim so far is the derivation of analytic expressions for the 4 real covariance sets:

$$
\Gamma^{RR}_{ij,kl} = E\left[\left(\hat{C}_{R_{ij}} - C_{R_{ij}}\right)\left(\hat{C}_{R_{kl}} - C_{R_{kl}}\right)\right] \tag{A.6a}
$$

$$
\Gamma^{II}_{ij,kl} = E\left[\left(\hat{C}_{I_{ij}} - C_{I_{ij}}\right)\left(\hat{C}_{I_{kl}} - C_{I_{kl}}\right)\right] \tag{A.6b}
$$

$$
\Gamma^{RI}_{ij,kl} = E\left[\left(\hat{C}_{R_{ij}} - C_{R_{ij}}\right)\left(\hat{C}_{I_{kl}} - C_{I_{kl}}\right)\right] \tag{A.6c}
$$

$$
\Gamma^{IR}_{ij,kl} = E\left[\left(\hat{C}_{I_{ij}} - C_{I_{ij}}\right)\left(\hat{C}_{R_{kl}} - C_{R_{kl}}\right)\right] \tag{A.6d}
$$

that, by exploiting (A.5), lead to:

$$
\Gamma^{AB}_{ij,kl} = E\left[\hat{C}_{A_{ij}}\hat{C}_{B_{kl}}\right] - C_{A_{ij}}C_{B_{kl}} \tag{A.7}
$$

with the apices A, B standing generically for R, I. The first term can be conveniently derived through some trivial, though heavy on the notation, calculation. With respect to the RR case we have for instance:

$$
\begin{aligned}
E\left[\hat{C}_{R_{ij}}\hat{C}_{R_{kl}}\right] &= \frac{1}{N^2}E\left[\sum_m p_i^{(m)}p_j^{(m)} + q_i^{(m)}q_j^{(m)} \cdot \sum_n p_k^{(n)}p_l^{(n)} + q_k^{(n)}q_l^{(n)}\right] \\
&= \frac{1}{N^2}\sum_m\sum_n E\left[p_i^{(m)}p_j^{(m)}p_k^{(n)}p_l^{(n)}\right] + E\left[p_i^{(m)}p_j^{(m)}q_k^{(n)}q_l^{(n)}\right] + \\
&\quad + E\left[q_i^{(m)}q_j^{(m)}p_k^{(n)}p_l^{(n)}\right] + E\left[q_i^{(m)}q_j^{(m)}q_k^{(n)}q_l^{(n)}\right].
\end{aligned} \tag{A.8}
$$

Aided by the Isserlis theorem, $E[x_1x_2x_3x_4] = E[x_1x_2]E[x_3x_4] + E[x_1x_3]E[x_2x_4] + E[x_1x_4]E[x_2x_3]$, and by the intrinsic x property:

$$\forall i,j,m\neq n \qquad E\left[p_i^{(m)}p_j^{(n)}\right]=E\left[q_i^{(m)}q_j^{(n)}\right]=E\left[p_i^{(m)}q_j^{(n)}\right]=E\left[q_i^{(m)}p_j^{(n)}\right]=0 \tag{A.9}$$

we can then solve the 4-th order moments for the two different cases $m=n$ and $m\neq n$, yielding

$$\begin{aligned}
&m=n\\
&E\left[p_i^{(m)}p_j^{(m)}p_k^{(m)}p_l^{(m)}\right]=E\left[p_ip_j\right]E\left[p_kp_l\right]+E\left[p_ip_k\right]E\left[p_jp_l\right]+\\
&\qquad\qquad +E\left[p_ip_l\right]E\left[p_jp_k\right]\\
&\qquad\qquad =\frac{1}{4}C_{R_{ij}}C_{R_{kl}}+\frac{1}{4}C_{R_{ik}}C_{R_{jl}}+\frac{1}{4}C_{R_{il}}C_{R_{jk}}\\
&E\left[p_i^{(m)}p_j^{(m)}q_k^{(m)}q_l^{(m)}\right]=\frac{1}{4}C_{R_{ij}}C_{R_{kl}}+\frac{1}{4}C_{I_{ik}}C_{I_{jl}}+\frac{1}{4}C_{I_{il}}C_{I_{jk}}\\
&E\left[q_i^{(m)}q_j^{(m)}p_k^{(m)}p_l^{(m)}\right]=E\left[p_i^{(m)}p_j^{(m)}q_k^{(m)}q_l^{(m)}\right]\\
&E\left[p_i^{(m)}p_j^{(m)}q_k^{(m)}q_l^{(m)}\right]=E\left[p_i^{(m)}p_j^{(m)}p_k^{(m)}p_l^{(m)}\right]
\end{aligned} \tag{A.10}$$

$$\begin{aligned}
&m\neq n\\
&E\left[p_i^{(m)}p_j^{(m)}p_k^{(n)}p_l^{(n)}\right]=E\left[p_ip_j\right]E\left[p_kp_l\right]=\frac{1}{4}C_{R_{ij}}C_{R_{kl}}\\
&E\left[p_i^{(m)}p_j^{(m)}q_k^{(n)}q_l^{(n)}\right]=\frac{1}{4}C_{R_{ij}}C_{R_{kl}}\\
&E\left[q_i^{(m)}q_j^{(m)}p_k^{(n)}p_l^{(n)}\right]=E\left[p_i^{(m)}p_j^{(m)}q_k^{(n)}q_l^{(n)}\right]\\
&E\left[p_i^{(m)}p_j^{(m)}q_k^{(n)}q_l^{(n)}\right]=E\left[p_i^{(m)}p_j^{(m)}p_k^{(n)}p_l^{(n)}\right]
\end{aligned} \tag{A.11}$$

Equation (A.8) can be therefore simplified into:

$$\begin{aligned}
E\left[\hat{C}_{R_{ij}}\hat{C}_{R_{kl}}\right]&=C_{R_{ij}}C_{R_{kl}}+\frac{1}{2N}C_{R_{ik}}C_{R_{jl}}+\frac{1}{2N}C_{R_{il}}C_{R_{jk}}+\\
&+\frac{1}{2N}C_{I_{ik}}C_{I_{jl}}+\frac{1}{2N}C_{I_{il}}C_{I_{jk}}
\end{aligned} \tag{A.12}$$

The same calculation applied to all the sets in (A.6) yields:

$$\Gamma^{RR}_{ij,kl}=\frac{1}{2N}\left(C_{R_{ik}}C_{R_{jl}}+C_{R_{il}}C_{R_{jk}}+C_{I_{ik}}C_{I_{jl}}+C_{I_{il}}C_{I_{jk}}\right) \tag{A.13}$$

$$\Gamma^{RI}_{ij,kl}=\frac{1}{2N}\left(C_{R_{ik}}C_{I_{jl}}+C_{I_{il}}C_{R_{jk}}-C_{I_{ik}}C_{R_{jl}}-C_{R_{il}}C_{I_{jk}}\right) \tag{A.14}$$

$$\Gamma^{IR}_{ij,kl} = \frac{1}{2N}\left(C_{I_{ik}}C_{R_{jl}} + C_{I_{il}}C_{R_{jk}} - C_{R_{ik}}C_{I_{jl}} - C_{R_{il}}C_{I_{jk}}\right) \quad \text{(A.15)}$$

$$\Gamma^{II}_{ij,kl} = \frac{1}{2N}\left(C_{R_{ik}}C_{R_{jl}} + C_{I_{ik}}C_{I_{jl}} - C_{I_{il}}C_{I_{jk}} - C_{R_{il}}C_{R_{jk}}\right) \quad \text{(A.16)}$$

A.2 Generalized Likelihood Ratio in (3.60)

The reader will find here proof of the validity of the GLR approximated expression:

$$\begin{aligned}\ln\frac{\mathcal{L}\left(\left\{\mathbf{y}_{\mathbf{3}i,p}\right\}_{i=1}^{N_I}|H_1\right)}{\mathcal{L}\left(\left\{\mathbf{y}_{\mathbf{3}i,p}\right\}_{i=1}^{N_I}|H_0\right)} &= \\ \ln\frac{\mathcal{L}\left(\left\{\mathbf{y}_{\mathbf{3}i,p}\right\}_{i=1}^{N_I}\left|\left\{\left\{\hat{\phi}_{i,p}\right\}_{i=1}^{N_I}, \mathbf{s}_{\mathbf{3}p} = \hat{\mathbf{s}}_{\mathbf{3}p}, \mathbf{C}_{\mathbf{3}p} = \Sigma_p^{PS}\right\}\right.\right)}{\mathcal{L}\left(\left\{\mathbf{y}_{\mathbf{3}i,p}\right\}_{i=1}^{N_I}\left|\left\{\mathbf{s}_{\mathbf{3}p} = \mathbf{0}, \mathbf{C}_{\mathbf{3}p} = \Sigma_p^{Cl}\right\}\right.\right)} &\simeq \\ N_I \cdot \ln\left(1 + \hat{\mathbf{s}}_{\mathbf{3}p}^H \hat{\mathbf{C}}_{\mathbf{3}p}^{-1}\hat{\mathbf{s}}_{\mathbf{3}p}\right) & \quad \text{(A.17)}\end{aligned}$$

introduced in (3.60) as the metric aimed to classify the target as PS (hypothesis H_1) or as noise (hypothesis H_0). We remind that $\mathcal{L}$ stands for the likelihood function referring to the observation model of the p-th target in the i-th image:

$$\begin{aligned} H_0: &\quad \mathbf{y}_{\mathbf{3}i,p} = \mathbf{w}_{\mathbf{3}i,p} \\ H_1: &\quad \mathbf{y}_{\mathbf{3}i,p} = e^{j\phi_{i,p}}\mathbf{s}_{\mathbf{3}p} + \mathbf{w}_{\mathbf{3}i,p} \end{aligned} \quad \text{(A.18)}$$

where $\mathbf{s}_{\mathbf{3}p} = \left[\begin{array}{ccc} S_{hh_p} & S_{hv_p} & S_{vv_p}\end{array}\right]^T$ is the PS backscattering vector, $\mathbf{w}_{\mathbf{3}_{i,p}} = \left[\begin{array}{ccc} w_{hh_{i,p}} & w_{hv_{i,p}} & w_{vv_{i,p}}\end{array}\right.$ is the clutter noise behaving according to $\mathbf{w}_{\mathbf{3}_{i,p}} \sim \mathcal{CN}\left(\mathbf{0}, \mathbf{C}_{\mathbf{3}p}\right)$ and $\phi_{i,p}$ is the target phase. Two assumptions has been done: 1) the stack is already calibrated, 2) the thermal noise is negligible compared to the clutter. Since the true parameters in (A.18) are problem unknowns, their estimates $\hat{\phi}$, $\hat{\mathbf{s}}_{\mathbf{3}}$ and

$$\Sigma_p^{PS} = \frac{1}{N_I}\sum_{i=1}^{N_I}(\mathbf{y}_{i,p} - e^{j\hat{\phi}_{i,p}}\hat{\mathbf{s}}_{\mathbf{3}p})(\mathbf{y}_{i,p} - e^{j\hat{\phi}_{i,p}}\hat{\mathbf{s}}_{\mathbf{3}p})^H \quad \text{(A.19)}$$

with

$$\hat{\mathbf{w}}_{\mathbf{3}i,p} = \mathbf{y}_{i,p} - e^{j\hat{\phi}_{i,p}}\hat{\mathbf{s}}_{\mathbf{3}p}$$

are indeed employed in the in the H_1 hypothesis, whereas in the H_0 case the backscatter is assumed null ($\mathbf{s_3} = \mathbf{0}$) and the covariance is computed as:

$$\Sigma_p^{Cl} = \left\langle \mathbf{y}_{\mathbf{3}i,p} \mathbf{y}_{\mathbf{3}i,p}^H \right\rangle_i = \Sigma_p^{PS} + \hat{\mathbf{s}}_{\mathbf{3}p} \hat{\mathbf{s}}_{\mathbf{3}p}^H .$$

The two likelihoods become as a result:

$$\begin{aligned} \mathcal{L}\left(\left\{ \mathbf{y}_{\mathbf{3}i,p} \right\}_{i=1}^{N_I} | H_1 \right) &= \prod_{i=1}^{N_I} \frac{\exp\left(-\hat{\mathbf{w}}_{\mathbf{3}i,p}^H \left(\Sigma_p^{PS} \right)^{-1} \hat{\mathbf{w}}_{\mathbf{3}i,p} \right)}{\pi^3 \cdot \det\left(\Sigma_p^{PS} \right)} \\ \mathcal{L}\left(\left\{ \mathbf{y}_{\mathbf{3}i,p} \right\}_{i=1}^{N_I} | H_0 \right) &= \prod_{i=1}^{N_I} \frac{\exp\left(-\mathbf{y}_{\mathbf{3}i,p}^H \left(\Sigma_p^{Cl} \right)^{-1} \mathbf{y}_{\mathbf{3}i,p} \right)}{\pi^3 \cdot \det\left(\Sigma_p^{Cl} \right)} \end{aligned} \tag{A.20}$$

and the corresponding log-likelihoods:

$$\begin{aligned} \ln \mathcal{L}\left(\left\{ \mathbf{y}_{\mathbf{3}i,p} \right\}_{i=1}^{N_I} | H_1 \right) &= -\sum_{i=1}^{N_I} \hat{\mathbf{w}}_{\mathbf{3}i,p}^H \left(\Sigma_p^{PS} \right)^{-1} \hat{\mathbf{w}}_{\mathbf{3}i,p} \\ &\qquad - N_I \ln \pi^3 - N_I \ln \left[\det\left(\Sigma_p^{PS} \right) \right] \\ &= -N_I \left(1 + \ln \pi^3 - \ln \left[\det\left(\Sigma_p^{PS} \right) \right] \right) \\ \ln \mathcal{L}\left(\left\{ \mathbf{y}_{\mathbf{3}i,p} \right\}_{i=1}^{N_I} | H_0 \right) &= -N_I \left(1 + \ln \pi^3 - \ln \left[\det\left(\Sigma_p^{Cl} \right) \right] \right) \end{aligned} \tag{A.21}$$

where the property $\sum \mathbf{a}^H \mathbf{B} \mathbf{a} = \mathrm{Tr}\left(\sum \mathbf{a}\mathbf{a}^H \mathbf{B} \right)$ has been adopted to simplify the quadratic forms. This leads to the difference between their log-likelihoods:

$$\begin{aligned} \ln \mathcal{L}\left(\left\{ \mathbf{y}_{\mathbf{3}i,p} \right\}_{i=1}^{N_I} | H_1 \right) &- \ln \mathcal{L}\left(\left\{ \mathbf{y}_{\mathbf{3}i,p} \right\}_{i=1}^{N_I} | H_0 \right) \\ &= N_I \ln \left[\det\left(\Sigma_p^{PS} + \hat{\mathbf{s}}_{\mathbf{3}p} \hat{\mathbf{s}}_{\mathbf{3}p}^H \right) \right] - N_I \ln \left[\det\left(\Sigma_p^{PS} \right) \right] \\ &= N_I \ln \left[\det\left(\Sigma_p^{PS} \right) \left(1 + \hat{\mathbf{s}}_{\mathbf{3}p}^H \left(\Sigma_p^{PS} \right)^{-1} \hat{\mathbf{s}}_{\mathbf{3}p} \right) \right] \\ &\qquad\qquad - N_I \ln \left[\det\left(\Sigma_p^{PS} \right) \right] \\ &= N_I \ln \left(1 + \hat{\mathbf{s}}_{\mathbf{3}p}^H \left(\Sigma_p^{PS} \right)^{-1} \hat{\mathbf{s}}_{\mathbf{3}p} \right) \end{aligned} \tag{A.22}$$

which concludes the demonstration.

APPENDIX $\mathcal{B}$

PDM estimation algorithms

B.1 Quegan algorithm

One of the most acknowleged techniques for polarimetric distortion estimation has been proposed by Quegan in [38]. The algorithm is here reported with its original parameter nomenclature and faces the generic distortion model:

$$\mathbf{O} = \mathbf{RST} + \mathbf{N} \tag{B.1}$$

$$\begin{bmatrix} O_{11} & O_{12} \\ O_{21} & O_{22} \end{bmatrix} = \begin{bmatrix} r_{11} & r_{12} \\ r_{21} & r_{22} \end{bmatrix} \begin{bmatrix} S_{11} & S_{12} \\ S_{21} & S_{22} \end{bmatrix} \begin{bmatrix} t_{11} & t_{12} \\ t_{21} & t_{22} \end{bmatrix} + \begin{bmatrix} N_{11} & N_{12} \\ N_{21} & N_{22} \end{bmatrix} \tag{B.2}$$

where the subscripts 1,2 refer to polarizations H and V (in the linearly polarized systems), $\mathbf{O}$ is the observation matrix, $\mathbf{R}$ and $\mathbf{T}$ are the matrices with the system parameters and $\mathbf{N}$ is the total system noise. The approach relies on two essential assumptions made on the target backscatter elements: 1) the validity of the reciprocity principle, i.e. $S_{12} = S_{21}$, 2) the uncorrelation between the true-like and cross-polarized channels, which leads to the target covariance matrix $\mathbf{C_S}$:

$$\mathbf{C_S} = \left\langle S \cdot S^H \right\rangle = \begin{bmatrix} \sigma_{11} & 0 & \rho \\ 0 & \sigma_{21} & 0 \\ \rho & 0 & \sigma_{22} \end{bmatrix} \qquad \text{with} \quad S = \begin{bmatrix} S_{11} \\ S_{12} \\ S_{22} \end{bmatrix} \tag{B.3}$$

Neglecting the effects of the noise $\mathbf{N}$, the resulting data covariance is:

$$\mathbf{C} = \mathbf{M}\mathbf{C_S}\mathbf{M}^H \tag{B.4}$$

where

$$M = \begin{bmatrix} r_{11}t_{11} & r_{11}t_{21} + r_{12}t_{11} & r_{12}t_{21} \\ r_{21}t_{11} & r_{22}t_{11} & r_{22}t_{21} \\ r_{11}t_{12} & r_{11}t_{22} & r_{12}t_{22} \\ r_{21}t_{12} & r_{21}t_{22} + r_{22}t_{12} & r_{22}t_{22} \end{bmatrix} \tag{B.5}$$

and the explicit expression of its elements is:

$$\begin{aligned}
C_{11} &= \left|r_{11}t_{11}\right|^2 \sigma_{11} \\
C_{22} &= \left|r_{21}t_{11}\right|^2 \sigma_{11} + \left|r_{22}t_{21}\right|^2 \sigma_{22} + \left|r_{22}t_{11}\right|^2 \sigma_{21} + 2\mathcal{R}\left(r_{21}r_{22}^*t_{11}t_{21}^*\rho\right) \\
C_{33} &= \left|r_{11}t_{12}\right|^2 \sigma_{11} + \left|r_{12}t_{22}\right|^2 \sigma_{22} + \left|r_{11}t_{22}\right|^2 \sigma_{21} + 2\mathcal{R}\left(r_{11}r_{12}^*t_{12}t_{22}^*\rho\right) \\
C_{44} &= \left|r_{22}t_{22}\right|^2 \sigma_{22} \\
C_{21} &= r_{21}r_{11}^* \left|t_{11}^*\right|^2 \sigma_{11} + r_{22}r_{11}^*t_{21}t_{11}^*\rho^* + r_{22}t_{11}\left(r_{11}^*t_{21}^* + r_{12}^*t_{11}^*\right)\sigma_{21} \\
C_{31} &= \left|r_{11}\right|^2 t_{11}^*t_{12}\sigma_{11} + r_{12}r_{11}^*t_{22}t_{11}^*\rho^* + r_{11}t_{22}\left(r_{11}^*t_{21}^* + r_{12}^*t_{11}^*\right)\sigma_{21} \\
C_{41} &= r_{22}r_{11}^*t_{22}t_{11}^*\rho^* \\
C_{24} &= \left|r_{22}\right|^2 t_{21}t_{22}^*\sigma_{22} + r_{21}r_{22}^*t_{11}t_{22}^*\rho + r_{22}t_{11}\left(r_{21}^*t_{22}^* + r_{22}^*t_{12}^*\right)\sigma_{21} \\
C_{34} &= r_{22}^*r_{12}\left|t_{22}\right|^2 \sigma_{22} + r_{11}r_{22}^*t_{12}t_{22}^*\rho + r_{11}t_{22}\left(r_{21}^*t_{22}^* + r_{22}^*t_{12}^*\right)\sigma_{21} \\
C_{32} &= r_{11}r_{21}^*t_{11}^*t_{12}\sigma_{11} + r_{12}r_{22}^*t_{22}t_{21}^*\sigma_{22} + r_{11}r_{22}^*t_{11}^*t_{22}\sigma_{21} + r_{12}r_{21}^*t_{11}t_{22}^*\rho^* + r_{11}r_{22}^*t_{12}t_{21}^*\rho
\end{aligned} \tag{B.6}$$

In this set of equations the second order terms of r_{12}, r_{21}, t_{12}, t_{21} have been omitted, basing on the hypothesis that cross-talk terms are much smaller than r_{11}, r_{22}, t_{11}, t_{22}. It can also be noticed that no specific parametrization is carried out for the Faraday rotation, which, as a result, becomes incorporated into the r_{ij} and t_{ij} values. This means that the approach is still valid in the presence of Faraday rotations, provided that the FRA is small.

The elements C_{ij} are the only data requested by the algorithm. The first step in Quegan's approach is the evaluation of the cross-talk ratios:

$$u = r_{21}/r_{11} \quad v = t_{21}/t_{22} \quad w = r_{12}/r_{22} \quad z = t_{12}/t_{11} \tag{B.7}$$

which can be done directly from the Cij through the expressions:

$$u = (C_{44}C_{21} - C_{41}C_{24})/\Delta \tag{B.8}$$
$$v = (C_{11}C_{24} - C_{21}C_{14})/\Delta \tag{B.9}$$
$$z = (C_{44}C_{31} - C_{41}C_{34})/\Delta \tag{B.10}$$
$$w = (C_{11}C_{34} - C_{31}C_{14})/\Delta \tag{B.11}$$

where $\Delta = C_{11}C_{44} - |C_{14}|^2$. Thanks to the presence of noise power in C_{44} and C_{11}, the eventuality of $\Delta \simeq 0$ becomes remote, though high values of u, v, w, z still can occur, in which case the algorithm should be rejected. The value of the imbalance ratio $\alpha = \frac{r22}{r11}\frac{t11}{t22}$ is then found by means of a critical analysis of the two solutions α_1 and α_2 achievable through different equations.

$$\alpha_1 = \frac{C_{22} - uC_{12} - vC_{42}}{C_{32} - zC_{12} - wC_{42}} \tag{B.12}$$

$$\alpha_2 = \frac{C_{32}^* - z^*C_{12}^* - w^*C_{42}^*}{C_{33} - z^*C_{31} - w^*C_{34}} \tag{B.13}$$

The two values should be very similar, since both are estimates of α, but never equal. The gap is readily explained by re-introducing the noise on cross-polarized channels. The addition of a noise power term N_p in C_{22} and C_{33}, which are the dominating terms of (B.12) and (B.13) in most acquisitions scenarios, leads to the corrected value of α:

$$\alpha = \frac{|\alpha_1\alpha_2| - 1 + \sqrt{(|\alpha_1\alpha_2| - 1)^2 + 4|\alpha_2|^2}}{2|\alpha_2|} \tag{B.14}$$

which is certainly a better estimate of the ratio, provided that the event $|\alpha_2| \simeq 0$ is not met, i.e. σ_{21} is not null. The method also allows to assess in closed form the noise power affecting the cross-pol channels through the expression:

$$N_p = (C_{32} - zC_{12} - wC_{42})(\alpha_1 - \alpha) \tag{B.15}$$

B.2 Quegan-based L-Band estimation algorithm

In [19] the authors exploit the Quegan approach generality to yield a more accurate physical characterization of the distortion by introducing the Faraday rotations. The only condition demanded is indeed a low cross-talk level, which limits the applicability to a narrow span of rotation angles. Small FR allow though a comfortable linearization of the Faraday matrix, which changes into:

$$\begin{bmatrix} M_{hh} & M_{vh} \\ M_{hv} & M_{vv} \end{bmatrix} = A\left(e^{j\phi}\begin{bmatrix} 1 & \delta_2 \\ \delta_1 & f_1 \end{bmatrix}\begin{bmatrix} 1 & \Omega \\ -\Omega & 1 \end{bmatrix}\begin{bmatrix} S_{hh} & S_{vh} \\ S_{hv} & S_{vv} \end{bmatrix}\right.$$
$$\left.\begin{bmatrix} 1 & \Omega \\ -\Omega & 1 \end{bmatrix}\begin{bmatrix} 1 & \delta_3 \\ \delta_4 & f_2 \end{bmatrix}\right) + \begin{bmatrix} N_{hh} & N_{vh} \\ N_{hv} & N_{vv} \end{bmatrix} \tag{B.16}$$

where the parameters matrices can be combined in order to be imagined as equivalent Rx and Tx matrices and further approximated to get:

$$\begin{bmatrix} 1 & \delta_2' \\ \delta_1' & f_1 \end{bmatrix} = \begin{bmatrix} 1 & \delta_2 \\ \delta_1 & f_1 \end{bmatrix}\begin{bmatrix} 1 & \Omega \\ -\Omega & 1 \end{bmatrix} \cong \begin{bmatrix} 1 & \Omega + \delta_2 \\ \delta_1 - \Omega f_1 & f_1 \end{bmatrix} \tag{B.17}$$

$$\begin{bmatrix} 1 & \delta_4' \\ \delta_3' & f_2 \end{bmatrix} = \begin{bmatrix} 1 & \Omega \\ -\Omega & 1 \end{bmatrix}\begin{bmatrix} 1 & \delta_3 \\ \delta_4 & f_2 \end{bmatrix} \cong \begin{bmatrix} 1 & \delta_3 + \Omega f_2 \\ \delta_4 - \Omega & f_2 \end{bmatrix} \tag{B.18}$$

If the symmetry assumptions is applied to system the cross-talks, i.e. $\delta_1 = \delta_3$ and $\delta_2 = \delta_4$, the number of unknowns reduces to 4 complex numbers and 1 real parameter (9 real unknowns overall). They can be retrieved from the 5 complex Quegan parameters α, u, v, w, z, by solving the following set of non-linear equations:

$$\alpha = f_1/f_2$$

$$u = \delta_1 - \Omega f_1 \qquad w = \frac{\Omega + \delta_2}{f_1} \tag{B.19}$$

$$z = \delta_1 + \Omega f_2 \qquad v = \frac{\delta_2 - \Omega}{f_2}$$

The δ_1 parameter can be immediately computed through u, v and α values as:

$$\delta_1 = \frac{u + \alpha z}{1 + \alpha} \tag{B.20}$$

while the estimation of the other parameters depends on the amplitude of the angle Ω, which in a first moment can be coarsely estimated as $u - \delta_1$ (since f_1 is in the same order as unity). Basically, when $\Omega << (\delta_1, \delta_2)$, there is an absolute scale factor between δ_2, f_1 ,f_2 which cannot be resolved; the information about their ratio alone can be retrieved:

$$\delta_2 \cong w f_1 \cong v f_2 \tag{B.21}$$

When instead Ω is not negligible the absolute value and phase computation of the parameters is possible up to a π phase ambiguity (sign ambiguity). By substituting (B.20) in the u expression in (B.19) we get:

$$u = \frac{u + \alpha z}{1 + \alpha} - \Omega f_1 \Rightarrow \Omega f_1 = \frac{\alpha\left(z - u\right)}{1 + \alpha} \tag{B.22}$$

Then, by combining the w and v expressions we obtain

$$\frac{\Omega}{f_1} = \frac{1}{2}\left(w - \frac{v}{\alpha}\right) \tag{B.23}$$

which, together with the product in (B.22), allows us to find the estimated Ω, f_1 and δ_2 estimates as

$$\Omega f_1 \cdot \left(\frac{f_1}{\Omega}\right)^* = \left|f_1\right|^2 = 2\frac{\left|\alpha\right|^2\left(z - u\right)}{\left(1 + \alpha\right)\left(w^*\alpha^* - v^*\right)} \tag{B.24}$$

$$\angle\left(\Omega f_1 \cdot \frac{f_1}{\Omega}\right) = 2\angle f_1 + 2k\pi \Rightarrow \angle f_1 = \frac{1}{2}\angle\left(\frac{2\alpha^2\left(z - u\right)}{\left(1 + \alpha\right)\left(w\alpha - v\right)}\right) + k\pi \tag{B.25}$$

$$\hat{f}_1 = \sqrt{\left|2\frac{\left|\alpha\right|^2\left(z - u\right)}{\left(1 + \alpha\right)\left(w^*\alpha^* - v^*\right)}\right|} \times e^{j\frac{1}{2}\angle\left(\frac{2\alpha^2\left(z-u\right)}{\left(1+\alpha\right)\left(w\alpha - v\right)}\right)} \tag{B.26}$$

$$\Omega = e^{jk\pi} \cdot \frac{1}{2}\left(w - \frac{v}{\alpha}\right)\hat{f}_1 \rightarrow \hat{\Omega} = \mathcal{R}\left\{\frac{1}{2}\left(w - \frac{v}{\alpha}\right)\hat{f}\right\} \tag{B.27}$$

$$\delta_2 = e^{jk\pi} \cdot \frac{1}{2}\left(w + \frac{v}{\alpha}\right)\hat{f}_1 \rightarrow \hat{\delta}_2 = \frac{1}{2}\left(w + \frac{v}{\alpha}\right)\hat{f}_1 \tag{B.28}$$

where the π ambiguity in the phase is clear. The last parameter, f_2, can be easily found from α as $\hat{f}_2 = \alpha/\hat{f}_1$, the result being obviously $\hat{f}_2 = f_2 e^{jk\pi}$. Therefore as far as$-\pi < \angle f_1 < \pi$ the values retrieved are correct, otherwise a π shift has to be added; this issue can be solved if we have at disposal previous f_1 measurements, thus pretending that the phase changed following the shortest path between acquisitions (note that f_2 and δ_2 can be used as well for this test). In summary, the approach is supposed to achieve good results in a significant but limited range of scenarios, since the conditions required are not always easily met.

APPENDIX C

A Maximum Likelihood PolPSCal refinement

C.1 SVD vs Maximum Likelihood

The estimators so far addressed do not represent the optimum in the Maximum Likelihood sense, though the PS quality is high result achieved are nonetheless satisfying. It is in fact easy to show that the SVD solution represents the Least Squares solution of the joint $\mathbf{H}, \mathrm{s}$ determination problem. Given the PS model in (3.1) and its noise characterization (3.13)-(3.14) the probability density function (pdf) of the the single observation $\mathbf{y}$ is:

$$p_y(\mathbf{y}_{i,p}) = \frac{1}{\pi^4 \cdot \det(\mathbf{H}_i \mathbf{C}_p \mathbf{H}_i^H)} \exp\left(-(\mathbf{y}_{i,p} - e^{j\phi_{i,p}} \mathbf{H}_i \mathbf{s}_p)^H \times \right. \\ \left. \mathbf{\Gamma}_{i,p}^{-1} (\mathbf{y}_{i,p} - e^{j\phi_{i,p}} \mathbf{H}_i \mathbf{s}_p)\right) \quad \text{(C.1)}$$

with

$$\mathbf{\Gamma}_{i,p} = \mathbf{H}_i \mathbf{C}_p \mathbf{H}_i^H + \sigma_n \mathbf{I} \quad \text{(C.2)}$$

The pdf of whole stack, taking into account (3.5), can be expressed as:

$$p_y(\mathbf{Y}) = \frac{1}{\prod_i \prod_p \pi^4 \cdot \det(\mathbf{H}_i \mathbf{C}_p \mathbf{H}_i^H)} \times \\ \exp\left(-\sum_i \sum_p (\mathbf{y}_{i,p} - e^{j\phi_{i,p}} \mathbf{H}_i \mathbf{s}_p)^H \mathbf{\Gamma}_{i,p}^{-1} (\mathbf{y}_{i,p} - e^{j\phi_{i,p}} \mathbf{H}_i \mathbf{s}_p) \right) \quad \text{(C.3)}$$

The ML solution demands the maximization of the log-likelihood:

$$\mathcal{L}(\mathbf{Y}) = -\sum_i \sum_p (\mathbf{y}_{i,p} - e^{j\phi_{i,p}} \mathbf{H}_i \mathbf{s}_p)^H \mathbf{\Gamma}_{i,p}^{-1} (\mathbf{y}_{i,p} - e^{j\phi_{i,p}} \mathbf{H}_i \mathbf{s}_p) - \\ \sum_i \sum_p \log |\mathbf{\Gamma}_{i,p}| - 4 N_I N_P \log(\pi). \quad \text{(C.4)}$$

When an estimate of the phases, ϕ, is available, the ML approach reduces to the particular solution:

$$\hat{\mathbf{H}}_i, \hat{\mathbf{s}}_p = \underset{\mathbf{H}_i, \mathbf{s}_p}{\operatorname{argmin}} \left(\sum_i \sum_p \|\mathbf{\Gamma}_{i,p}^{-1/2} \cdot (\mathbf{z}_{i,p} - \mathbf{H}_i \mathbf{s}_p)\| - \log |\mathbf{\Gamma}_{i,p}| \right) \quad \text{(C.5)}$$

with $\mathbf{z}_{i,p} = e^{-j\phi_{i,p}} \mathbf{y}_{i,p}$, where the displacement between the real and the reconstructed data is weighted by the noise covariance. Such ℓ_2 norm indeed allows good quality PSs to influence the estimates more then the noisy ones. Notice, on the opposite, that the Frobenius norm criterion in (3.45) corresponds to the Least Squares (LS) optimum:

$$\hat{\mathbf{H}}_{\mathbf{3}i}, \hat{\mathbf{s}}_{\mathbf{3}p} = \underset{\mathbf{H}_{\mathbf{3}i}, \mathbf{s}_{\mathbf{3}p}}{\operatorname{argmin}} \left(\sum_i \sum_p \|\mathbf{z}_{i,p} - \mathbf{H}_{\mathbf{3}i} \mathbf{s}_{\mathbf{3}p}\| \right) \quad \text{(C.6)}$$

where all the error contributes are equally weighted.

C.2 A numerical ML optimization

The opportunity of performing a further ML optimization will be then explored. Since the analytic treatment of (C.4) seems unfeasible, the ML problem has been approached by means of iterative numeric techniques. Besides, it must be remembered that the estimates (**??**),(3.57)-(3.58), that will be used to determine the starting point of the algorithm, are affected by uncertainty. Two important characteristics of (C.4) can though be exploited in order to plan an efficient optimization procedure which takes into account the mentioned issues:

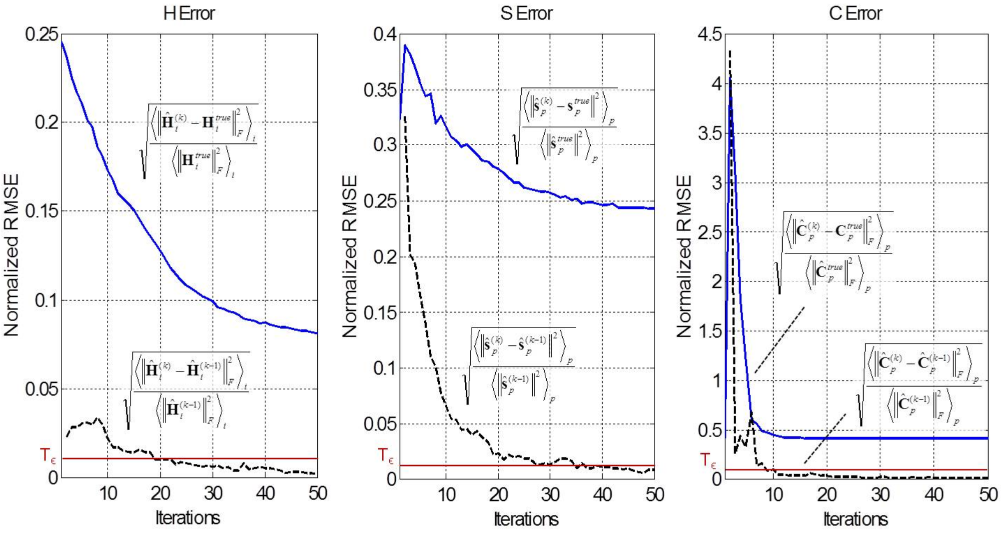

Figure C.1: *Results of the iterative ML refinement procedure on a single simulated case study with parameters:* $N_p = 100$, $N_I = 10$, *average SCR of 5 dB. The normalized RMSE of the estimated PDMs, target signatures and target covariances are reported with comprehensive metrics for each algorithm iteration.*

- Given a predefined set of target parameters $\hat{\mathrm{s}}$, $\hat{\mathbf{C}}$ the distortion estimates of each image is independent from those of the others. In formulas:

  $$\hat{\mathbf{H}}_i \Big| \left(\{\mathbf{H}_j\}_{j\neq i}, \{\hat{\mathrm{s}}, \hat{\mathbf{C}}\}\right) = \hat{\mathbf{H}}_i \Big| \{\hat{\mathrm{s}}, \hat{\mathbf{C}}\}$$

  The same behavior also applies to the target estimates, being:

  $$\{\hat{\mathrm{s}}_p, \hat{\mathbf{C}}_p\} \Big| \left(\{\hat{\mathbf{H}}\}, \{\mathrm{s}_k, \mathbf{C}_k\}_{k\neq p}\right) = \{\hat{\mathrm{s}}_p, \hat{\mathbf{C}}_p\} \Big| \{\hat{\mathbf{H}}\}$$

- The log-likelihood is invariant to any linear complex uncertainty $\mathbf{B}$. Introducing indeed the ambiguous parameters $\mathbf{H_a} = \mathbf{H_3}\mathbf{B}^{-1}$, $\mathbf{s_a} = \mathbf{B} \cdot \mathbf{s_3}$, $\mathbf{w_a} = \mathbf{B} \cdot \mathbf{D} \cdot \mathbf{w}$ and then defining $\mathbf{C_a} = E[\mathbf{w_a}\mathbf{w_a}^H] = \mathbf{B}\mathbf{C_3}\mathbf{B}^H$, it can be easily demonstrated that the invariance relationships:

  $$\mathbf{Y}(\mathbf{H_a}, \mathbf{s_a}, \mathbf{w_a}) = \mathbf{Y}(\mathbf{H}, \mathbf{S}, \mathbf{w}) \tag{C.7}$$

  $$\mathcal{L}(\mathbf{Y}|\{\mathbf{H_a}, \mathbf{S_a}, \mathbf{C_a}\}) = \mathcal{L}(\mathbf{Y}|\{\mathbf{H}, \mathbf{S}, \mathbf{C}\}) \tag{C.8}$$

  are satisfied.

Note that this latter point is verified even when the white noise (3.9) is reintroduced in the model. As evidenced with concern to the PS selection - SVD estimation algorithm, such property is essential for the relative PS calibration algorithm since it provides the possibility of retrieving correctly all the parameters basing on the available data alone, except for that uncertainty term which can be conveniently removed in a post-processing phase (discussed in 3.4.3). The implemented algorithm is therefore intended to iteratively refine the estimates by operating on the image parameters $\tilde{\mathbf{H}}_\mathbf{3}$ at first and on the target parameters $\tilde{\mathbf{s}}_\mathbf{3}$,$\tilde{\mathbf{C}}_\mathbf{3}$ in a second moment, exploiting therefore the property commented on the first point. More formally, the first block performs:

$$\tilde{\mathbf{H}}_{\mathbf{3}i} = \underset{\mathbf{H}_{\mathbf{3}i}}{\operatorname{argmin}} \left(\mathcal{L} \left(\mathbf{Y} \middle| \{\tilde{\mathbf{S}}_\mathbf{3}, \tilde{\mathbf{C}}_\mathbf{3}\} \right) \right) \tag{C.9}$$

whereas the second one completes the set with:

$$\tilde{\mathbf{s}}_{\mathbf{3}p}, \tilde{\mathbf{C}}_{\mathbf{3}p} = \underset{\mathbf{S}_{\mathbf{3}p}, \mathbf{C}_{\mathbf{3}p}}{\operatorname{argmin}} \left(\mathcal{L} \left(\mathbf{Y} \middle| \{\tilde{\mathbf{H}}_\mathbf{3}\} \right) \right) \tag{C.10}$$

where it was assumed that the thermal noise power σ_n is known since it can be accurately estimated through traditional techniques such as Quegan's [ref]. The phases $\hat{\phi}$ is identically updated at each iteration, though, differently from (C.9) and (C.10), the analytic form of its ML estimator is available:

$$\hat{\phi}_{i,p} = \angle \left(\mathbf{y}_{i,p}^H \tilde{\mathbf{\Gamma}}_{i,p}^{-1} \tilde{\mathbf{H}}_{\mathbf{3}i} \tilde{\mathbf{s}}_{\mathbf{3}p} \right) \tag{C.11}$$

with $\tilde{\mathbf{\Gamma}}_{i,p} = \tilde{\mathbf{H}}_{\mathbf{3}i} \tilde{\mathbf{C}}_{\mathbf{3}p} \tilde{\mathbf{H}}_{\mathbf{3}i}^H + \sigma_n \mathbf{I}$. A total number of 12 real parameters (6 degrees of freedom for the covariances and 6 for the backscatter) are jointly optimized in (C.10), whereas 24 real parameters are involved in (C.9). Since the overall number of parameters is high, the convergence of the numeric solver to the correct estimates is not guaranteed, thought it can be argued that the algorithm manages to overcome this complexity thanks to the high quality initialization returned by the SVD-based estimates. In Fig. C.1 the results of the refinement when applied to a synthetic dataset built on 10 images and 100 PSs with an average SCR quality of 5 dB is shown. The metrics adopted are the normalized total RMSE residuals on $\tilde{\mathbf{H}}_\mathbf{3}$, $\tilde{\mathbf{s}}_\mathbf{3}$, $\tilde{\mathbf{C}}_\mathbf{3}$, computed respectively as $\Delta_H = \sqrt{\frac{\sum_i \|\hat{\mathbf{H}}_\mathbf{3} - \mathbf{H}_\mathbf{3}\|^2}{\sum_i \|\mathbf{H}_\mathbf{3}\|^2}}$, $\Delta_s = \sqrt{\frac{\sum_p \|\hat{\mathbf{s}}_\mathbf{3} - \mathbf{s}_\mathbf{3}\|^2}{\sum_p \|\mathbf{s}_\mathbf{3}\|^2}}$, $\Delta_C = \sqrt{\frac{\sum_p \|\hat{\mathbf{C}}_\mathbf{3} - \mathbf{C}_\mathbf{3}\|^2}{\sum_p \|\mathbf{C}_\mathbf{3}\|^2}}$, which have evaluated at each iteration. Notice that all the errors tend to decrease, confirming that the procedure is indeed effective. The initial misleading behavior in the target backscatter and covariance error is due to the fact that (C.9) is performed before (C.10). The iterations can be arrested either at the k-th step when all the metrics $\epsilon_H = \sqrt{\frac{\sum_i \|\tilde{\mathbf{H}}_\mathbf{3}^{(k)} - \tilde{\mathbf{H}}_\mathbf{3}^{(k-1)}\|_F^2}{\sum_i \|\tilde{\mathbf{H}}_\mathbf{3}^{(k-1)}\|_F^2}}$, $\epsilon_s = \sqrt{\frac{\sum_p \|\tilde{\mathbf{s}}_\mathbf{3}^{(k)} - \tilde{\mathbf{s}}_\mathbf{3}^{(k-1)}\|_F^2}{\sum_p \|\tilde{\mathbf{s}}_\mathbf{3}^{(k-1)}\|_F^2}}$, $\epsilon_C = \sqrt{\frac{\sum_p \|\tilde{\mathbf{C}}_\mathbf{3}^{(k)} - \tilde{\mathbf{C}}_\mathbf{3}^{(k-1)}\|_F^2}{\sum_p \|\tilde{\mathbf{C}}_\mathbf{3}^{(k-1)}\|_F^2}}$ agree to the condition:

$$\epsilon < T_\epsilon \tag{C.12}$$

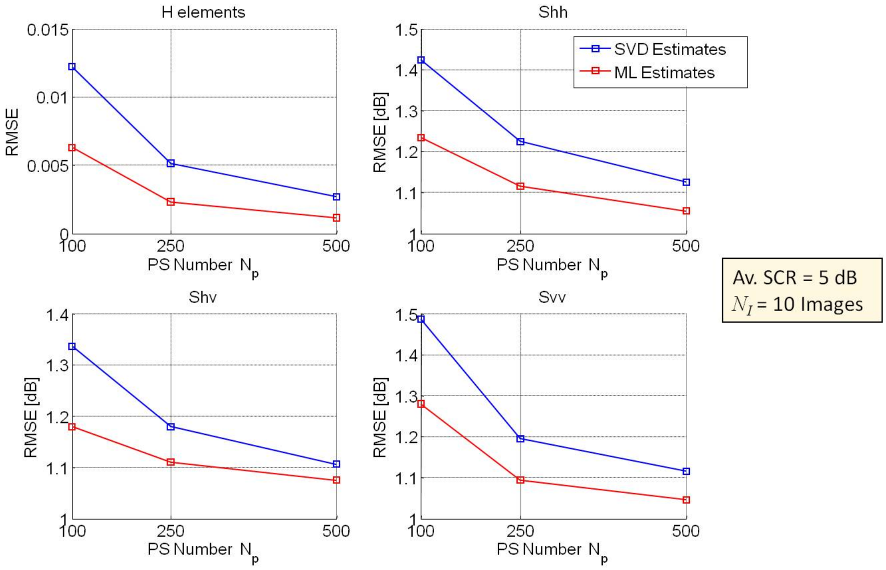

Figure C.2: *PolPSCal theoretical performance assessed through Montecarlo simulation of PS datasets with* $N_p = 100$ *targets. The RMSE achieved through the first SVD estimation and a further ML refinement are compared. The quality of the* S_{HV} *estimates is worst than that of the HH,VV channels since the cross-pol backscatter power is 5 dB weaker than the co-pol returns, resulting in a lower SNR with respect to the thermal noise floor, which is the uniform throughout the channels.*

with the threshold T_ϵ set to the reasonable value of 0.01, or when the maximum number of iterations (set to 50) is reached. In the case of Fig. C.1 all 50 iterations are shown. The average impact on the PolPSCal estimates is then attained on a synthetic dataset of 10 images with average PS quality of 5 dB SCR and shown in Fig. C.2. The most evident improvements occur in the RMSE of the PDM elements, which is halved by the ML optimization. The study provided here though is not exhaustive. It must in fact be remarked that the computational costs, depending on N_I and N_p, are very high in terms of the time demanded. Moreover the robustness of the iterative procedure in the case of more complex datasets where the clutter disturbance is not perfectly gaussian (as in the case of real data) still has to be properly assessed. So far, the ML refinement here proposed must be considered as a noteworthy cue for further performance optimization. However, in the theoretical and real measured performance that will follow such step has been abandoned.

Bibliography

[1] T.L. Ainsworth, L. Ferro-Famil, and Jong-Sen Lee. Orientation angle preserving a posteriori polarimetric sar calibration. *Geoscience and Remote Sensing, IEEE Transactions on*, 44(4):994 – 1003, april 2006. 4.2.3

[2] S.H. Bickel and R.H.T. Bates. Effects of magneto-ionic propagation on the polarization scattering matrix. *Proceedings of the IEEE*, 53(8):1089 – 1091, aug. 1965. 2.1.2, 2.1.4, 2.5, 3.4

[3] W.-M. Boerner, M. El-Arini, Chung-Yee Chan, and P. Mastoris. Polarization dependence in electromagnetic inverse problems. *Antennas and Propagation, IEEE Transactions on*, 29(2):262 – 271, mar 1981. 1.1

[4] M. Borgeaud, R.T. Shin, and J.A. Kong. Theoretical models for polarimetric radar clutter. *Journal of Electromagnetic Waves and Applications*, 1(1):73–89, 1987. 2.2.1

[5] Jie Chen and Shaun Quegan. Improved estimators of faraday rotation in spaceborne polarimetric sar data. *Geoscience and Remote Sensing Letters, IEEE*, 7(4):846 –850, oct. 2010. 2.1.4, 3.4

[6] P.N. Churchill and E.P.W. Attema. The european airborne polarimetric sar campaign maestro 1. In *Geoscience and Remote Sensing Symposium, 1991. IGARSS '91. Remote Sensing: Global Monitoring for Earth Management., International*, volume 2, pages 327 –328, jun 1991. 1.1

[7] S.R. Cloude and E. Pottier. A review of target decomposition theorems in radar polarimetry. *Geoscience and Remote Sensing, IEEE Transactions on*, 34(2):498–518, Mar 1996. 2.1.2

[8] S.R. Cloude and E. Pottier. An entropy based classification scheme for land applications of polarimetric SAR. *Geoscience and Remote Sensing, IEEE Transactions on*, 35(1):68–78, Jan 1997. 3.2.2

[9] D. D'Aria, A. Ferretti, A.M. Guarnieri, and S. Tebaldini. Sar calibration aided by permanent scatterers. *Geoscience and Remote Sensing, IEEE Transactions on*, 48(4):2076 –2086, april 2010. 1.1, 3.1, 3.2.1

[10] Y. Dong, B. Forster, and C. Ticehurst. Radar backscatter analysis for urban environments. *International Journal of Remote Sensing*, 18(6):1351–1364, 1997. 3.2

[11] P.C. Dubois, D. Evans, and J. van Zyl. Approach to derivation of sir-c science requirements for calibration. *Geoscience and Remote Sensing, IEEE Transactions on*, 30(6):1145 –1149, nov 1992. 1.1, 2.1.3, 2.1.3

[12] P. Dubois-Fernandez, H. Oriot, C. Coulombeix, H. Cantalloube, O. Ruault du Plessis, T. Le Toan, S. Daniel, J. Chave, L. Blanc, M. Davidson, and M. Petit. Tropisar: Exploring the temporal behavior of p-band sar data. In *Geoscience and Remote Sensing Symposium (IGARSS), 2010 IEEE International*, pages 1319 –1322, july 2010. 2.1.3

Bibliography

[13] C. Eckart and G. Young. The approximation of one matrix by another of lower rank. *Psychometrika*, 1:211–218, 1936. 10.1007/BF02288367. 3.4.1

[14] A. Ferretti, C. Prat, and F. Rocca. Permanent scatterers in sar interferometry. *IEEE Trans. Geosci. Remote Sens.*, vol. 39, no. 11:8–20, Jan. 2001. 3.2, 3.2.1

[15] A. Freeman. Sar calibration: an overview. *Geoscience and Remote Sensing, IEEE Transactions on*, 30(6):1107 –1121, nov 1992. 1.1, 2.2.2, 2.2.2, 3.4.3

[16] A. Freeman. Calibration of linearly polarized polarimetric sar data subject to faraday rotation. *Geoscience and Remote Sensing, IEEE Transactions on*, 42(8):1617 – 1624, aug. 2004. 1.1, 2.1.4, 2.2.1, 3.1, 3.3

[17] A. Freeman, M. Alves, B. Chapman, J. Cruz, Y. Kim, S. Shaffer, J. Sun, E. Turner, and K. Sarabandi. Sir-c data quality and calibration results. *Geoscience and Remote Sensing, IEEE Transactions on*, 33(4):848 –857, jul 1995. 1.1

[18] A. Freeman and S.L. Durden. A three-component scattering model for polarimetric sar data. *Geoscience and Remote Sensing, IEEE Transactions on*, 36(3):963 –973, may 1998. 2.3.4

[19] A. Freeman, X. Pi, and B. Chapman. Calibration of palsar polarimetric data. In *Proc. of 4th Int. Workshop on Science and Applications of SAR polarimetry and Polarimetric Interferometry - PolInSAR 2009*, volume ESA SP-668, apr. 2009. 1.1, 2.1.1, 2.1.4, 2.4.2, 3.1, 3.4, B.2

[20] A. Freeman and S.S. Saatchi. On the detection of faraday rotation in linearly polarized l-band sar backscatter signatures. *Geoscience and Remote Sensing, IEEE Transactions on*, 42(8):1607 – 1616, aug. 2004. 2.4.1

[21] A. Freeman, Y. Shen, and C.L. Werner. Polarimetric sar calibration experiment using active radar calibrators. *Geoscience and Remote Sensing, IEEE Transactions on*, 28(2):224–240, Mar 1990. 1.1

[22] D. Giuli. Polarization diversity in radars. *Proceedings of the IEEE*, 74(2):245 – 269, feb. 1986. 1.1

[23] Dinh Ho Tong Minh, Ludovic Villard, Mauro Mariotti d'Alessandro, Stefano Tebaldini, Fabio Rocca, and Le Toan Thuy. Relating tropical forest biomass to p-band sar tomography. In *IGARSS 2012, submitted*, 2012. 2.1.3

[24] R.L. Jordan, B.L. Huneycutt, and M. Werner. The sir-c/x-sar synthetic aperture radar system. *Geoscience and Remote Sensing, IEEE Transactions on*, 33(4):829 –839, jul 1995. 1.1

[25] S.M. Kay. *Fundamentals of Statistical Signal Processing: Detection theory*. Prentice Hall Signal Processing Series. Prentice-Hall PTR, 1998. 3.2.3

[26] Jong-Sen Lee and T.L. Ainsworth. The effect of orientation angle compensation on coherency matrix and polarimetric target decompositions. *Geoscience and Remote Sensing, IEEE Transactions on*, 49(1):53 –64, jan. 2011. 2.2.1, 2.4.1, 4.3.3

[27] Jong-Sen Lee, E. Krogager, T.L. Ainsworth, and W.-M. Boerner. Polarimetric analysis of radar signature of a manmade structure. *Geoscience and Remote Sensing Letters, IEEE*, 3(4):555 –559, oct. 2006. 3.2

[28] A. Luscombe. Image quality and calibration of radarsat-2. In *IEEE IGARSS 2009*, volume 2, july 2009. 1.1, 2.4.1, 4.3.3

[29] L. m. Novak and M. c. Burl. Optimal speckle reduction in polarimetric SAR imagery. *Advances in Engineering Software*, 1990. 3.2.3, 3.2.3

[30] T. Macklin, P. Wright, and P. Meadows. Sensitivity of sar calibration to the combined effects of cross- talk, channel imbalance and faraday rotation. *EUSAR 2006 Proceedings*, 2006. 2.1.3

[31] G. Margarit, J.J. Mallorqui, and L. Pipia. Polarimetric characterization and temporal stability analysis of urban target scattering. *Geoscience and Remote Sensing, IEEE Transactions on*, 48(4):2038 –2048, april 2010. 3.2

[32] F.J. Meyer. Performance requirements for ionospheric correction of low-frequency sar data. *Geoscience and Remote Sensing, IEEE Transactions on*, 49(10):3694 –3702, oct. 2011. 2.1.2, 2.1.3

[33] F.J. Meyer and J.B. Nicoll. Prediction, detection, and correction of faraday rotation in full-polarimetric l-band sar data. *Geoscience and Remote Sensing, IEEE Transactions on*, 46(10):3076 –3086, oct. 2008. 2.1.4

[34] V.D. Navarro-Sanchez, J.M. Lopez-Sanchez, and F. Vicente-Guijalba. A contribution of polarimetry to satellite differential sar interferometry: Increasing the number of pixel candidates. *Geoscience and Remote Sensing Letters, IEEE*, 7(2):276 –280, april 2010. 3.2.3

[35] L. Novak, M. Sechtin, and M. Cardullo. Studies of target detection algorithms that use polarimetric radar data. *IEEE Transactions on Aerospace and Electronic Systems*, AES-25(2), 1989. 3.2.3

[36] D. Perissin and A. Ferretti. Urban-target recognition by means of repeated spaceborne sar images. *Geoscience and Remote Sensing, IEEE Transactions on*, 45(12):4043 –4058, dec. 2007. 3.2

[37] L. Pipia et al. Polarimetric temporal information for urban deformation map retrieval. In *Geosci. Rem. Sens. Symposium. IGARSS 2007. IEEE Intern.*, july 2007. 3.2

[38] S. Quegan. A unified algorithm for phase and cross-talk calibration of polarimetric data-theory and observations. *Geoscience and Remote Sensing, IEEE Transactions on*, 32(1):89 –99, jan 1994. 1.1, 1.2, 2.1.4, 2.2.1, 2.4, 3.1, 3.3, 3.4, 4.2.2, 4.2.3, 4.3.2, B.1

[39] A. Refice, F. Mattia, and G. de Carolis. Polarimetric optimisation applied to permanent scatterers identification. In *Geoscience and Remote Sensing Symposium, 2003. IGARSS '03. Proceedings. 2003 IEEE International*, volume 2, pages 687 – 689 vol.2, july 2003. 3.2.3

[40] C.L. Rino. On the application of phase screen models to the interpretation of ionospheric scintillation data. *Radio Science*, vol. 17, no. 4:885–867, 1982. 2.1.2

[41] D.R. Sheen, A. Freeman, and E.S. Kasischke. Phase calibration of polarimetric radar images. *Geoscience and Remote Sensing, IEEE Transactions on*, 27(6):719 – 731, nov 1989. 1.1

[42] M. Shimada. Model-based polarimetric sar calibration method using forest and surface-scattering targets. *Geoscience and Remote Sensing, IEEE Transactions on*, 49(5):1712 –1733, may 2011. 1.1, 2.1.1, 2.1.4, 2.3.3, 2.3.4.2, 4.2.3

[43] M. Shimada, O. Isoguchi, T. Tadono, and K. Isono. Palsar radiometric and geometric calibration. *Geoscience and Remote Sensing, IEEE Transactions on*, 47(12):3915 –3932, dec. 2009. 1.1, 2.1.4

[44] G. Stewart. On the early history of the singular value decomposition. *SIAM Review*, 35(4):551–566, 1993. 3.4.1

[45] R. Touzi and M. Shimada. Polarimetric palsar calibration. *Geoscience and Remote Sensing, IEEE Transactions on*, 47(12):3951 –3959, dec. 2009. 1.1, 2.1.1, 2.1.4

[46] J. Uher, C. Grenier, and G. Lefebvre. Radarsat-2 sar antenna. *Canadian Journal of Remote Sensing*, 30(3):287–294, jun. 2004. 2.1.1

[47] F.T. Ulaby and C. Elachi. *Radar polarimetry for geoscience applications*. Artech House remote sensing library. Artech House, 1990. 1.1

[48] H.L. Van Trees. *Detection, Estimation, and Modulation Theory*. Number v. 1 in Detection, Estimation, and Modulation Theory. John Wiley & Sons, 2001. 3.2.3

[49] J.J. van Zyl. Calibration of polarimetric radar images using only image parameters and trihedral corner reflector responses. *Geoscience and Remote Sensing, IEEE Transactions on*, 28(3):337 –348, may 1990. 1.1, 2.1.1, 2.1.4, 2.2.1, 2.3.4.2, 3.1, 3.3

[50] Yanting Wang, T.L. Ainsworth, and Jong-Sen Lee. Assessment of system polarization quality for polarimetric sar imagery and target decomposition. *Geoscience and Remote Sensing, IEEE Transactions on*, 49(5):1755 –1771, may 2011. 3.3

[51] M.W. Whitt, F.T. Ulaby, P. Polatin, and V.V. Liepa. A general polarimetric radar calibration technique. *Antennas and Propagation, IEEE Transactions on*, 39(1):62 –67, jan 1991. 1.1

[52] P.A. Wright, S. Quegan, N.S. Wheadon, and C.D. Hall. Faraday rotation effects on l-band spaceborne sar data. *Geoscience and Remote Sensing, IEEE Transactions on*, 41(12):2735 – 2744, dec. 2003. 2.1.4

[53] Jian Yang, Y. Yamaguchi, W.-M. Boerner, and Shiming Lin. Numerical methods for solving the optimal problem of contrast enhancement. *Geoscience and Remote Sensing, IEEE Transactions on*, 38(2):965 –971, mar 2000. 3.2.3

[54] H.A. Zebker and J.J. Van Zyl. Imaging radar polarimetry: a review. *Proceedings of the IEEE*, 79(11):1583 –1606, nov 1991. 1.1

[55] H.A. Zebker, J.J. Van Zyl, S.L. Durden, and L. Norikane. Calibrated imaging radar polarimetry: technique, examples, and applications. *Geoscience and Remote Sensing, IEEE Transactions on*, 29(6):942 –961, nov 1991. 1.1

Acknowledgments

So, that's it, I'm actually writing the acknowledgments at the end of this long ride. A compelling ride, rich of gratification and personal growth, but certainly not an easy one. I started this path out of the enthusiasm for the signal processing and remote sensing topics that were conveyed to me by top level POLIMI scientists and teachers. I'm referring of course to prof. Fabio Rocca, prof. Claudio Prati and prof. Andrea Monti Guarnieri, to whom I'm indebted both for my previous student career and recently as a member of their radar group. The years has been filled with edifying moments as well as with stressful ones. I believe that all those moments were equally important, contributing to form altogether the person that I have so far become.

Above all, I would like to thank prof. Monti Guarnieri, my supervisor. His inspired and constant support have been essential for my scientific and professional achievements. I also owe sincere gratitude to Stefano Tebaldini, and I feel that the quality of my research significantly benefited from all my discussions with him. I am thankful to Davide D'Aria, managing director of the Aresys s.r.l., for introducing me in the world of SAR and supporting my activity through active collaboration with the DEI department.

Thanks are certainly due to the Italian Space Agency (ASI) for sponsoring the project and to the Canadian Space Agency (CSA) for providing us the RADARSAT-2 dataset, foundamental for our analysis, within the SOAR-EU framework.

I am then grateful to all the other members and friends working in the DEI remote sensing group and in Aresys. I truly felt that the time spent in conversation with them was extremely fruitful and enjoying. I'd like to further extend this list to all the DEI 'comrades', since they contributed so much at creating a genuine and enjoyable atmosphere at work and at having plenty of fun and relax in the free time. The friendship that I could grow up with them is among the most positive things of this last four years.

Last, but not least, I'd like to pay tribute to my old friends, which I indeed consider nothing less than a second family, and I wish to specify that this effort would not have been possible without the support of my parents and my brother Nicola. to whom I am and I will always be grateful.